

Silicon Photomultiplier Classification of the GCT Camera of CTA

Silicon Photomultiplier Klassifikation der GCT Kamera von CTA

Master-Thesis von Ben Gebhardt aus Heidelberg

Tag der Einreichung:

1. Gutachten: Dr. Richard White (MPIK)
2. Gutachten: Prof. Jim Hinton (MPIK)
3. Gutachten: Prof. Tetyana Galatyuk (TU DA)



TECHNISCHE
UNIVERSITÄT
DARMSTADT

Fachbereich Physik
Max Planck Institut für Kernphysik Heidelberg

8 Silicon Photomultiplier Classification of the GCT Camera of CTA
Silicon Photomultiplier Klassifikation der GCT Kamera von CTA

Vorgelegte Master-Thesis von Ben Gebhardt aus Heidelberg

1. Gutachten: Dr. Richard White (MPIK)
2. Gutachten: Prof. Jim Hinton (MPIK)
3. Gutachten: Prof. Tetyana Galatyuk (TU DA)

Tag der Einreichung:

¹⁰
¹¹ **Abstract**

¹² whats this about



Abstract

13
14
15 worum es geht



16 **Contents**

18	1 Cosmic Radiation	5
19	1.1 Air shower induced Cherenkov Radiation	7
20	1.2 Imaging Atmospheric Cherenkov Telescopes	8
21	2 Cherenkov Telescope Array	10
22	2.1 GCT	11
23	2.2 CHEC	12
24	3 Silicon Photomultipliers	14
25	3.1 SiPM characteristics	14
26	3.2 Gain of a Silicon Photomultiplier	17
27	3.3 Thermally induced dark counts	18
28	3.4 Avalanche-induced secondary effects	19
29	3.5 Photon Detection Efficiency	20
30	4 Experimental Setup	22
31	5 Data Analysis	28
32	5.1 Tracefile Conversion	28
33	5.2 Pedestal Subtraction	29
34	5.3 Peak Detection	30
35	5.4 Gain Extraction	31
36	5.5 Data Challenges	34
37	6 Results	37
38	6.1 SiPM devices for CTA	37
39	6.2 Hamamatsu S12642-1616PA-50 50 μ m 3mm	39
40	6.3 Hamamatsu LCT5 50 μ m 6mm	44
41	6.4 Hamamatsu LCT5 75 μ m 7mm	48
42	6.5 Hamamatsu LVR 50 μ m 6mm	51
43	6.6 SensL FJ60035 6mm 35 μ m	54
44	7 Comparison	56
45	7.1 Dark Count Rate	56
46	7.2 Optical Cross Talk	57

47	7.3 Photon Detection Efficiency	59
48	7.4 Point of Operation Comparison	62
49	8 further analysis	63
50	8.1 multi incident probability and optical Cross Talk	63
51	8.2 Prompt and delayed cross talk ratio	63
52	9 Conclusion and Outlook	63
53	10 Glossary	64
54	11 Bibliography	65
55	12 Appendix	67

⁵⁶⁵⁷ 1 Cosmic Radiation

⁵⁸ Cosmic rays consist of a single particle with energies from 10^{10} to 10^{20} eV and describes extra-
⁵⁹ solar charged particles arriving on Earth and hitting the atmosphere fig(1). They were discovered
⁶⁰ by V.F. Hess in 1912 during the famous balloon flight experiments. He aimed to measure the
⁶¹ conductivity of air, that until then, was believed to be an insulator resulting in some problems
⁶² regarding the discharge of an electrically charged body, no matter how well it was isolated from
⁶³ the ground. Hess found the air's conductivity to increase with higher altitude, concluding the
⁶⁴ presence of a large amount of ionizing radiation above the atmosphere. The most energetic
⁶⁵ laboratory based accelerators operate in the 10^{12} eV energy range.

⁶⁶ Cosmic rays do not include those low energy particles originating from our sun. With a particle
⁶⁷ energy up to 1keV, those are referred to as solar wind, which means, by definition, cosmic rays
⁶⁸ arrive on Earth from outside our solar system. They consist of 87% protons, 12% α -particles
⁶⁹, 1% heavier nuclei and some electrons. High energy cosmic rays hitting Earth are very rare,
⁷⁰ averaging to one per year in an area of one square kilometer. Except at those very high energies
⁷¹ ($>10^{18}$ eV) cosmic rays will not reach earth directly and can not be observed to pinpoint
⁷² their source. Traveling through the interstellar medium, they get scattered by the interstellar
⁷³ magnetic fields, the cosmic microwave background and other hindrances and therefore have
⁷⁴ lost all directional information. However, directly observable cosmic rays, for example at the
⁷⁵ Pierre-Auger Observatory, provide an insight into cosmic particle accelerators.[2]

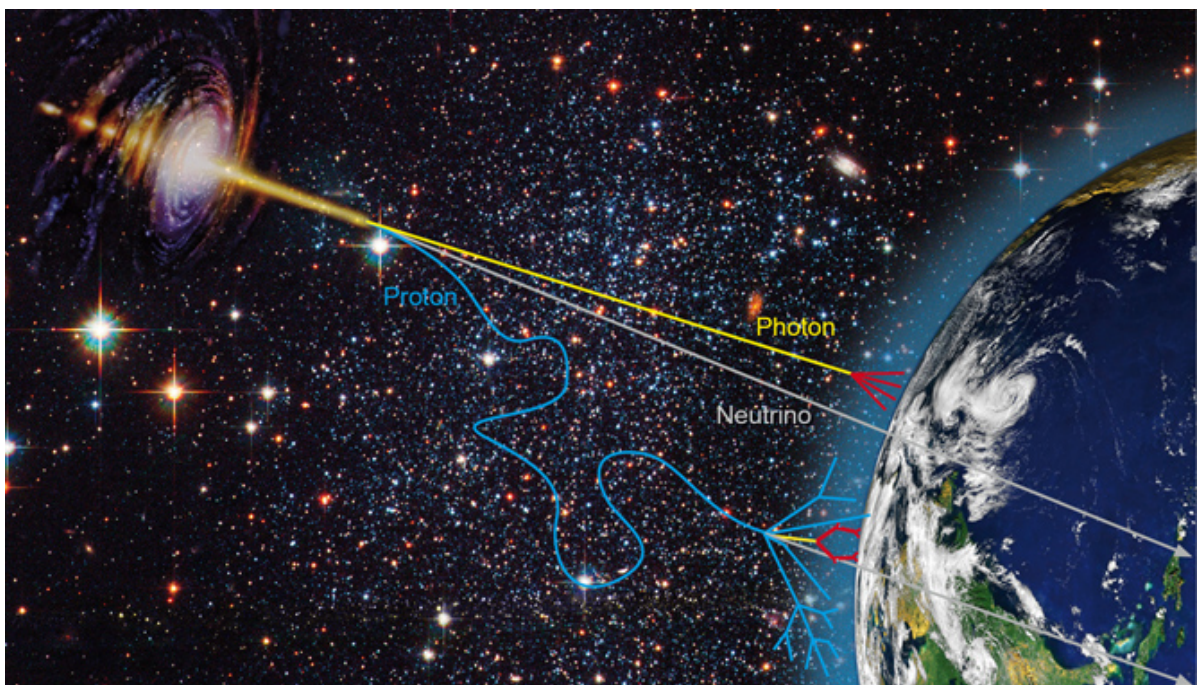


Figure 1: Gamma radiation photons (yellow) and scattered cosmic ray protons (blue) from an astrophysical source arriving on Earth. Neutrinos (grey) mostly do not interact. Picture from [26]

76 Cosmic rays of the higher energies are therefore observed via a detour: Gamma radiation.

77

78 Gamma radiation cannot be generated by
79 thermal emission of hot stellar objects, the
80 only event with a high enough temperature
81 to produce thermal radiation in the range of
82 GeV and TeV gamma radiation would be the
83 big bang, there is and has been nothing else
84 in the known universe. If thermal radiation
85 reflects the temperature of the emitting body,
86 what do gamma rays tell us?

87 Gamma radiation probe a non-thermal uni-
88 verse. In this one needs other mechanisms
89 to concentrate large amounts of energy into a
90 single quantum. The possible emission mechanisms are outlined below.

91 There are many diverse mechanisms of emitting gamma radiation. Gamma rays are generated
92 by high relativistic particles, in a first step for example: accelerated by the shockwave of a su-
93 pernova explosion. Those cosmic rays then collide with ambient gas, interact with photons or
94 magnetic fields, by inverse compton scattering, emitting high energy photons (down-top). Very-
95 high-energy (VHE) gamma radiation is defined as gamma radiation in the energy range of 10^{11}
96 to 10^{14} eV.

97

98 One such source of VHE gamma radiation and also the most famous, because the first to be
99 discovered, lies within the Crab Nebula. The Neutron Star located inside the Crab Nebula is a
100 Pulsar and the remnant of Supernova1054 and steadily emits gamma radiation energies up to
101 80 TeV. Another compound of the gamma radiation here is the so called Pulsar Wind Nebula. It
102 is composed of highly relativistic charged particles from the Pulsars giant rotating magnetic field
103 interacting with the expanding Supernova remnant via inverse compton scattering. Supernova
104 shockwaves themselves can also drive atomic nuclei to high energies which in turn emit observ-
105 able gamma-rays in a top-down fashion. Additionaly, binary systems consisting of a black hole
106 or pulsar orbiting a massive star can emit a flow of high-energy particles with variing intensity,
107 based on the elliptical orbit, where particle acceleration conditions vary.

108 So just like thermal radiation reflects the temperature of the emitting object, the flux and en-
109 ergy spectrum of the gamma rays reflect the flux and spectrum of the high energy seed particles,
110 coming from the source. So they can be used to trace these cosmic rays and electrons in distant
111 regions of our own galaxy or even beyond.

112 One surprise was the discovery of so called "dark sources" , objects emitting VHE gamma-rays,
113 but have no counterpart in other wavelenghts, meaning those objects might only be observable



Figure 2: FermiLAT Picuture from [27]

114 through gamma-rays. In extragalactical regions, gamma rays provide information on active
115 galaxies, where a constant stream of gas feeds a supermassive black hole at the center, releasing
116 enormous amounts of energy. From there, gamma rays are believed to be emitted, giving insight
117 into one of the most violent but to date poorly understood environments in our universe.

118 Even higher energy gamma rays could also be the product of decays of heavy particles, like
119 dark matter or cosmic strings. They therefore also provide a window to the discovery of dark
120 matter.

121

122 Gamma Radiation carries unique information about the most energetic phenomena in our
123 universe. The only problem is, our atmosphere is opaque for gamma radiation, gamma ray as-
124 tronomy in the lower energies is done by satellite based instruments like FermiLAT. The Large
125 Area Telescope, the principle scientific instrument on the Fermi Gamma-Ray Space Telescope
126 Spacecraft sensitive in the energy range between 20 MeV and 100 GeV, launched in June 2008.
127 fig (2) To reach the higher energy range through space based telescopes is very inconvinient,
128 since the required mass the telescope active area would need to detect the gamma rays increases
129 with gamma ray energy, and can therefore by very expensive to launch into space. Low energy
130 gamma rays can be efficiently captured by a volume appropriate for a spacecraft, for higher en-
131 ergy gamma rays using other interaction and detection media, like water or Earths atmosphere,
132 is more viable.

133 1.1 Air shower induced Cherenkov Radiation

134
135 The effect of gamma radiation on Earth is visible through gamma-ray induced particle cascades.
136 When a primary particle, i.e. a gamma photon or cosmic ray enters the atmosphere and collides
137 with a nucleus of the air, it gets scattered and creates secondary electrons, positrons and pho-
138 tons. Those secondary particles also interact with the atmosphere creating a cascade of particles
139 called a particle shower.

140 In this air shower, the initial and each subsequent particle traveling through our atmosphere
141 emitts Cherenkov light. Cherenkov radiation is a phenomenon caused by charged particles trav-
142 eling faster than the local speed of light would allow in that medium. This light is emitted in a
143 narrow cone with an increasing angle as the particles travel downward. This Cherenkov light
144 shows as a very short ($\sim 5\text{ns}$) flash with a peak in the UV-spectrum at around 330nm. Thus, we
145 can image the particle cascade measured with the telescope and can reconstruct the direction
146 and energy through a stereoscopic image of the shower taken by multiple telescopes (see sec-
147 tion A), reconstructing the position of the source in the sky. Is is also possible to reconstruct the
148 energy of the original photon from the amount of light produced, because energy is conserved,
149 so all energy of the original photon is now distributed between the particles of the shower.

150 To determine whether it is a hadronic shower, originating from cosmic rays, or a gamma shower,

151 originating from gamma ray photons, the shape of the shower and so called Hillas parameters
152 are used to determine the difference.

153 1.2 Imaging Atmospheric Cherenkov Telescopes

155 The technique, pioneered by the Wipple Collaboration,
156 behind the ground based experiments called Imaging
157 Atmospheric Cherenkov Telescope (IACTs) aims at
158 measuring the time, direction and energy of flashes
159 of Cherenkov light from extensive air showers caused
160 by VHE gamma radiation. Those ground based instru-
161 ments have a much larger effective detection area than
162 any satellite based instrument, which have a typical de-
163 tection size of 1m^2 . The range of the Cherenkov flash
164 being between 300-600nm, current generation Silicon
165 Photomultipliers (SiPMs) are a promising candidate to
166 replace the progenitor photon detector used in previ-
167 ous experiments like HESS, the Photomultiplier Tube
168 (PMT).

169 Current ground based IACT experiments are HESS,
170 MAGIC and Veritas. (see section B) HESS is the ...
171 Namibia consists of four telescopes the size of Xm op-
172 erating in the energy range of eV - eV. The recent HESS
173 upgrade added a fifth larger telescope in the center
174 of the array covering the xeV to XeV energy range.
175 MAGIC.... Veritas....

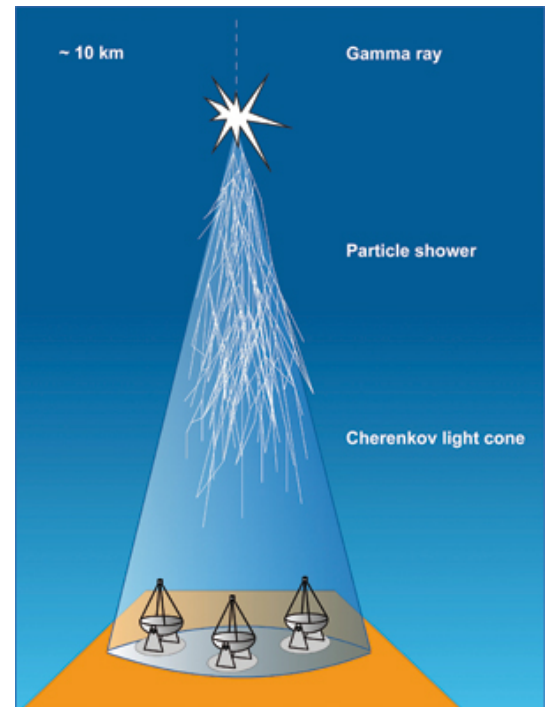


Figure 3: The cone of Cherenkov light emitted by an extensive air shower. Picture from [28]

176
177 _____ > HESS 5 3 GeV to 100 TeV MAGIC 2 30 GeV and 30 TeV VERI-
178 TAS 4 50 GeV - 50 TeV

179
180 _____ >
181 All of those arrays consist of at most 5 telescopes spread over a wide area. So most cas-
182 cades are viewed by only 2 or 3 of the telescopes. Additionally, due to the low flux of VHE
183 gamma radiation, detectors for this energy range are spread over a large area, making space
184 based instruments, which detect the incident gamma ray, an inconvenient choice. Another de-
185 tection concept for VHE gamma radiation are ground based air shower particle detectors such
186 as the High-Altitude-Water-Cherenkov observatory (HAWC) [6]. It employs a similar detection
187 principle, recording shower particles reaching arrays of ground based particle detectors filled
188 with water as detection medium, in contrast to air in IACTs. Those have the advantage of a

¹⁸⁹ larger duty cycle than IACTs, as they are able to operate during the day. Their limited sensitivity
¹⁹⁰ even with high observation time however will not allow them to compete with the sensitivity
¹⁹¹ and resolution of IACTs such as in the CTA. The array will however be able to provide useful
¹⁹² complementary information.

¹⁹³¹⁹⁴ 2 Cherenkov Telescope Array

¹⁹⁵ The Cherenkov Telescope Array, CTA, is a
¹⁹⁶ proposed ground-based observatory array of
¹⁹⁷ many tens of telescopes distributed over a
¹⁹⁸ larger energy range than before. It will al-
¹⁹⁹ low detection of gamma rays over a large
²⁰⁰ area on the ground and from multiple differ-
²⁰¹ ent directions. The array will consist of 60 -
²⁰² 100 telescopes of different designs and sizes
²⁰³ to cover the aimed for energy range and area.
²⁰⁴ Science goals are the understanding of cosmic
²⁰⁵ rays and their role in the universe, including
²⁰⁶ the study of cosmic particle accelerators, such
²⁰⁷ as pulsars, pulsar wind nebulae , supernova
²⁰⁸ remnants and gamma ray binaries. Secondly
²⁰⁹ particle acceleration around black holes of su-
²¹⁰ permassive or stellar size and lastly physics
²¹¹ beyond the Standard Model. There are currently three groups of telescopes planed, differing in
²¹² their size and achievable energy range:[2]



Figure 4: SST The GCT Structure with mounted
CHEC-M at meudon obs paris

- ²¹³ 1. LST¹ The low energy instrument, between 20 and 200 GeV, is a 23 meter class telescope
²¹⁴ with a moderate field of view (FoV) of the order of about 4.5°.
- ²¹⁵ 2. MST² The medium energy range, from around 100 GeV to 10 TeV, is covered by a telescope
²¹⁶ of the 12 meter class with a FoV of 7°.
- ²¹⁷ 3. SST³ The high energy instrument, operating between a few TeV to 300 TeV, is a 4 meter
²¹⁸ telescope with a FoV ranging from 9.1° to 9.6°.

²¹⁹ There are currently two sites planed, which when deployed, will achieve full-sky coverage. The
²²⁰ southern site in the Atacama Desert in Chile, one of the most driest and isolated regions on
²²¹ Earth, will consist of four LSTs, 24 MSTs, and about 70 SSTs covering an area of 4 km². The
²²² northern site will only cover 0.4 km² and will only contain four LSTs and 15 MSTs due to spac-
²²³ ing reasons with the MAGIC observatory at the same location at the Roque de los Muchachos
²²⁴ Observatory on La Palma, one of the Canary Islands.

²²⁵
²²⁶ One proposed concept for the SST is the Gamma Cherenkov Telescope (GCT) fig(4).

²²⁷
¹ LST large sized telescope
² MST medium sized telescope
³ SST small sized telescope

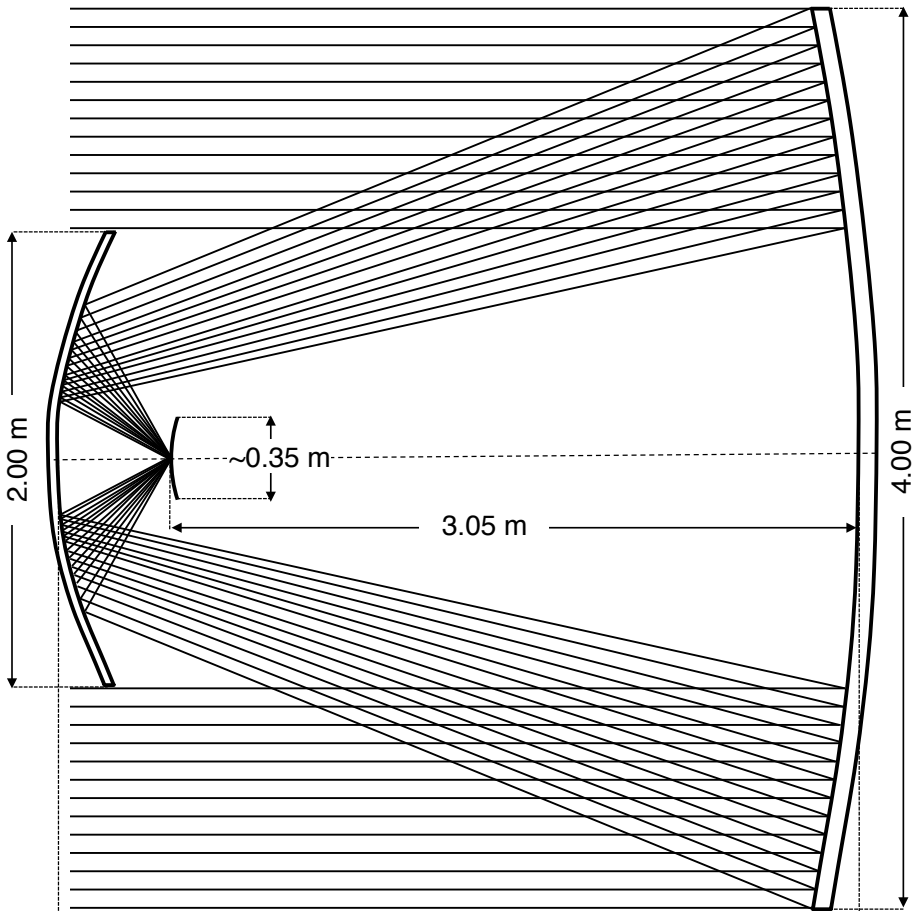


Figure 5

228 2.1 GCT

230 The reflector design of IACTs traditionally consists of multiple mirror segments, which focus the
 231 incident light onto a camera covering ~ 1 m with pixels ~ 25 mm in diameter. Such a reflector
 232 design is proposed for both, the LST and the MST of CTA resulting in the telescope sizes men-
 233 tioned in Section 2 above, that will use the traditional PMTs fig(7)(left).

234 For the SST such a design would result in a cheap telescope structure, but a disproportionately
 235 expensive camera, i.e. the cost and size of the structure is reduced, while the cost of the camera
 236 is not. The cost of one SST camera would be near the cost of a MST camera, which given the
 237 number of SST telescopes at the southern site is inconvenient.

238 The alternative solution is the reduction of the camera plate scale through a dual-mirrors de-
 239 sign allowing the use of more affordable photosensors. The optical system of the telescope is
 240 complemented with a secondary mirror added to the primary mirror. This shortens the effective
 241 focal length so the focal surface will lie between primary and secondary mirror fig(5). This
 242 optical design is based on the Schwarzschild-Couder design first produced by Karl Schwarzschild
 243 (Schwarzschild, 1905) and later refined by Couder (Couder, 1926) and then adapted for use
 244 in IACTs by Vassiliev and Fegan [10]. With the dual-mirror design optimised for GCT by Blake

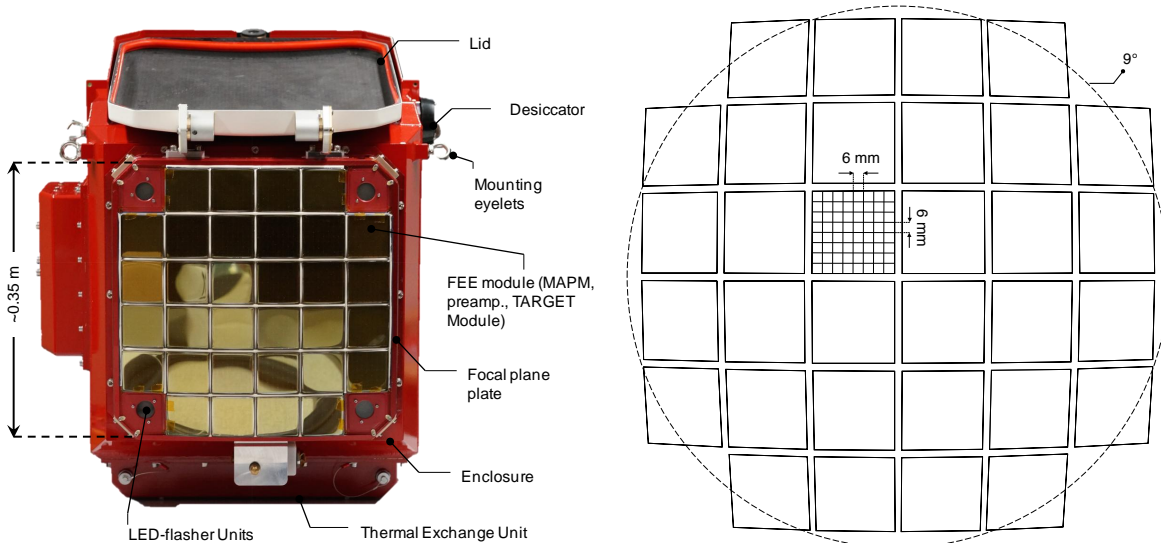


Figure 6: picture with GCT with mounted CHEC camera picture here Picture from

et al. [11] the camera plate scale is reduced, allowing the use of more affordable photosensors, Silicon Photomultipliers (SiPMs) and multi-anode photomultipliertubes (MAPMTs) among them, potentially reducing the cost of each SST.

2.2 CHEC

The Compact High Energy Camera, or CHEC is one of three prototype camera concepts in development for one of the SST structures within CTA. One camera features 2048 photosensors, building equally many readout channels per camera. The readout is done by so called TARGET⁴ modules for sampling, digitization and triggering, one of those consists of 4 ASICs⁵ with 16 channels each. The camera houses 32 TARGET modules, one of them responsible for readout of 64 photosensors. The TARGET modules build the front-end of the integrated electronics inside the CHEC camera connecting the buffer to the cameras backplane. After the photosensor is triggered the buffer amplifies the signal, that is then sent to the ASIC inside the TARGET module, where an analog-to-digital converter and a shaper convert the signal before it is sent to the backplane for transfer to the main array hub. Two iterations of the CHEC camera are tested, CHEC-M is the first design based on MAPMs as photosensors and was the initial prototype platform all improvements to the electronics are tested on. CHEC-M since then moved to Meudon in Paris and is now mounted on the GCT structure for further testing of the entire GCT prototype. The second iteration of the camera: CHEC-S, based on SiPMs as photosensors is a similar concept, with applied improvements to electronics and mechanical design. The two cameras are similar in shape and can both be mounted on the GCT structure with minor alterations.

⁴ TARGET TeV Array Readout with GS/s sampling and Event Trigger

⁵ ASIC Application Specific Integrated Circuit

266

267

268 In order to make an educated choice on the best SiPM device to use to populate the cameras
269 focal plane, an in-depth characteristic study on pulse-shape, gain, temperature-dependence,
270 detection efficiency, thermal noise and correlated secondary effects is conducted by multiple
271 groups within the CTA collaboration.

272

273

274 This paper studies the gain, noise from thermal, as well as correlated secondary effects and
275 their temperature dependence.

3 Silicon Photomultipliers



Figure 7: The size of the photodetector still used in progenitor IACT experiments (PMT)(left) compared to an SiPM(right). Picture from [23]

278 Silicon Photomultipliers (SiPMs) are semiconductor photo detectors, that have attracted in-
 279 creased attention over the last decade for their possible use in astroparticle physics. The sensor
 280 consists of an array of avalanche photo-diodes, typically $\sim 50 \mu\text{m}$ in size. Depending on the
 281 pixel-size, one pixel contains several 1000 diodes, hereafter called cells. Each cell is a PN junc-
 282 tion fig(8) supplied with a reverse bias-voltage above breakdown, which is called operation in
 283 Geiger-mode, in analogy to the Geiger counter. In this mode, a photon or thermal excitation will
 284 produce an electron-hole pair in the depleted region. Through impact ionization these charge
 285 carriers will in turn trigger an avalanche in a cell, which in turn generates a large output pulse
 286 typically in the range of several Mega electronvolt. This avalanche is then passively quenched
 287 by a resistor to limit the current in the substrate and to reset the cell to a quiet state so it is
 288 photosensitive again. The signal of the SiPM is the sum of the signal of all cells, read out over
 289 their quenching resistor via a common output.

290

291 3.1 SiPM characteristics

293 Silicon Photomultipliers posses major advantages over their progenitor, the Photomultiplier-
 294 tubes, or PMT fig(7). They are more resistent to mechanical and accidental light-exposure
 295 damage through ambient light. Silicon Photomultipliers have a lower power consumption and,
 296 operating at a much lower bias-voltage, there is no need for high-voltage as in PMT. They posses
 297 a high photon detection efficiency and are insensitive to magnetic field changes. There is rapid
 298 improvement, being a fairly new technology, with new generations every ~ 5 months and de-
 299 creasing costs per mm^2 . Viewed over all cells of the whole pixel, fluctuations in the gain are

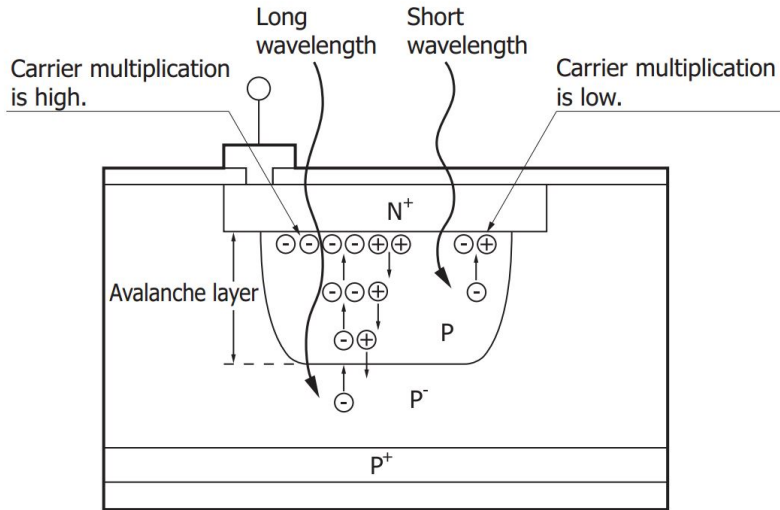


Figure 8: Structure and carrier multiplication through an avalanche inside a SiPM. Picture from [16]

300 very small. This is because of the uniformity during manufacture and visible in the width and
 301 the clear resolution of the p.e. peaks in the pulse area spectrum. Examples in the appendix G.
 302 MAPMs on the other hand posses larger gain fluctuations, which is due to their structure. These
 303 make Silicon Photomultipliers an interesting candidate in astrophysics experiments for both,
 304 space- and ground-based telescopes (or IACTs, Imaging Atmospheric Cherenkov Telescopes).
 305 However SiPMs also posses drawbacks, one of which is their temperature dependence through
 306 their Gain and Dark Count Rate. Another source of worry is their Optical Cross Talk, although
 307 manufacturers advance to reduce this source of noise.

308 Advantages:

- | | |
|---|---|
| 309 1. Sturdiness | 316 5. No need for HV as in PMTs |
| 310 2. May be exposed to ambient light (obser- | 317 vation during bright moonlight periods is |
| 311 possible) | 318 6. High Photon detection efficiency |
| 312 | 319 7. Insensitivity to magnetic fields |
| 313 3. Low power consumption ($\leq 50\mu\text{W}/\text{mm}^2$) | 320 8. Being a fairly new technology it is |
| 314 4. Low operation voltage (typically ~ 20 | 321 steadily improved, meaning a new gen- |
| 315 100 Volts) | 322 eration of SiPMs every 5months |
| | 9. Rapidly decreasing cost per mm^2 |

323 Drawbacks:

- 324 1. temperature dependence, Gain and Dark Count Rate
 325 2. Noise through Optical Cross Talk

326

327

328 Among the most desired characteristics is a high enough fill-factor (detector space versus dead
 329 space) to guarantee high Photon Detection Efficiency (PDE) 3.5. The peak of the spectral re-

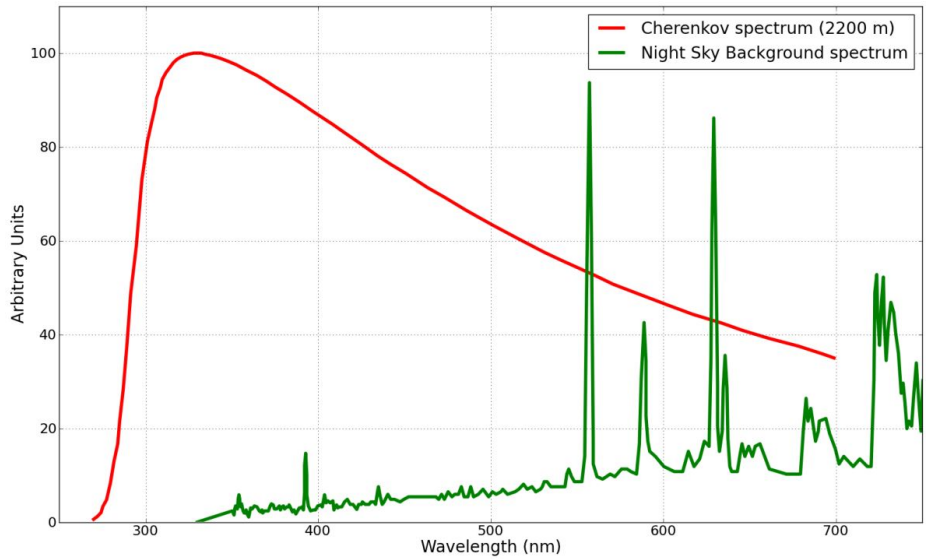


Figure 9: The spectrum of Cherenkov light observed from an extended air shower at 2200m asl. compared to the expected NSB measured in La Palma. Cut-off of the spectrum at wavelengths below ~ 300 nm due to atmospheric absorption. The emission peaks above ~ 550 nm in the NSB spectrum are mostly attributed to atomic oxygen, hydroxide and sodium in the atmosphere. Units on the y-axis are arbitrary because NSB and Cherenkov light vary by different parameters. There is a region between 550 and 650 nm, where the Cherenkov light spectrum and contributions from the NSB overlap. Image from [9]

330 response of the SiPM is desired to be around the spectral peak of the Cherenkov light at ~ 400 nm
 331 and at the same time, must have a fast enough drop to ensure less Night Sky Background (NSB)
 332 pick up (Figure(??)). The overall noise from thermal and correlated secondary effects of the
 333 SiPM must be sufficiently below the expected NSB rate at the location (usually around ~ 20 -80
 334 MHz).

335

336

337 =—————> Writing more later, see page 12 in pencil edited draft
 338 SiPMs could be suitable for application in IACTs and offer many potential benefits, however
 339 there are also potential drawbacks affecting their expectations from Cherenkov. The currently
 340 most challenging astrophysics experiment Silicon Photomultipliers are considered for use in
 341 Cherenkov telescopes, with very demanding expectations in terms of photon detection efficiency.
 342 The photon detection efficiency quantifies the absolute efficiency of any photon detector to
 343 absorb a photon and produce a measurable signal at its output. To achieve a high photon
 344 detection efficiency in the 450nm regime, the design moves to very thin implantation layers
 345 on the surface in order to minimize the absorption of shorter wavelength photons in insensitive
 346 areas. Figure(??) Different entry window coatings and avalanche structures (trenches etc.)
 347 explore the capable enhancements in the blue sensitive UV region.

348 349 3.2 Gain of a Silicon Photomultiplier

350 The gain of a Silicon Photomultiplier measures the internal conversion of a photon incident into
351 a signal at the output. The amplification of the device is expressed as the average number of
352 charge carriers produced. There is no distinction whether the incident was caused by a single
original photon or a thermal electron.

$$M = \frac{Q}{e} \quad (1)$$
$$Q = C \times (V_{bias} - V_{breakdown})$$

Figure 10: The gain (M) of a Silicon Photomultiplier results from the deposited charge (Q) of the pulse generated from one cell when it detects one photon, divided by the charge per electron (e). The charge deposited per event is proportional to the cell's capacitance (C) and the supplied over-voltage ($V_{bias} - V_{breakdown}$). [9] This results in the gain (M) in units of total number of charge carriers, usually in the several 10^6 range.

353
354 Estimation can be done via the voltage mean of the 1 p.e. amplitude: (e.g. see Figure (32)). For
355 a better understanding, stating the gain in units of mV per photoelectron or $\frac{mV}{p.e.}$ is more suitable,
356 as it gives a direct correlation between detected photoelectron and expected voltage amplitude.
357 Given the very narrow pulse shapes, using the average pulse amplitude and extracting FWHM
as a time measure of the total charge flowing during discharge and using the formula:

$$Q(p.e.) = C \times (V_{bias} - V_{breakdown}) \quad (2)$$
$$U(p.e.) = \frac{Q(p.e.)}{t(FWHM)} \times 50\text{ohm}$$

Figure 11: Resulting in the expected event charge flowing during capacitor discharge. Given the bias-voltage and C as capacitance of one cell and the resistance (50ohm) of the quenching resistor, a conversion factor and the average amplitude per photoelectron can be extracted.

358
359 The gain is obviously higher the larger the cell capacitance or the higher the bias-voltage (eq 1)
360 will be. But increasing the bias-voltage also increases dark counts and crosstalk. The gain is also
361 dependent on the temperature, mainly through the quenching resistor but also from the silicon
362 bulk itself, at a certain bias-voltage decreasing as temperature rises. The quenching resistor is
363 affected by a lowering of the electrical conductivity with rising temperature, in accordance to

364 the Wiedemann-Franz law, stating that the ratio of electrical and thermal conductivity remains
365 constant. The silicon bulk at rising temperatures underlies increased crystal lattice movement.
366 This impinges charge transport by increasing the probability that carriers might impact on the
367 lattice before the carrier energy has become large enough for continued ionization. In order
368 to counteract this, the electric field must be increased by increasing the supplied bias-voltage
369 so ionization is more likely. Doing this has drawbacks as discussed before. For application as
370 a photon detector, keeping the gain constant is an inevitable step, otherwise the shifting gain
371 leads to problems. To do that, either the bias-voltage need to be adjusted to match ambient
372 temperature, leading to problems with varying dark counts and crosstalk. Or the surface tem-
373 perature must be regulated to be kept constant. Although more challenging hardware would be
374 required, the latter option has obvious advantages, keeping dark counts and crosstalk and more
375 important the gain constant by simply regulating the surface temperature.
376 Taking into account equation 1, it appears that the breakdown-voltage can be estimated from
377 the zero-crossing of a linear extrapolation of the gain at every bias-voltage per temperature. By
378 doing this a linear breakdown-voltage dependence of the temperature can be observed. See
379 appendix E
380 When parametrized over over-voltage, the gain is essentially temperature independent.
381 For gain measurements see section 6.

382 3.3 Thermally induced dark counts

383 Inside the Silicon Photomultipliers depleted region a dark pulse originates from thermal exci-
384 tation of an electron to the conduction band. Without an event photon present to trigger the
385 avalanche, it is still indistinguishable from a photoelectron pulse. These thermally generated
386 carriers are observed along with the signal from a real photoelectron, presenting an irreducible
387 source of noise. The number of dark pulses observed is referred to as dark counts and the number
388 per second as the dark count rate. For applications that need to operate in an environment with
389 low noise, those dark counts are a concern. In IACT application of SiPMs however, this is only
390 a minor problem, since IACTs operate in a naturally noisy environment. Even though sky dark-
391 ness is one of the prime criteria of the proposed site selections for CTA, the surrounding NSB at
392 the most darkest side in Chile will still exceed any random noise in the detector. The pollution
393 of those NSB photons is unavoidable noise and will essentially limit the low energy resolution
394 of the telescope to the NSB rate. As long as any random noise, being dark counts or other, is
395 significantly below the NSB rate, it will not affect the telescopes performance.
396 Telescope performance simulations of the Schwarzschild-Couder MST of CTA at the site of
397 Chilec showed a rate of $\sim 20 - 80$ MHz per pixel for one of the older SiPM iterations from
398 Hamamatsu.[9] This is purely for NSB photons and pixels with a size of 6×6 mm², the cov-
399 ered range originates from differences in illumination level of the night sky by galactic- and
400 extragalactic-fields.

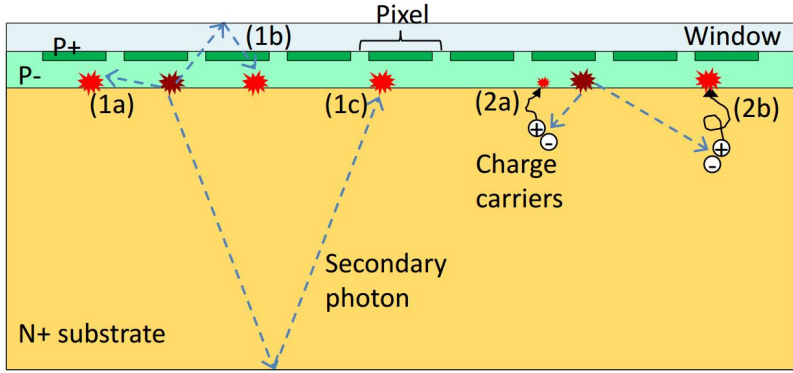


Figure 12: Secondary effects (bright red) caused by primary avalanches (dark red) in a Silicon Photomultiplier. In this paper a single pixel, in this figure, is referred to as a cell (see 3). Everything labeled under 1 is associated with prompt cross-talk, afterpulsing labeled as 2a, and delayed cross-talk labeled as 2b. Image adapted from [13]

402 403 3.4 Avalanche-induced secondary effects

404 An avalanche originating from the primary cell can sometimes, either directly or by reflection,
 405 propagate outside the cell and trigger an avalanche almost simultaneously in a secondary cell.
 406 This will, unless accounted for, degrade the Silicon Photomultipliers photon counting resolu-
 407 tion, since the signal will be a merge of cross-talk cells and real incident cells. This effect is
 408 referred to as the Optical Cross Talk, since it is conveyed via secondary photons generated in
 409 the primary avalanche. Afterpulsing also falls under this category, with the main difference to
 410 cross-talk being that the carrier triggers a secondary avalanche in the primary cell, basically gen-
 411 erating a parasitic pulse inside the previously fired cell. Contained in a single cell, afterpulsing
 412 increases the measured charge registered for an incident photon. The difference in arrival time
 413 of the secondary avalanche distinguishes different components comprising the cross-talk and
 414 afterpulsing. Those secondary avalanches can again emit photons, that can trigger secondary
 415 avalanches themselves, leading to high amplitudes, even in dark conditions. Cross-talk is de-
 416 pendent on the ability of the secondary photons to reach a neighboring cell. This means, that
 417 an increase in cell-size and therefore cell-area should directly correlate with the Optical Cross
 418 Talk of a pixel. The OCT dependency on the cellsize was tested and can be found in section C.
 419 Figure (12) shows different physical processes causing secondary effects in Silicon Photomulti-
 420 pliers based on their delay time. Cause of the delay time is the dependence on the penetration
 421 depth of the incident photon, or the region the dark count generated, and the diffusion time
 422 inside the substrate. At long delay times of up to 70ns afterpulsing and cross-talk are not
 423 distinguishable.[13] The prompt Optical Cross Talk happens basically simultaneous to the pri-
 424 mary avalanche, since it is unaffected by the primary cells recovery time and is labeled 1 in
 425 Figure (12). It is either triggered by the secondary photon directly (1a) reaching the neigh-
 426 boring cell, or after first reflecting on the surface layer (1b) or the bottom surface (1c). If the

427 cross-talk avalanche delay time is shorter than the detection resolution, the difference in signal
428 between an Optical Cross Talk event or an incitend photon being detected, is not observable.
429 Time delayed Optical Cross Talk is caused by a carrier generated in the non-depleted substrate
430 diffusing to a neighboring cell and triggering an avalanche in the depleted region (2b). If the
431 carrier stays in the primary cell, the triggered avalanche is labeled afterpulsing (2a) and will
432 have a lower amplitude, due to the cell not being recovered yet. The delay time is influenced
433 by how deep the carriers are being trapped in the substrate, the time they need to diffuse to the
434 surface, and also distinguished by traps with different lifetimes.
435 This is very important in IACT performance, since this effect gives random NSB and dark count
436 photons the ability to rise to larger amplitudes. The consequent need to raise the trigger thresh-
437 old to counteract the resulting rising accidental-triggerate has a negative impact on the low
438 energy resolution of the telescope.

439
440 Parametrized with over-voltage, the secondary avalanche effects are temperature indepen-
441 dent, for OCT measurements see section 6.

442 3.5 Photon Detection Efficiency

$$PDE = \frac{N_{\text{detected photons}}}{N_{\text{total photons}}} \quad (3)$$

Figure 13: Photon Detection Efficiency is the percentage of detected photons versus overall emitted photons.

442 The Photon Detection Efficiency is the probability of a detector to absorb an incoming pho-
443 ton and produce a measurable signal at its output, and depends on a number of factors. First
444 the photon must enter the depleted region via transmission through the surface of bare sili-
445 con, which has a reflectivity of 30%. However, the transmission probability can be improved
446 by coating the surface with a substrate with adequate thickness and a refraction index between
447 air $\eta_{\text{air}} = 1$. and silicon $\eta_{\text{silicon}} = 3.4$. Devices presented in this paper are coated with epoxy,
448 a silicon resin and glass. The coating also has the added benefit of insulating and protecting
449 the cells against environmental influence. A possible negative effect of coating is an increase in
450 prompt cross-talk and a larger dependency of the overall cross-talk on the cellsize. The second
451 factor is quantum efficiency, describing how susceptible the depleted region is to photons ex-
452 citing electrons from the valence band to the conduction band. This is sometimes referred to as
453 spectral response of a detector to reflect the wavelength dependence of a detector and makes
454 the PDE wavelength dependent. The over-voltage dependency of the PDE is conveyed by the
455 third factor, the avalanche probability. It depends on the electric field present, and thus on the
456 applied over-voltage. The last factor is the fill-factor: the more the surface area of the detector
457 applied over-voltage. The last factor is the fill-factor: the more the surface area of the detector
458 applied over-voltage.

459 is covered with active-area cells and the less dead-area exists between cells the higher the fill-
460 factor is.

461 The Photon Detection Efficiency is commonly measured by illumination of the pixel and a cali-
462 brated reference photodiode with a flashing light source, and determining the average number
463 of photons hitting the photosensor during a light pulse.

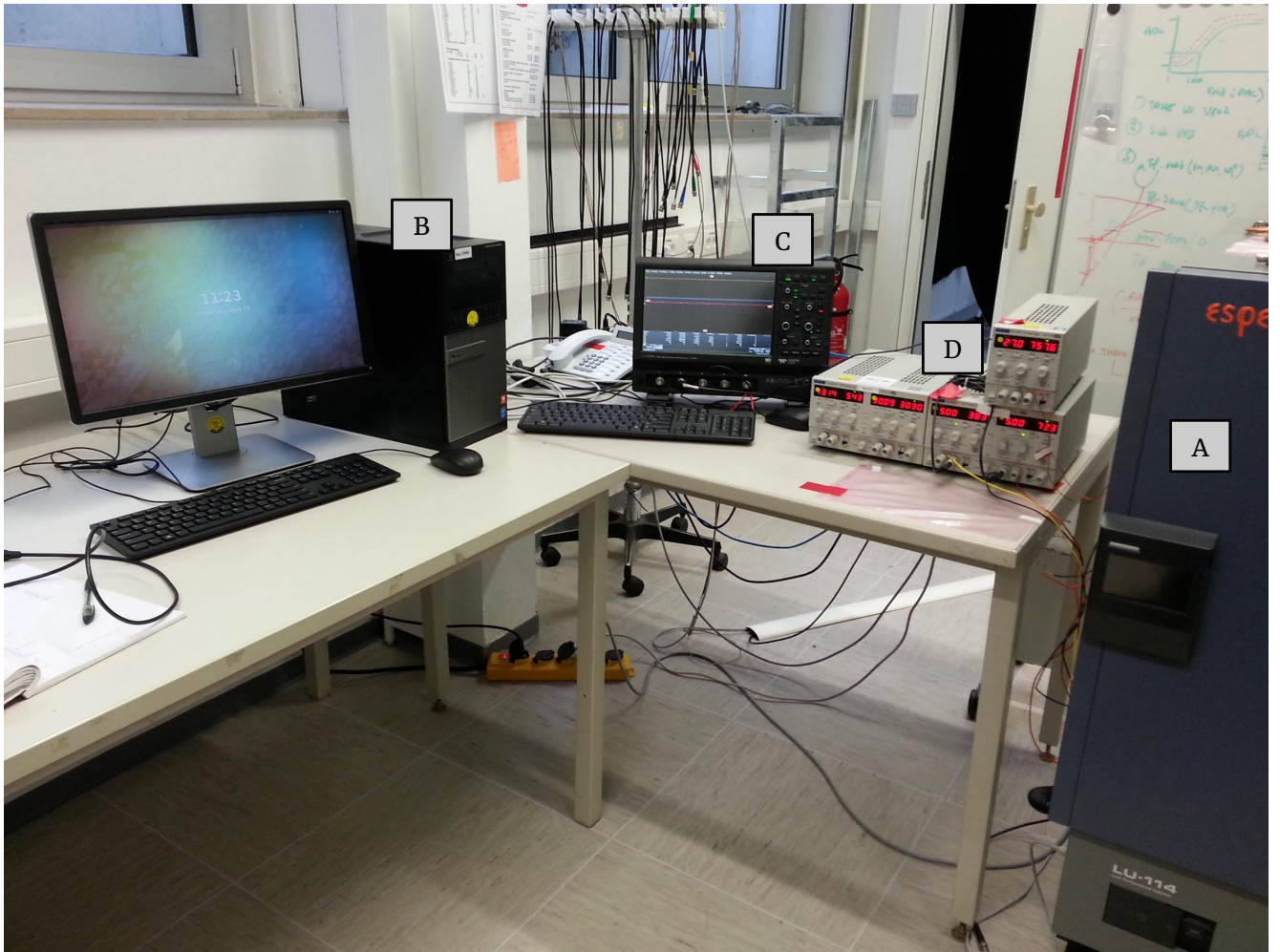


Figure 14: Outside pic Will be updated. With Alphabetical captions for the different steps and references later in the text and setup scheme below, Picture of the inside of the thermal chamber is missing, will do later, and try to fit it next to this one

464
465

4 Experimental Setup

466 The experimental setup in general is designed to house a variety of SiPM devices. Over the
 467 course of this paper, 5 different types of SiPMs were mounted on the setup and evaluated. It
 468 involves a thermal chamber Figure(65)(A) for temperature regulation which proved light tight
 469 and thus also serves as a dark box, to prevent any stray light to reach the SiPMs surface. The
 470 thermal chamber in question is a LU-114 constant climate cabinet from ESPEC with a pro-
 471 grammable interface for remote control. The chamber is able to raise and lower the inside
 472 temperature with a $\pm 0.5^{\circ}\text{C}$ accuracy, direct measurements of the SiPMs surface with a tempera-
 473 ture probe confirmed this. In the absence of light tests, heating of the SiPM surface through the
 474 dark current proved no concern.

475
476

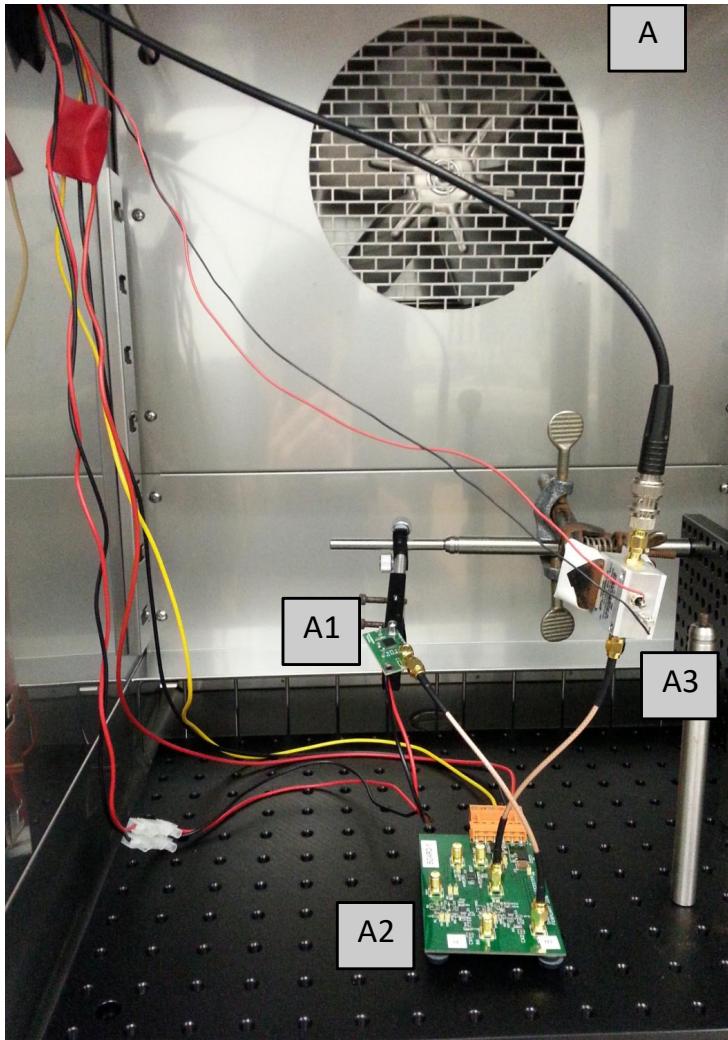


Figure 15: Inside Pic Will be updated. With Alphabetical captions for the different steps and references later in the text and setup scheme below, Picture of the inside of the thermal chamber is missing, will do later, and try to fit it next to this one

477 Depending if the SiPM Figure(65)(A1) in testing is pre-manufactured on a test-array or sup-
 478 plied as a standalone chip, it is either mounted directly on a mechanical arm inside the chamber
 479 in the former case, or in the latter the mechanical arm supports a specifically designed PCB
 480 connecting to the device. Via the mount, bias-voltage is supplied and signal is transferred to the
 481 shaper Figure(65)(A2). In some cases the output signals amplitude is too low to trigger the oscil-
 482 loscope, therefore amplification is needed. I used an amplifier from MiniCircuits Figure(65)(A3)
 483 supplied with different voltages depending on the tested device to amplify the shaped signal.

484

485 Data acquisition in the Laboratory is realized by a Lab-PC Figure(65)(B), that forms the
 486 central control station for multiple pieces of equipment. It is connected to the oscilloscope
 487 Figure(65)(C), which records the waveforms of the device in testing, and then sends the data
 488 back to the PC via ethernet. The oscilloscope is a Lecroy HDO6104 1GHz HS Oscilloscope capa-

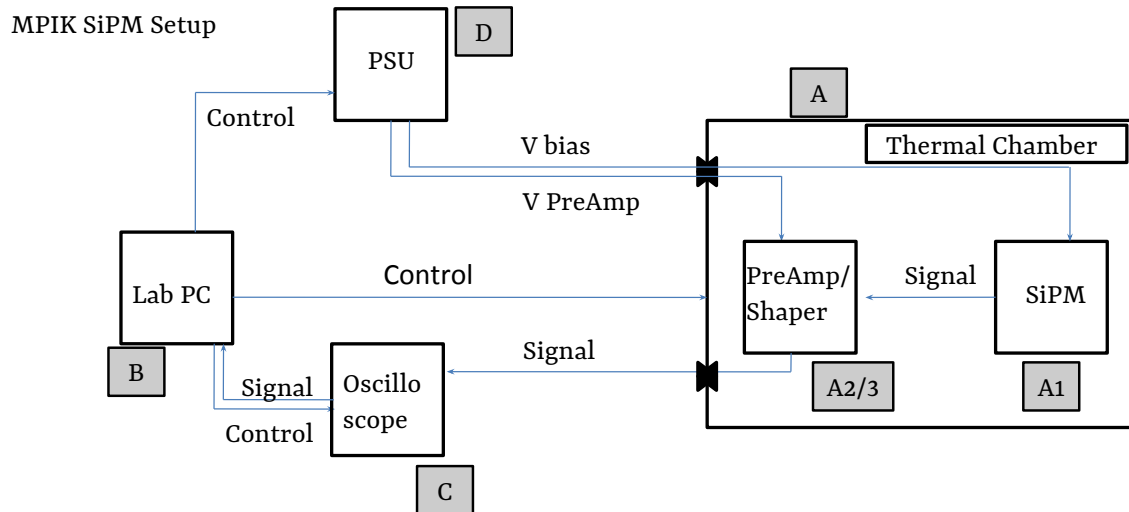


Figure 16: Experimental setup scheme, Annotations see text

ble of 2.5 GS/s.

490

491 The power supplies Figure(65)(D) control the bias-voltage of the Silicon Photomultipliers,
 492 ramping of the bias-voltage is controled by the PC. Lastly the thermal chamber is connected
 493 to the Lab-PC, where the data acquisition script controls the temperature, and continuously
 494 rechecks it during temperature ramps. Signal transfer from the shaper to the oscilloscope is via
 495 a throughput on the side. All equipment is connected via ethernet, plugged into a common hub,
 496 to form a local network. While the temperature of the thermal chamber is ramping from the
 497 previous to the next set-point, the data is send to the Lab-PC.

498

499

500 Temperature regulation is an issue in the teststand, as there is no way of controlling the SiPMs
 501 surface temperature. In dark conditions however, without conducting illumination tests, the
 502 shift in temperature on the SiPMs surface is only minimal. (Find the breakdown-voltage depen-
 503 dence on temperature in the appendix (??)). Checking the surface temperature of all devices
 504 with a temperature probe during testing showed minimal rising temperatures. So the influence
 505 of the temperature on the breakdown-voltage is only of minor concern. However, once illumina-
 506 tion tests begin, the rising temperature on the SiPMs surface will no longer be negligible and the
 507 temperature must be regulated, either by cooling of the surface or including the temparature
 508 parameter.

509

510

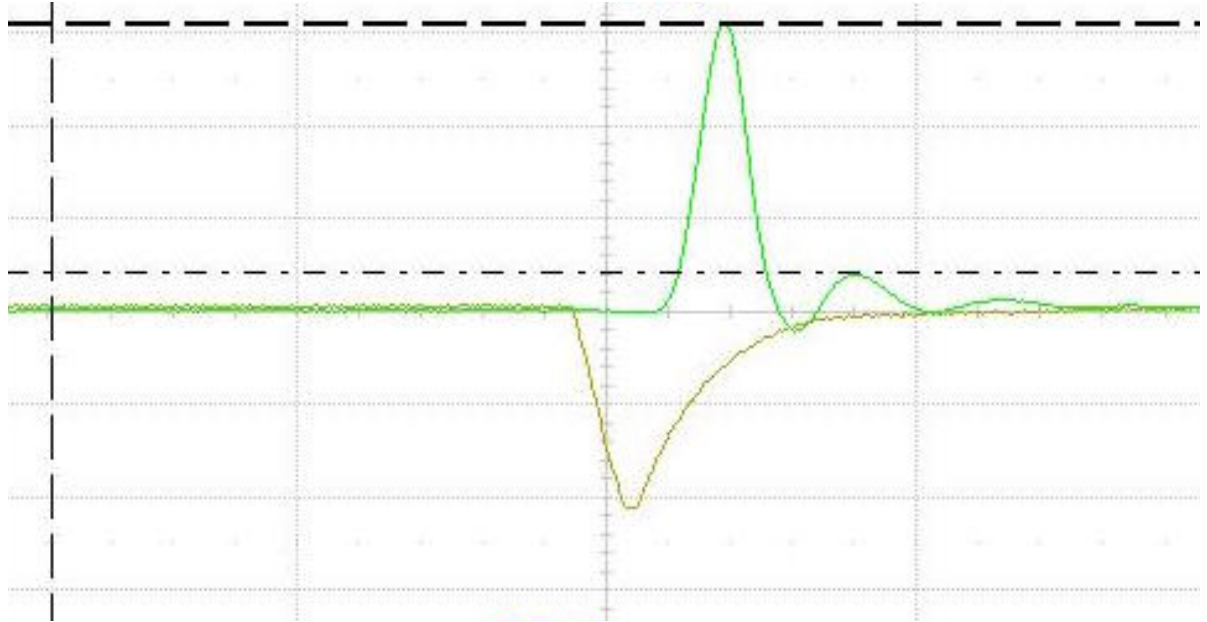


Figure 17: The shaped and unshaped pulse from a pulse generator emulating the output of the front-end buffer of the CHEC-S SiPM. The unshaped pulse in yellow and negative, due to the buffer-output. The shaped pulse now flipped through the electronics in green. Zoomed, Taken from [20]

511 The shaper consists of two stages, the main
 512 components are an Op-Amp amplifier serving
 513 as an input buffer followed by a zero pole
 514 cancelation circuit for pulse shaping and is
 515 commonly used in photon-counting applica-
 516 tions. A zero pole cancelation circuit is ba-
 517 sically a RC circuit eq(4) (C_Z , R_0) supressing
 518 the high frequencys to narrow the pulses from
 519 the usual ~ 50 ns to ~ 10 ns, using a high-pass
 520 filter with a tunable time constant, through
 521 f_C which gives control over the frequency re-
 522 sponse of the circuit.[21]

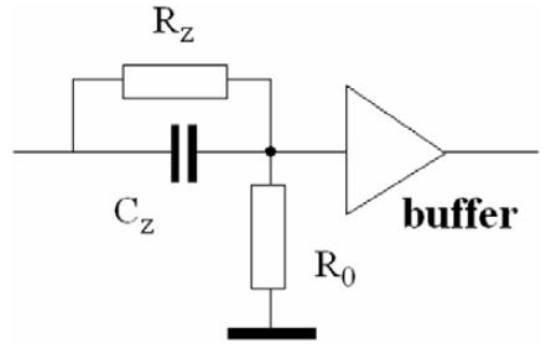


Figure 18: A Zero Pole cancelation circuit com-
 monly used in photon counting applica-
 tions. Taken from [21]

$$R_0 \times C_Z = 1/(2\pi \times f_C) \quad (4)$$

523 In Figure 17, reference by Luigi Tibaldo [20], the shaped and unshaped pulse is shown, the
 524 negative amplitude (yellow) corresponds to the unshaped signal mimiced by a function gen-
 525 erator to emulate the output of the front-end buffer of the CHEC-S SiPM, with a fall-time of
 526 approximately 9 ns followed by the exponential rise with 90 % to 10 % in 23 ns. These tests
 527 correspond to an initial design of the shaper and do not correspond to the final setup.

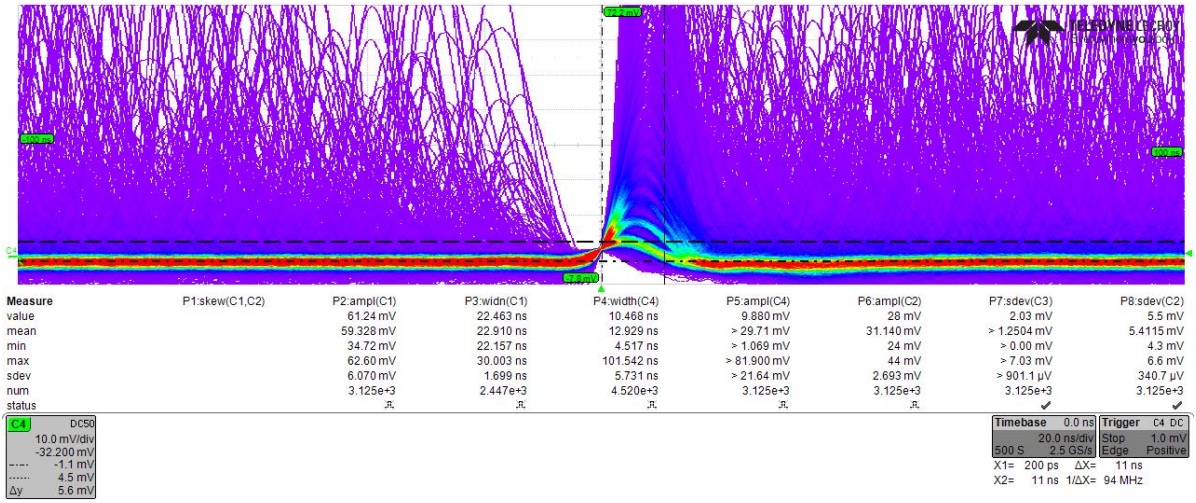


Figure 19: Persistence figure of the shaped pulse after adapting the electronics to a preferable pulse shape. In the center, a row of pulses with rising amplitudes is visible. These are the multiple N p.e. pulses, differing by $\sim 5\text{mV}$. The purple area off-center is due to delayed cross-talk and after-pulsing. Taken from [20]

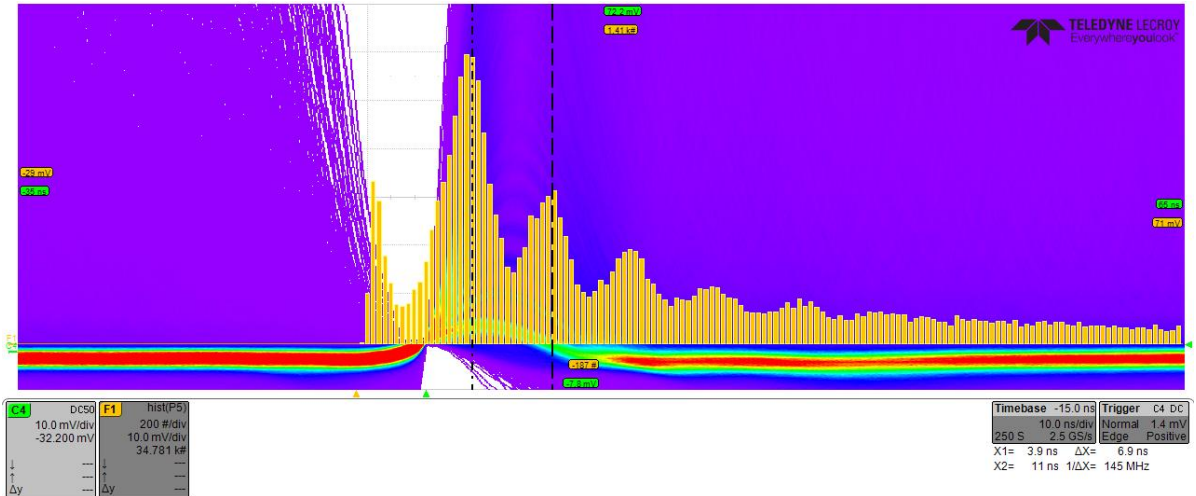


Figure 20: An oscilloscope based pulse height spectrum in the same scheme as the persistence figure fig(19). The distance between the peak maxima delivers an estimation of the gain of the SiPM at this bias-voltage. Taken from [20]

528 The shaper board contains tuneable capacitors (C9) and resistors (R20) (see schematic ap-
 529 pendix F), that can be optimized for ideal pulse layout. The green pulse in Figure 17 shows
 530 the output after shaping, with a width of FWHM of 9 ns. The amplification between input and
 531 output is approximately 6-7. The output pulse has some ringing after the main pulse, the first
 532 afterpulse has a 12 % amplitude relative to the main pulse. For the complete unzoomed Figure,
 533 see appendix F.

534

535 After tweaking the tunable electronics on the shaper to a preferable pulse shape, clear single p.e.

536 peaks are visible in a persistence plot. fig(19). The peaks have an amplitude of \sim 5 mV/p.e.,
537 from this and from the following, a gain estimate for the peak finding threshold in the anal-
538 ysis can be made. With the same configuration a gain estimate at different bias-voltages of
539 the SiPM is possible through an on-oscilloscope pulse height spectrum fig(20). The distance in
540 peak maxima is a reference to the gain of the SiPM, in the case of Figure 20 close to \sim 5 mV/p.e. .

541

542 This chain of shaper modification is done for every SiPM from Hamamatsu Photonics K.K.
543 tested in this paper (4 in total) as they arrived as a single unmounted device, in need of
544 shaping and amplification. The device from SensL is premounted on a test array, preshaped
545 and only externally amplified.

546 5 Data Analysis

548 The analysis of the Silicon Photomultiplier waveforms is done exclusively in python following
549 the sequence:

550

- 551 1. data conversion
- 552 2. pedestal subtraction
- 553 3. peak detection
- 554 4. gain extraction
- 555 5. calculation

556 The waveform data, after being transferred to a separate PC, is analyzed offline. The goal is
557 to extract event-data from the waveforms in order to produce pulse-area spectra for every bias-
558 voltage at every temperature. To that end, the pedestal of the electronic noise must be found and
559 subtracted from the data. After that, event-pulses are detected and integrated. This generates
560 a list of pulse-areas, which is in turn used to fill a pulse-area histogram. To this pulse-area
561 histogram, a model is fitted from which the gain can be extracted. Due to the linear behavior
562 of the gain with rising bias-voltage, a regression line is fitted, from which the Dark Count Rate
563 and the Optical Cross Talk are calculated using the original pulse-area histogram.

564 5.1 Tracefile Conversion

565 The oscilloscope produces the waveform data in its intrinsic data format, called a trace with
566 the data suffix trc in binary. A trace file contains a header and two binary lists, an amplitude
567 based on the oscilloscope's voltage-range and offset, and a list of the same length containing the
568 associated event-time, based on the time-range and horizontal offset. The first step is therefore
569 a conversion of the amplitude and associated event-time of all segments of a waveform trace
570 file into two lists of floats.

572 5.2 Pedestal Subtraction

574 A single waveform from the oscilloscope is
575 anticipated to be uncentered fig(21)(grey), it
576 will be slightly above or below zero, depending
577 on the device setup (some devices pro-
578 duce inverted signals). The signal is mixed
579 with electronic noise when it is observed
580 and forms a pedestal, shifting the mean of
581 the waveform from its original position to
582 zero. Pedestal subtraction removes this av-
583 erage noise.

584 The first step of the process is reading in the
585 uncentered waveform fig(21)(grey) and cal-
586 culating an initial mean(mean0), expected to
587 be slightly higher than the actual mean of the
588 noise, due to the presence of event-pulses.
589 The waveform is then shifted to about zero,
590 by subtracting the mean0. A second mean of the now nearly centered waveform is taken
591 (mean1). Now a new, same-sized array is formed and filled with the data from the wave-
592 form that is smaller than mean1, this represents the negative part of the noise. The data larger
593 than mean1, the positive noise, is also filled into the array, but is negative-signed. This cre-
594 ates an array of the waveform centered around zero and, above the mean1, folded towards the
595 negative. It proved reliably, that calculating the root-mean-square of this helper-array is a solid
596 possibility of stripping the waveform of event-peaks. Taking the root-mean-square with a factor
597 3 of the helper-array, a cut is now applied to the waveform on both, the positive and negative
598 side. In that fashion, the remnant is the waveform between the positive and the negative root-
599 mean-square and is now called a peakless-signal, representing the noise of the waveform.
600 Pedestal subtraction is done by calculating the mean of this peakless signal and subtracting
601 it from the waveform. After that, the peakless signal is also smoothed by convolving it with
602 a wide-windowed gaussian and subtracted from the waveform to eliminate any slow moving
603 noise, the resulting waveform is called "Filtered Signal 1" fig(21)(blue).

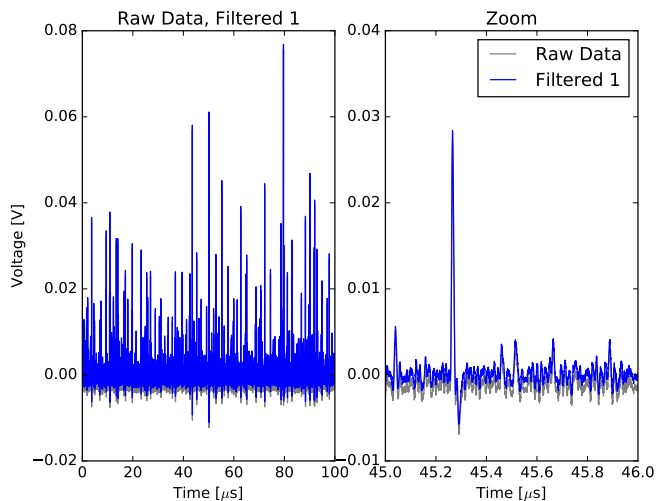


Figure 21: Raw, real data from a HPK SiPM in grey, in blue the pedestal subtracted and smoothed "Filtered Signal 1"

604 605 5.3 Peak Detection

606 Peak detection exploits the fact, that the first
607 derivative of an event-peak will cross zero
608 into the negative at the time of the peak max-
609 imum. The presence of random noise in the
610 signal however will lead to many false de-
611 tections. Therefore, before the detection of
612 the event-peaks, the waveform fig(22)(grey)
613 is smoothed with a narrow-window gaussian
614 with a width of about the FWHM of the de-
615 vices characteristic event-pulse, in order to at-
616 tenuate non-event peaks fig(22)(blue). After
617 the first derivative of the signal is calculated,
618 which in python is a fast process if using ar-
619 rays, a number of parameters decide the va-
620 lidity of the detected peaks. Most important
621 parameters are a certain predetermined mini-
622 mum amplitude, called the amplitude thresh-
623 old or: minimum peak height. This is determined from initial examination of pulses on the
624 oscilloscope and entered as a parameter to the analysis chain, but could later be calculated
625 based on the noise level. The second important parameter defining validity is the minimum
626 peak distance, which defines how close two events can occur after another. The value is deter-
627 mined by the FWHM of the device in testing, which is expected to be sensible enough to resolve
628 two events happening close after another. The peak detection algorithm can not distinguish
629 between instantaneous and delayed Optical Cross Talk, but nonetheless, due to the fact, that
630 the signal data is taken over many micro-seconds, all events are detected, independent of their
631 source. On the other hand, this also means, that it is possible for two events to happen at the
632 same time, for example a real photoelectron-event coinciding with delayed Optical Cross Talk or
633 two simultaneous dark events being misinterpreted as one dark event + its prompt cross-talk.
634 This can not be distinguished and will lead to a slight shift of the amplitude, due to the mostly
635 lower amplitude of afterpulsing and cross-talk events.

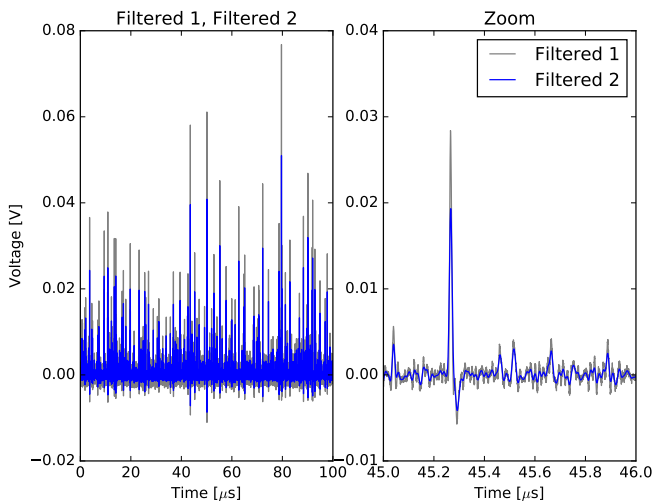


Figure 22: "Filtered Signal 1" in grey before
smoothing with a narrow gaussian to
generate "Filtered Signal 2" in blue,
which is used for peak finding.

5.4 Gain Extraction

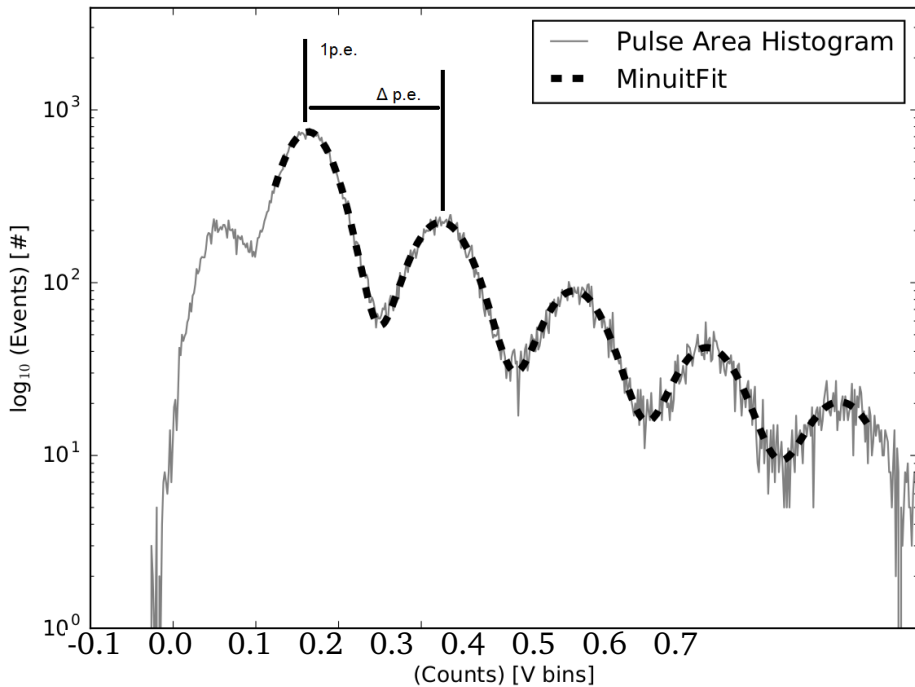


Figure 23: Pulse Area Histogram of a HPK S12642 with 1p.e. and Δ p.e. positions. Multi gaussian fitted function eq(5) as black dashed line.

638 The detected peaks are integrated with a window extending symmetically from the peak
 639 maximum, the width is chosen as slightly wider than the peaks FWHM. The generated list of
 640 peak areas is generating a peak area histogram, which is fitted with a function of multiple
 641 gaussians eq(5) using iMinuit in python, seen in Figure (23). To determine the number of
 642 gaussians to fit, another function checks the viability of each N p.e. peak, among the checked
 643 parameters is the ratio in height to the 1 p.e. peak and the absolute peak-height of the checked
 644 Nth p.e. peak in the histogramm.

$$(N \times \left[A \times e^{-\frac{[(x - (\bar{x} + N \times \Delta x))^2]}{2 \times \sigma^2}} \right]) \quad (5)$$

Figure 24: The fit function of multiple gaussians with equal spacing. N is the multiplicity of the
 function or range the fit function is to be applied. A is the Amplitude of the N th p.e.
 peak with σ , \bar{x} is the x-position of the 1 p.e. peak, Δx is the p.e. spacing distance.

645 Two parameters are extracted from the fit to the peak area histogram. The first \bar{x} , the position
 646 of the 1p.e. peak is the position of the maximum of the first peak in the histogram, and the
 647 position of corresponding multiple p.e. events should be integral factors of the 1p.e. position.

648 This proved to not be the case for some devices, the suspected source of this error is a pedestal
649 generated during the peak integration. For a more detailed study of the effect of the integration
650 window see section 5.5.

651

652 A second parameter is extracted from the
653 peak area histogram to deal with this prob-
654 lem, which is the distance between N p.e.
655 peak maxima of the histogram, labeled Δ p.e.
656 , which defines the gain. The apparent
657 pedestal of the pulse area histogram makes
658 extraction of the two parameters necessary in
659 order to calculate the Dark Count Rate and
660 the Optical Cross Talk. The gain of a Sili-
661 con Photomultiplier has a linear dependence
662 of the supplied bias-voltage. Given that the
663 bias-voltage range is deliberately chosen such
664 that the over-voltage ranges from about 1V
665 growing upwards, the range of linearity only
666 starts at around the point of operation given
667 by the manufacturer of the device. At the
668 higher end of the bias-voltage range the be-
669 haviour usually starts to divert from the linearity. In order to get an estimation of the gain over
670 a large range, both previously extracted parameters, the 1p.e. peak and the distance Δ p.e. are
671 fitted with a linear regression line. The fit assumes linearity utilizing weighted least squares in-
672 herited from pythons statsmodels package. For the fit, only the data, where at least 3 gaussians
673 are fitted to the peak area histogram is taken into account. Plotting both extracted parameters,
674 as well as their respective regression lines versus bias-voltage, as in Figure (25), shows the dif-
675 ference between the two parameters. Comparing the manufacturer supplied breakdown-voltage
676 from the datasheet for all devices showed, that the zero-crossing of the 1p.e. regression line
677 is more consistent with datasheet values, in contrast to the zero-crossing of Δ p.e. , which lies
678 slightly higher. The over-voltage, corresponding to the set bias-voltage at any given temperature
679 is calculated from this breakdown-voltage.

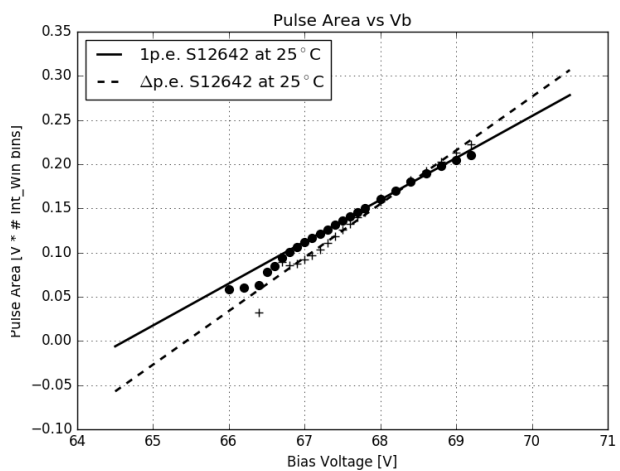


Figure 25: 1p.e. position and Δ p.e. extracted from the Pulse Area histogram at every bias-voltage for HPK S12642 with their respective regression lines.

680 Dark Count Rate and Optical Cross Talk are calculated utilizing 1p.e. position and Δ p.e.
681 derived from the regression line. Both values are applied, in the calculation, to the peak area
682 histogramm with the Dark Count Rate being defined as:

$$DCR = \frac{N_{events(\geq 0.5p.e.)}}{T_{experiment}} \quad (6)$$

Figure 26: The Dark Count Rate of a Silicon Photomultiplier is defined as all events exceeding 0.5 p.e. in amplitude $N_{events(\geq 0.5p.e.)}$ occurring over the experiment time $T_{experiment}$. Included in the measurement are thermally generated dark counts, as well as delayed cross-talk and afterpulsing with only a minor contribution.

, and the Optical Cross Talk as:

$$OCT = \frac{N_{events(\geq 1.5p.e.)}}{N_{events(\geq 0.5p.e.)}}. \quad (7)$$

Figure 27: The Optical Cross Talk of a Silicon Photomultiplier is defined as all events exceeding 1.5 p.e. in amplitude [$N_{events(\geq 1.5p.e.)}$] divided by all events exceeding 0.5 p.e. in amplitude [$N_{events(\geq 0.5p.e.)}$]. It scales with the number of photons produced inside an avalanche, as well as the probability of these photons to trigger a neighboring cell

684 5.5 Data Challenges

686 687 5.5.1 The influence of the minimum peak distance

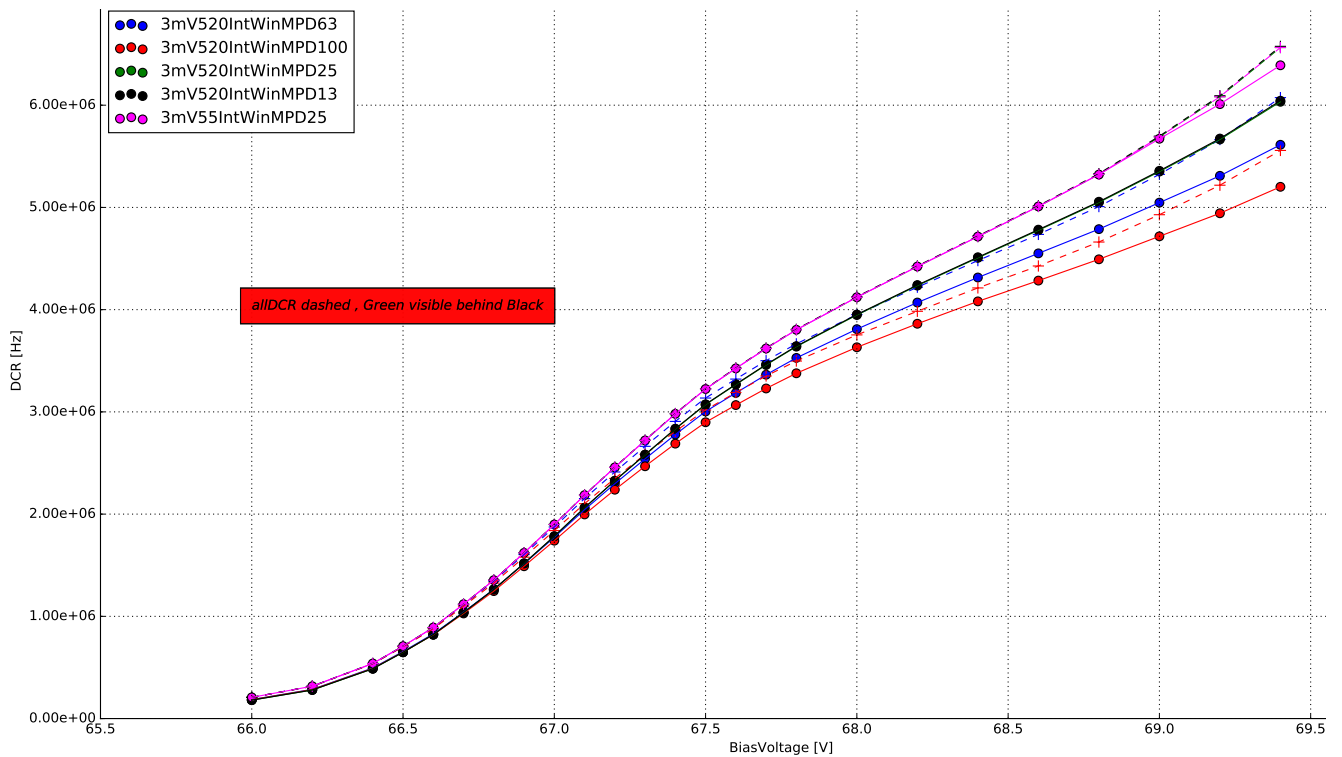


Figure 28: The difference between 4 minimum peak distance windows, in time-bins, during the peak detection. The dashed lines are the Dark Count Rates considering all recorded events, forming an upper limit. In pink, the effect of a different integration window is shown.

688 The influence of the minimum peak distance is shown in Figure (28) . Based on their bin-
689 width, four different windows are tested. With the oscilloscopes sampling rate of $2.5 \frac{GS}{s}$, the
690 windows of 100, 63, 25 and 13 time-bins, correspond to 40, 25, 10, 5 ns windows respectively.
691 With a event pulse FWHM of 10ns, setting the minimum peak distance to 100 bins, resulting
692 in a 40ns window is visibly to large, as the algorithm will skip over valid data Figure (28)(red).
693 After an event is detected, skipping over 40ns worth of data will result in errors of the Dark
694 Count Rate, since the calculation uses the complete experiment time. Therefore a more reliable
695 distance window must be chosen. The second window of 25ns was the next approach, origi-
696 nating from the length of the pulse-tail fig(28)(blue). This would lead to no detected events
697 overlapping with the tail of one previously detected, resulting in a sharper pulse-area spectrum.
698 Compared to a window of approximately the pulse FWHM, the previously discussed window
699 would still lead to lost event-data. Since the sharpness of the pulse-area spectrum is already
700 sufficient, a window around the pulse FWHM was chosen as reference for all measured de-

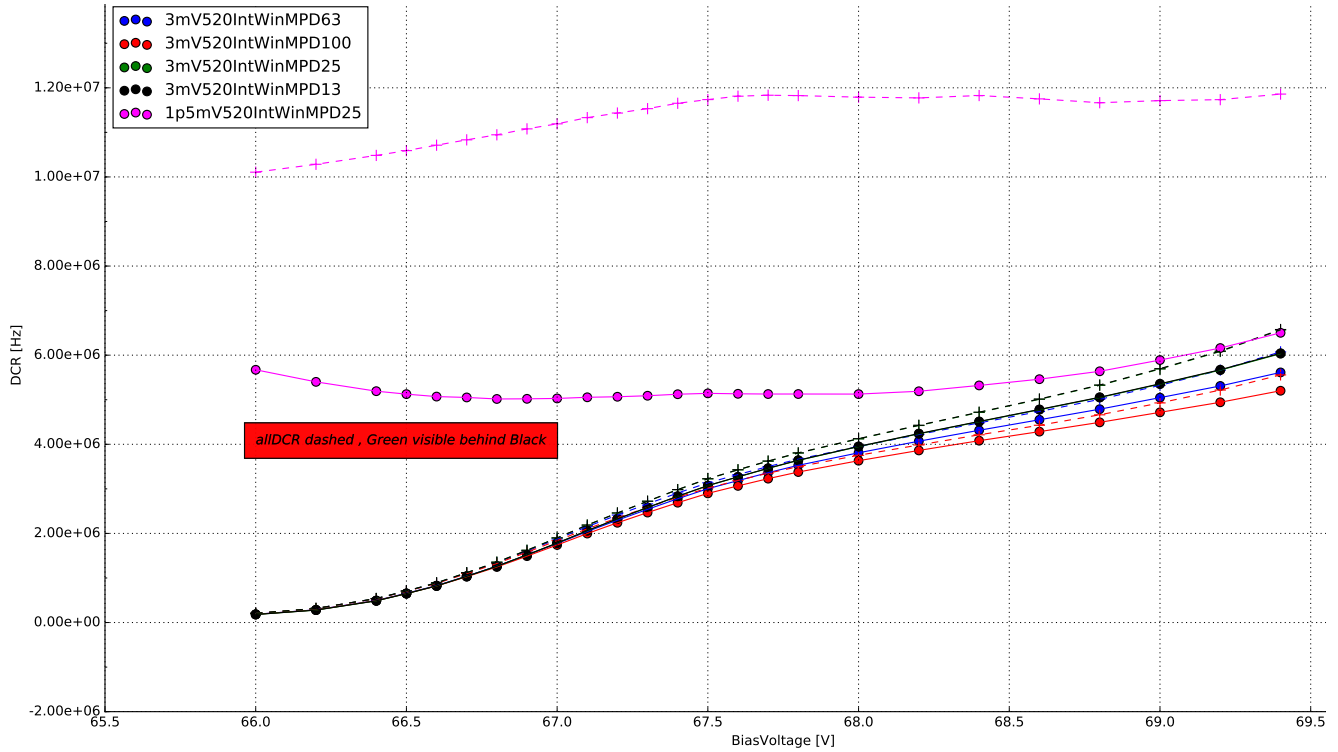


Figure 29: The difference between 4 minimum peak distance windows, in time-bins, during the peak detection. The dashed lines are the Dark Count Rates considering all recorded events, forming an upper limit. In pink, the effect of a lowered peak detection threshold is shown.

701 vices Figure (28)(green). Going lower than the pulse FWHM showed no improvement Figure
 702 (28)(black).

703 5.5.2 The influence of the integration window

704 Figure (28) also shows the influence of the size and shape of the integration window on the Dark
 705 Count Rate. The influence of the chosen integration window is most visible in their respective
 706 pulse area spectra. Choosing a narrow, symmetrical integration window of 5ns left and right of
 707 the peak maxima, the noise peak, or zero-peak, is much more prominent compared to the pulse
 708 area spectrum of a symmetrical 10 ns window. This leads to errors in the multi-gaus fitting
 709 step, or the fitting will fail altogether. An asymmetrical integration window of 5ns left, 20ns
 710 right, to capture the influence of the pulse-tail proved, at first, to be the best solution as their
 711 was no visible zero-peak present. The low amplitude pulses are averaged out by the extended
 712 integration window to the right of the pulse-maximum. The downside of the asymmetrical
 713 window is the shifting of the pulsle area spectrum and the fact, that the N p.e. peaks get
 714 blurred. The next step was widening the window on both sides. This proved the best solution,
 715 since there is no zero-peak visible and the N p.e. peaks are gaussian shaped. Please see the
 716 Appendix for the respective plots of pulse area spectra of the different windows ??.

⁷¹⁸ 5.5.3 The influence of the peak detection threshold

⁷²⁰ Choosing an adequate peak-finding threshold is a crucial step. Lowering of the threshold to
⁷²¹ ~ 0.5 p.e. will cause the peak finding algorithm to misinterpret a lot of noise peaks as actual
⁷²² dark incidents. This, of course, leads to errors in the gain extraction and even if a gain regression
⁷²³ line can be extracted, the resulting Dark Count Rates and Optical Cross Talk will be incorrect.
⁷²⁴ Figure (29), shows the effect a low peak finding threshold has on the Dark Count Rate.

725 6 Results

727 6.1 SiPM devices for CTA

Manufacturer	pixel size	cell size	coating	connection	specifics	pre-Amp
HPK S12642-1616PA-50 *CHEC-S SiPM	3mm^2	$50\mu\text{m}$	SR	TSV	no trenches	CHEC-S buffer
HPK LCT5 S13360-6050CS	6mm^2	$50\mu\text{m}$	SR	wire-bonds	trenches	MS 13V
HPK LCT5 6.975MM-SIL Single	6.915mm^2	$75\mu\text{m}$	SR	wire-bonds	trenches	MS 8V
HPK 6050HWB-LVR-LCT	6mm^2	$50\mu\text{m}$	SR	TSV	trenches	MS 13V
SensL FJ60035	6mm^2	$35\mu\text{m}$	glass	TSV	no trenches	MS 15V

Figure 30: List of SiPM devices which results are presented in this paper. *(SR: silicon resin , MS: MiniCircuits , TSV: through silicon via)

729 Silicon Photomultiplier devices for CTA are researched by many different groups, validating
730 different characteristics. Besides the current SiPM for CHEC-S, newly developed prototypes of-
731 fer a diverse range of pixel- and cellsizes. The majority of the devices are tested in Japan, at
732 the University of Nagoya, conducting in depth analysis of the characteristics over a wide over-
733 voltage range at one static temperature, mainly focusing on PDE and OCT, and their correlation.
734 This correlation of OCT and PDE for all devices determines the candidate for CHEC-S, by com-
735 paring the highest PDE at the lowest possible OCT for each device. At MPIK, chosen candidate
736 devices are examined regarding their temperature dependence and as to assist in the final deci-
737 sion by confirming results with a different analysis technique.

738 The chosen devices include the current CHEC-S device HPK S12642-1616PA-50, from Hamam-
739 matsu Photonics K.K., to be implemented in the first prototype camera. It is a previous gener-
740 ation SiPM, which was decided for use in 2014.(, due to the limited availability in high PDE
741 devices at that time.) The manufacturer supplies a 16*16 channel premounted tile of 3mm^2
742 pixels with a cell-size of $50\mu\text{m}$. To emulate the usage in a TARGET module, 4 3mm^2 pixels are
743 electrically connected to form a 6mm^2 superpixel. The tile is typically coated with epoxy resin,
744 but due to specific requirements regarding the uniformity of the coating, it was replaced with
745 a very thin layer of silicon resin equivalent to later prototypes. The CHEC-S devices electroni-
746 cal connection is realised via the new through-silicon-via (TSV) concept of running a connecting
747 solder through the silicon bulk, instead of wiring on the outside, greatly increasing the fill-factor,

748 but also including some disadvantageous sideeffects later shown.

749 Additional tested devices include the LCT5 generation from Hamamatsu Photonics K.K., so
750 called due to their low cross talk properties, namely the commercial available S13360-5050CS.
751 This device is the first to include physical trenches between the cells, effectively dividing the
752 cells optically and thus reducing prompt cross-talk probability.

753 The LCT5 generation also made two prototype devices available for testing at MPIK, the first,
754 HPK LCT5 SN CATANIA, is a larger iteration with a cellsize of $75\mu\text{m}$ and a pixelsize of 6.915mm^2 .
755 Being from the LCT5 generation it also includes optical trenches. The second device available
756 is a LCT5 prototype designated 6050HWB-LVR-LCT , LVR meaning low-voltage-range, with the
757 same physical dimensions and properties as the S13360 device but incorporating TSV technology
758 and possibly other unknown deviations.

759 The final device is a commercially available test-array designated FJ60035 from SensL, pre-
760 mounted on a test-array by the manufacturer. It has the same pixel-size, but a much smaller
761 cell-size $35\mu\text{m}$ than the previous mentioned devices and a different coating (glass).

762

763 The tests conducted in Nagoya contain many different iterations of the LCT5 generation with
764 variing pixel- and cell-sizes.

765 For a full overview of the considered Silicon Photomultipliers, please refer to the appendix under
766 (??).

767

6.2 Hamamatsu S12642-1616PA-50 50 μ m 3mm

768
769 The Silicon Photomultiplier by Hamamatsu Photonics designated
770 S12642-1616PA-50 is a 3 mm by 3 mm device. The array uses
771 the through-silicon-via technology, meaning there are no wire-
772 bonds present, the electrical connection is realised through the
773 silicon-body. The pixels are coated with a thin film of silicon
774 resin, after the previously used epoxy resin proved not uniform
775 enough. One array consists of 256 pixels, 4 of which are elec-
776 trically tied together to form a 6mm by 6mm superpixel respec-
777 tively. This practice is necessary for the pre-production camera
778 CHEC-S, because the focal plane is mechanically designed to house 64 6mm² pixels, connected
779 to the TARGET modules. Furthermore this is expected to have an influence on the results due
780 to electrical crosstalk, but this is only of minor concern due to the following.

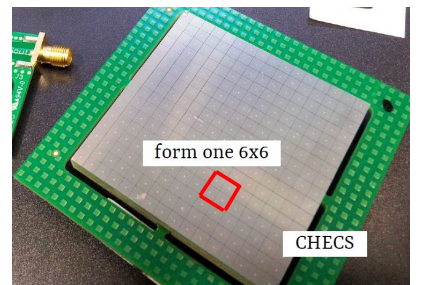


Figure 31: CHEC-S tile

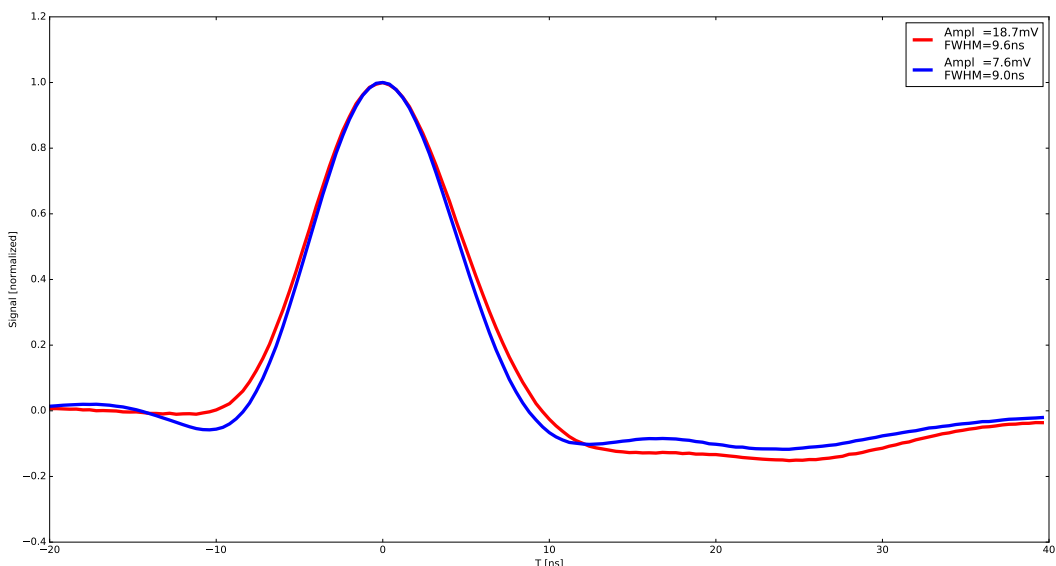


Figure 32: The average pulse shape of the 1photoelectron in blue and the 2photoelectron pulse in red of HPK S12642 at 25° C and 67.8V, which is around the proposed operating point. Both pulses are averaged over »1000 events and normalized to illustrate possible differences in pulseshape resulting from the utilized shaping electronics. Both pulses have a FWHM of around 10ns and are nearly free of ringing. The resulting average amplitude of the 1p.e. pulse is later used to calculate the Gain in [mV/p.e.] instead of [V*IntWin] by cross-referencing the 1p.e. amplitude at multiple bias-voltages.

781 My measurements of the CHEC-S tile concentrate on the array as an as-is device. This means
782 all results, influenced by external factors outside the actual Silicon Photomultipliers physics,
783 are valid on the assumption, that the way I was conducting the measurements is the way the

784 Photomultiplier will later be incorporated into the camera. On that ground, deviations of my
 785 results from the results of other groups and the manufacturer itself are expected. To clarify this
 786 further, for example, it is expected that the tests done at Hamamatsu Photonics where conducted
 787 on a single 3mm^2 pixel, not an array of 256 pixels, where 4 are tied together. Also divergence
 788 of shaping and amplification electronics between the groups will result in some differences.
 789 For this test, the CHEC-S tile is connected to the CHEC-S buffer, supplied with $\pm 4\text{V}$, where the
 790 signal is amplified. This signal in turn is then shaped via the CHEC-S shaper, developed by the
 791 University of Leicester. This is done in order to lower the unshaped pulse from a FWHM in
 792 the 100s ns to 10ns. This whole amplification and shaping chain is simulating later usage in
 793 the TARGET modules. I conducted the measurements multiple times on different pixels of the
 794 CHEC-S tile (appendix676869).

795 6.2.1 Gain 796

797 As described in section 3.2, the average pulse shape fig(32) is used to convert the relative gain
 798 from the analysis procedure to an absolute gain in sensible units. This is necessary, because
 799 the analysis aims to use pulse-area rather than -height, which results in this relative gain being
 800 in units of $V * \text{timebins}$, instead of plain V. In Figure (??) (left) the relative gain is shown, the
 801 right side shows the gain after conversion. A lower gain with increasing temperature is expected
 802 and described in detail in the chapter 3.2. In short, increased lattice movement due to higher
 803 temperature hinders photoelectron transport. The effects visible at extreme bias-voltages at both
 804 ends are partially analysis related. The gain of a SiPM is expected to be linear over bias-voltage
 805 at a constant temperature.

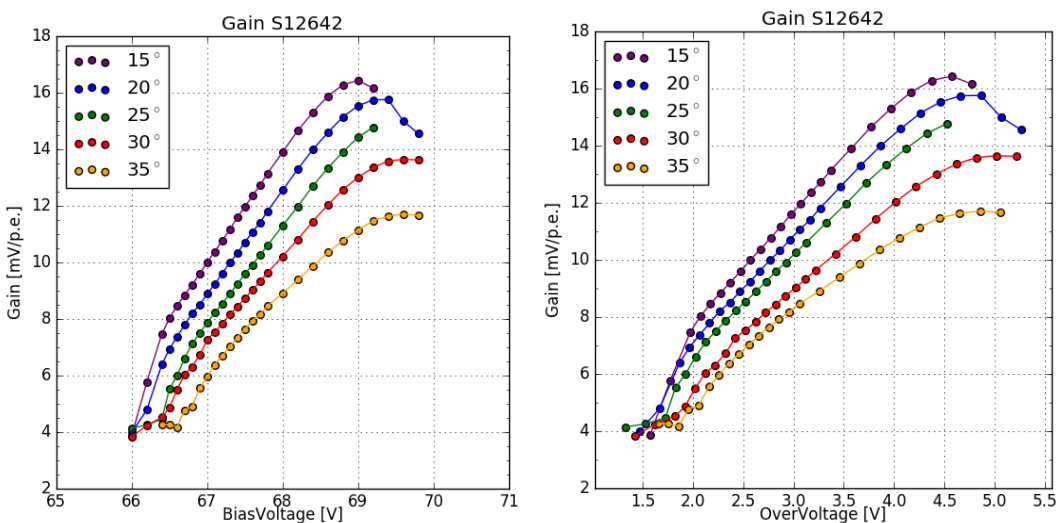


Figure 33: Gain of the HPK S12642 pixel, plotted against over-, bias-voltage and temperature.

806 In the lower regime at $V_b = 66.5\text{V}$ my analysis method struggles to pick up pulses, because of
 807 the very low gain compared to the noise. Depending on the chosen peak-finding threshold, the
 808 analysis is suspected to interpret noise peaks as 1p.e. peaks at an increasing rate, the lower the

809 overvoltage is. This is visible in the sudden break in linearity at 30° C and 35° C , where the gain
 810 is almost in a plateau, due to this effect. The roll-over of the gain at the highest bias-voltages is
 811 in part a result of a voltage drop across the bias resistor occurring, because of high current flow
 812 through the SiPM. At higher temperatures, and therefore higher dark rates, the effect occurs
 813 at lower over-voltages. A second influence is caused again, by the noise at Vov 5V, which is
 814 very high compared to the proposed point of operation at Vov 3V. The same threshold is again
 815 counting the now increased noise peaks as 1p.e. peaks, but due to the abundance of 1p.e. pulses
 816 this just results in an apparent lowering of the gain.

817 6.2.2 Dark Count Rate

818 The Dark Count Rate is expected to increase with temperature, which is the case for S12642
 819 showb in Figure (34). I also expect it to follow a nearly linear progression, a sudden turn-up
 820 or turn-down of the Dark Count Rate would be analysis related. The turn-up at a certain point
 821 is visible in Figure (34), particulary for 15° C (purple) and 20° C (blue) respectively. At 15° C
 822 and an Overvoltage of 4V, the Dark Count Rate starts to deviate from the previously linear be-
 823 haviour. It starts to rise more rapid than before, which I can attribute to the fact, that the Optical
 824 Cross Talk at that point is very high; higher than 50% fig(35) (left). I suspect that I do not reach
 825 this critical point for the higher temperatures of 25° C (green) and 30° C (red), so the effect is
 826 barely, if not at all visible. At 35° C (yellow) I suspect my analysis is not able to count every

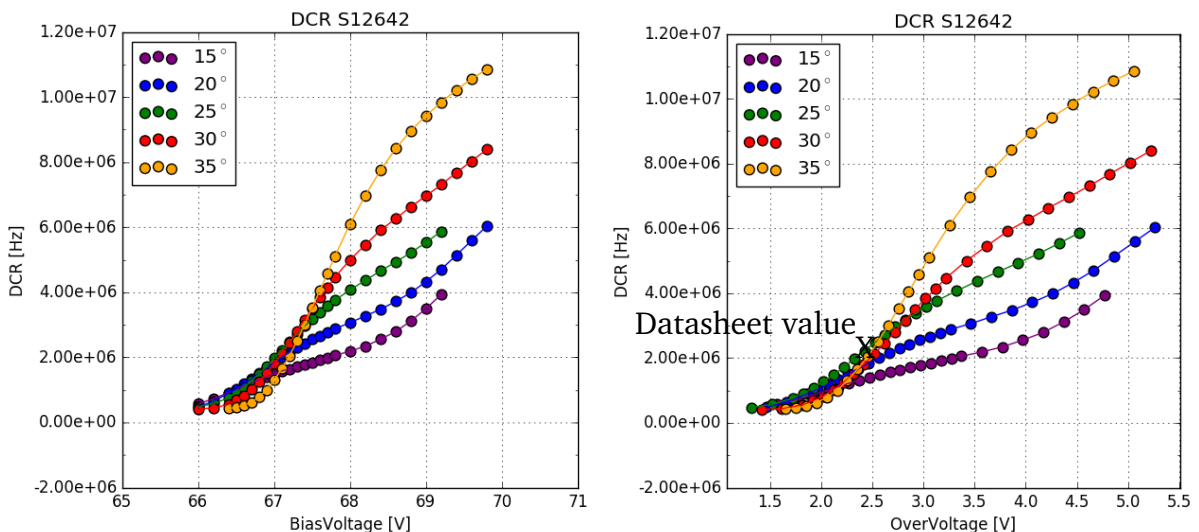


Figure 34: Dark Count Rate of the HPK S12642 pixel, plotted against over- , bias-voltage and temperature. Datasheet value at operation voltage = 2.4V and 25°C measured by current

827 pulse, due to the high rate of 9-10 MHz. A majority of the pulses overlapping each other and
 828 being counted as a 2p.e. event rather than 2 1p.e. events would reduce the Dark Count Rate sig-
 829 nificantly. At this point, heating of the Silicon Photomultipliers surface due to the high rate could
 830

831 also affect the Dark Count Rate through shifting of the temperature slightly upwards, away from
832 35° C . So that the Dark Count Rate declared at 35° C is in reality the rate at higher temperatures.

833

834 At the lower end of the bias-voltage range, I suspect, that a major part of the found 1p.e.
835 pulses are actually noise related. So the Dark Count Rate changing to a plateau is expected.
836 This is also due to the fact, that my measurements are done with a fixed bias-voltage range.
837 Due to the increase of the breakdown-voltage with rising temperature, part of the measured
838 bias-voltage range corresponding to a very low over-voltage, attributes to this effect. In order
839 to reliably measure beyond an overvoltage of 2.5V in the lower range, the noise would need to
840 be improved.

841 842 6.2.3 Optical Cross Talk

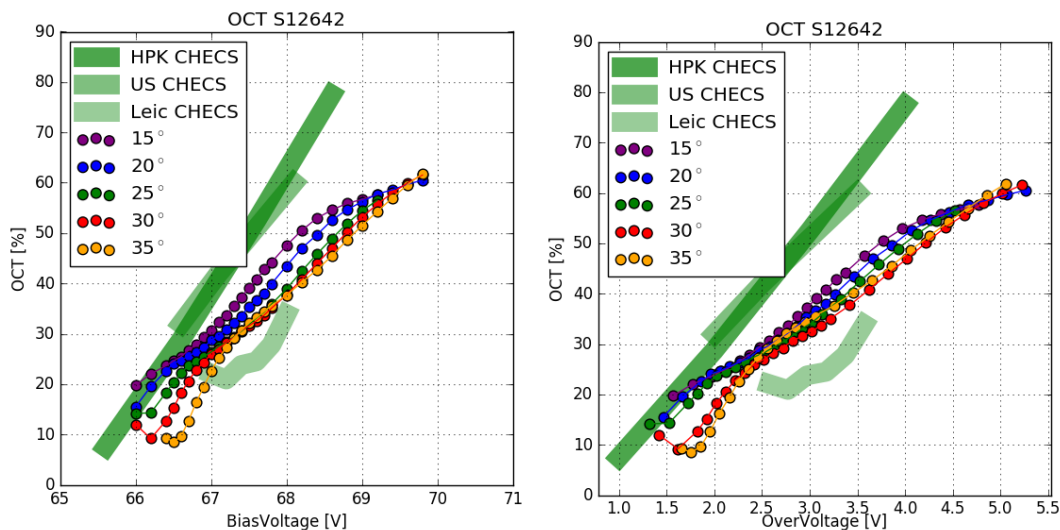


Figure 35: Dark Count Rate of the HPK S12642 pixel, plotted against over-, bias-voltage and temperature.

843 The Optical Cross Talk should be linear and independent from temperature. This is confirmed
844 for HPK S12642. Minor deviations from that are probably due to slight errors in the breakdown-
845 voltage calculation from the gain regression line. The deviation of 30° C and 35° C below
846 an over-voltage of 2V stems from the way the gain regression line is used to calculate both
847 Dark Count Rate and Optical Cross Talk. At higher temperatures the lower voltage range is
848 dominated by noise, so using the gain regression line to calculate the Optical Cross Talk at
849 those low voltages leads to the visible effect of the first few datapoints of 30° C and 35° C.
850 The deviations between the different groups results at 25° C (green) are caused by 4 major
851 contributions. Firstly the difference in the tested device. While I take measurements on 4
852 3mm² pixels electrically tied together, the way the device will later be implemented into CHEC-
853 S, the groups in the US[17] and Hamamatsu Photonics[16] are likely to run tests on 1 3mm²
854 pixel only. Secondly I suspect a slight difference in amplification and shaping electronics. The

855 measurements I conducted as well as the measurements of Leicester are done with the same
856 shaper and buffer configuration. The difference here is, thirdly, my measurements are done
857 with dark counts only, while measurements from other groups are conducted with a pulsed light
858 source and reading out timed windows. This causes the results from Leicester to be difficult to
859 compare against, their surface temperature of the SiPM is likely much higher than 25° C, and
860 thus, a misinterpreted breakdown-voltage at 25° C causes a shift of the Optical Cross Talk to
861 the right. Lastly the difference in actual data taking and analysis procedure must be mentioned,
862 also this is only of minor concern, as we will see with other measured devices.

863 6.3 Hamamatsu LCT5 50 μ m 6mm

865 The Silicon Photomultiplier designated HPK S13360
866 6050CS fig(36) is an LCT5, meaning Low Cross Talk
867 5th iteration device from Hamamatsu Photonics. It is
868 one of the most promising candidates for later usage in
869 CHEC-S. It has a pixelsize of 6mm² consisting of 14400
870 cells with a cellsize of 50 μ m. The present device and
871 its similar iterations are the first to incorporate trenches
872 bordering each cell, effectively insulating the cells and
873 reducing the prompt Optical Cross Talk very effectively.
874 Tests are done with a single pixel only, in contrast to
875 measurements done on S12642. It is mounted on a
876 ceramic chip and coated with a silicon resin that is UV-
877 transparent. Wire bonds supply the electrical contact. A similar, but not tested, device from
878 the same generation uses through-silicon-via (TSV) technology, realising electrical connection
879 through the silicon bulk, allowing a tighter fit of the cells, with minimal dead-space.

LCT5 6mm

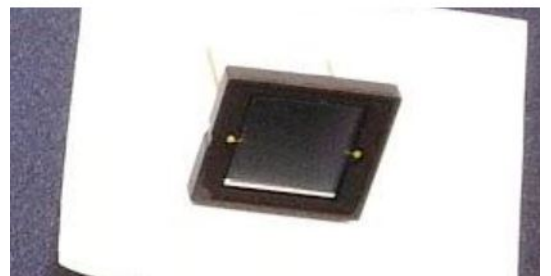


Figure 36: HPK S13360 6050CS pixel

A similar, but not tested, device from the same generation uses through-silicon-via (TSV) technology, realising electrical connection through the silicon bulk, allowing a tighter fit of the cells, with minimal dead-space.

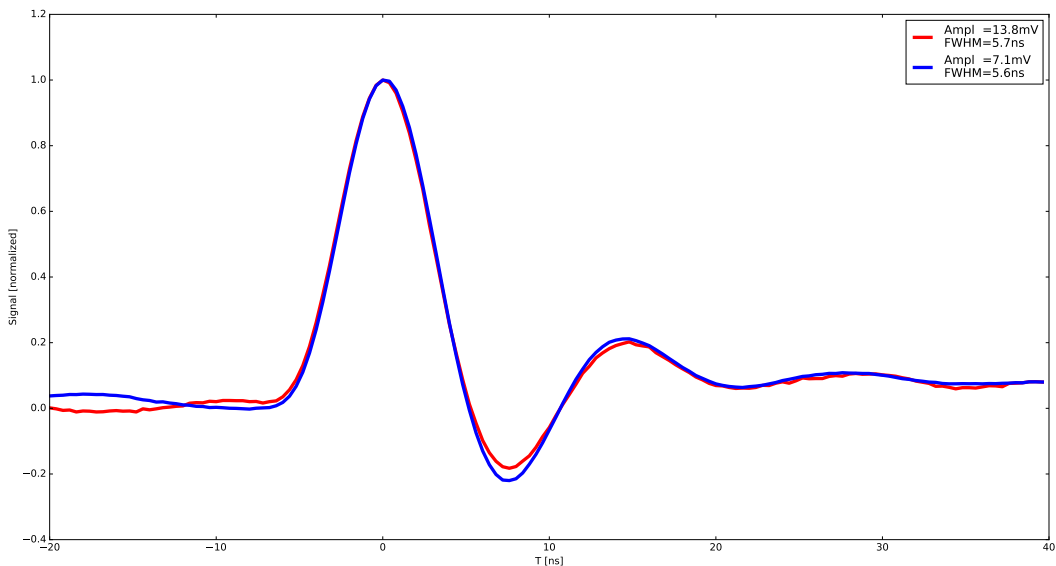


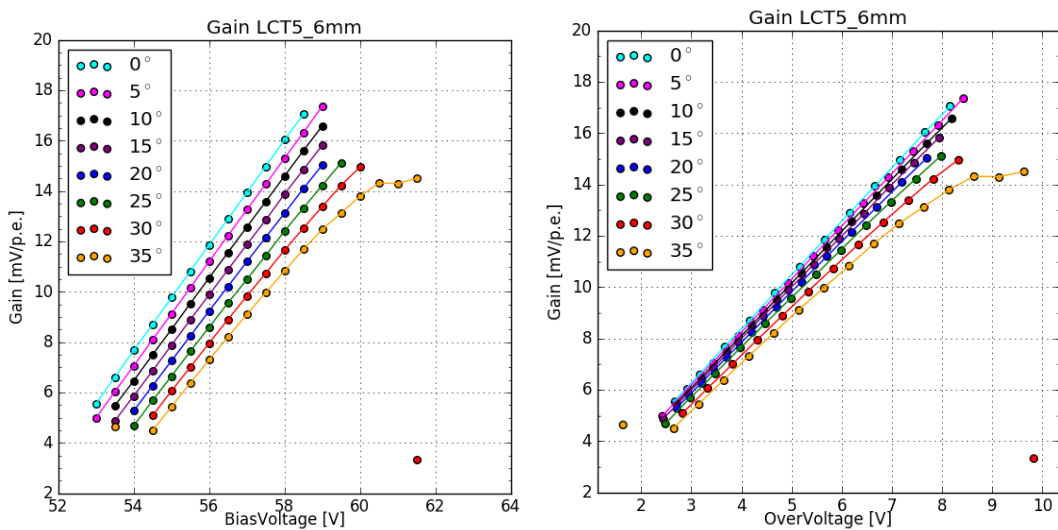
Figure 37: The average pulse shape of the 1photoelectron in blue and the 2photoelectron pulse in red of HPK S13360 6050CS at 25° C and at point of operation. Both pulses have a FWHM of around 5ns and ring for approximately 20ns with an undershoot of 20%.

880 The layout of the single pixle test device made external amplification necessary. I used a
881 MiniCircuits PreAMP, which was supplied with 13V during this test. Shaping of the pulse is
882 conducted by a CHEC-S shaper, modified to fit the new unshaped pulse. The pulse shape fig(37)
883 makes the pulses appear much harder to analyze, due to the possibility of events occurring during

884 the ringing window. This assumption proved untrue, due to the devices low Dark Count Rate
885 and Optical Cross Talk, so the multi incident probability is also low.

886 6.3.1 Gain

888 The gain of the LCT5 50 μ m 6mm device is clearly linear with some minor outliers at 30°C.
889 The same effect as with S12642 is visible at 35°C, again counting noise peaks as 1p.e. peaks,
890 resulting in an apparent lowering of the gain and the slope changing over into a plateau. In
891 Figure(38)(left) the gain is shown, plotted against over-voltage. It is still dependant on tem-
892 perature, but due to reliable breakdown-voltage calculation, the spread is much smaller than,
893 if plotted against bias-voltage. The same conversion is done to transform relative gain into an
894 absolute gain with sensible units. When parametrized with over-voltage, the gain is essentially
temperature independent.



895 **Figure 38:** Gain of the HPK S13360 pixel, plotted against over-, bias-voltage and temperature.

896

897 6.3.2 Dark Count Rate

898 The Dark Count Rate of two similar HPK S13360 devices is shown in Figure(39). The bars
899 show the difference between the two devices, the results of one device is used as a reference,
900 while the deviation is illustrated with the filled bar. The Dark Count Rate of HPK S13360
901 follows the expected behaviour, mostly linear in the significant range and rising with increasing
902 temperature. Below an over-voltage of 2.5V the analysis struggles, compared to noise, the gain
903 is suspected to be to low for the analysis to pick up pulses. Thus the regression line calculation
904 is unreliable in this range. The turnup at high over-voltages is most prominent at 0°C(teal)
905 after an over-voltage of 9V. This is also the point where the Optical Cross Talk rises very rapidly.
906 The large range of the DCR at an over-voltage of 3V makes it difficult to compare against, the
907 manufacturer determines the DCR by measuring the current.

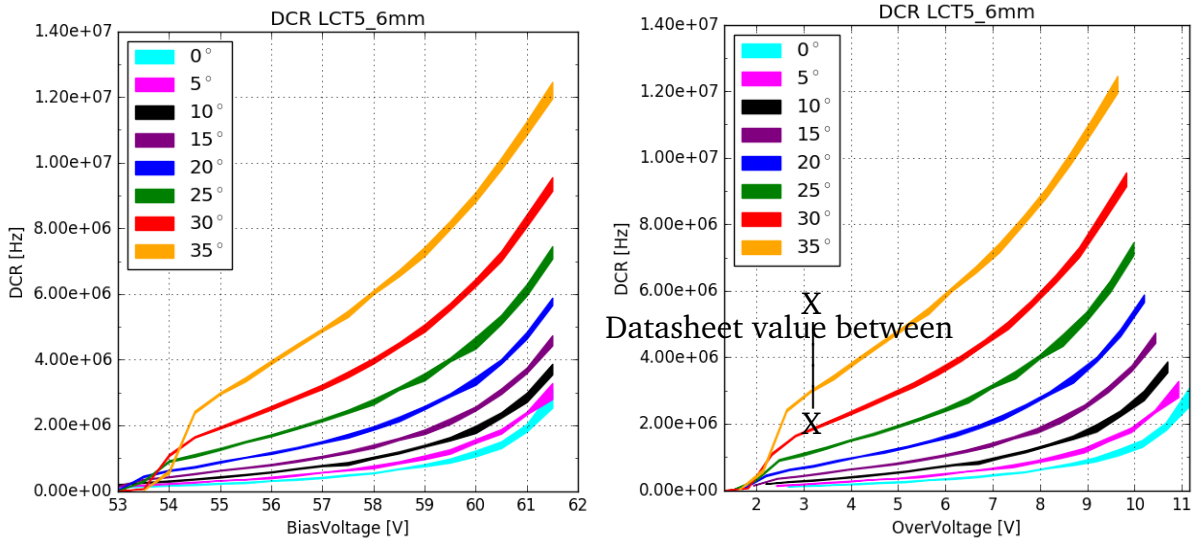


Figure 39: Dark Count Rate of the HPK S13360 pixel, plotted against over-, bias-voltage and temperature. The Datasheet value at 25°C of the DCR at $V_{OV} = 3V$ covers a very large range to exactly compare against, and is measured by current

908 6.3.3 Optical Cross Talk 909

910 Compared to measurements on HPK S13360 done at the Nagoya University, Japan fig(40)
911 (faded green bar), I see a very strong correlation of the Optical Cross Talk in the over-voltage
912 range between 2.5V and 9V. The Optical Cross Talk in this range is linear and independent from
913 temperature, with minor deviations attributed to the breakdown-voltage calculation from the
914 regression line, causing the horizontal shift. In contrast to my technique, using only dark counts,
915 the measurements at Nagoya University followed a pulsed light source approach, reading out
916 a time-window after the laser incident. This could have consequences, since Optical Cross talk
917 with a large delay time could be missed. Deviations below an over-voltage of 2.5V are expected,
918 they are very likely caused by the regression line calculation being unreliable in this range due
919 to the analysis method struggling to pick up pulses using dark counts. Above an over-voltage
920 of 9V, which is also the point of the turnup of the Dark Count Rate, the Optical Cross Talk is
921 no longer linear and the deviation from the results of Nagoya University increase very rapidly.
922 I suspect the rapid increase in both Dark Count Rate and Optical Cross Talk to be caused by
923 the over-voltage reaching ranges, where interpretation of noise as a 1p.e. pulse becomes more
924 likely. This, joint together with the usage of the MiniCircuits amplifier supplied with 13V, makes
925 false interpretation of noise as pulses even more likely. I suspect these two reasons in conjunc-
926 tion are responsible for both, the sudden rise of the Dark Count Rate as well as the deviation of
927 the Optical Cross Talk from linearity and the results of Nagoya University, above over-voltages
928 around 9V. In summary, the correlation between the two measurements, conducted by two dif-
929 ferent methods of data acquisition and analysis, is evident.

930

931

932 The S13360 series is the first to incorporate physical barriers, called trenches, effectively insu-
 933 lating the cells from each other. This drastically reduces the prompt cross-talk, while increasing
 934 the percentage the delayed cross-talk contributes to the overall cross-talk shown. This could
 935 also be the reason for the upturn compared to data from the University of Nagoya, at higher
 936 over-voltages the contribution from delayed cross-talk is higher. With the trenches effectively
 937 reducing the prompt cross-talk and the difference in analysis, the effect could be partially ex-
 938 planed by increased contribution of the delayed cross-talk. More on this subject in chapter
 939 7.

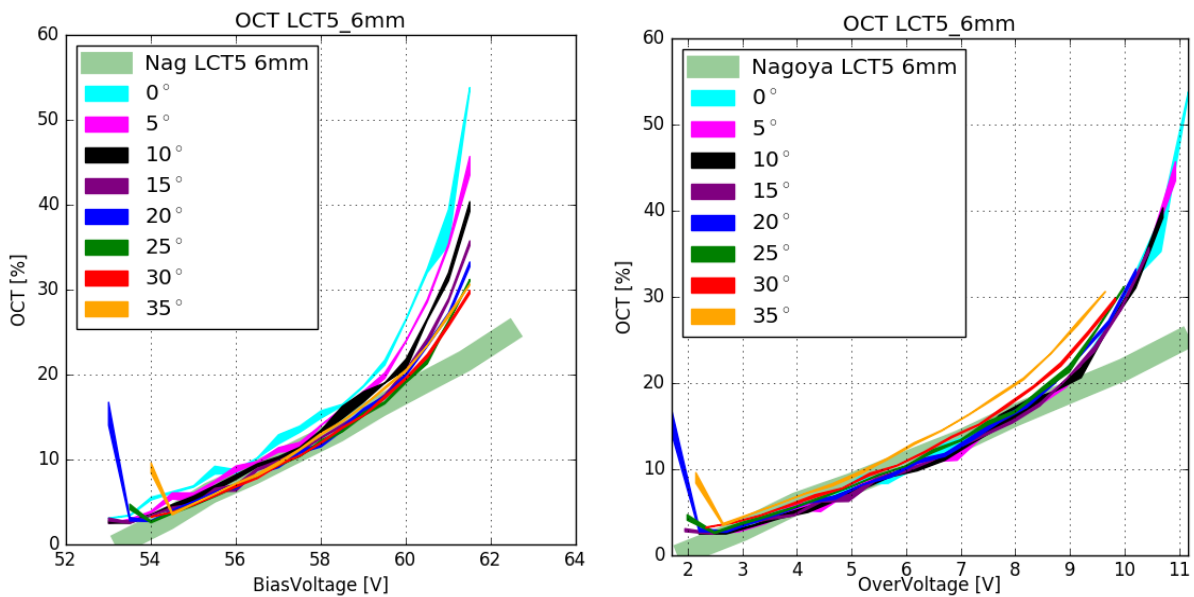


Figure 40: Optical Cross Talk of the HPK S13360 pixel, plotted against over-, bias-voltage and temperature.

940
941

6.4 Hamamatsu LCT5 75 μ m 7mm

942 The device named 6.975MM-SIL Single is a larger LCT5
943 prototype Silicon Photomultiplier of the same design as
944 S13360-6050CS fig(41). With an increase in cellsize to
945 75 μ m, the device gains a higher fill-factor than 50 μ m
946 devices. The pixel-area is also expanded to 6.915mm²,
947 which will result in a higher fill-factor (less deadspace),
948 so presumably a higher PDE but also a higher OCT.
949 Since it is a prototype device, there is limited data
950 from datasheets. The ID number suggests, that it is
951 also a wire-bond device with a UV-transparent silicon-
952 resin coating. It is also a single pixel test device, so
953 external amplification is necessary with the MiniCir-
954 cuits PreAMP supplied with 8V during this test. The signal is also shaped by a differently
955 modified CHEC-S shaper, which results in a pulse shape similar to S12642, but with a much
956 lower amplitude fig(42).

LCT5 7mm



Figure 41: HPK LCT5 7mm pixel

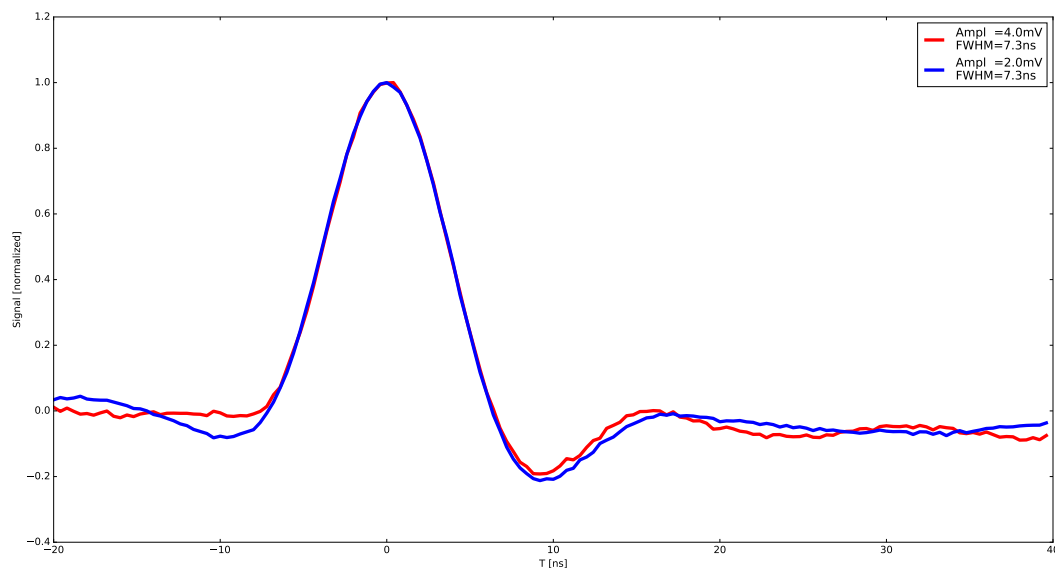


Figure 42: The average pulse shape of the 1 photoelectron in blue and the 2 photoelectron pulse in red of HPK LCT5 7mm at 25° C and at point of operation. Both pulses have a FWHM of around 7ns and an undershoot of 20%, with no ringing.

6.4.1 Gain

Figure(43) shows the gain of the LCT5 7mm device. Two sets of measurements are done for 25°C to extend the measured range. The first set of measurements covers the lower over-voltage range, where the low gain makes external amplification necessary with a MiniCircuits PreAMP supplied with 8V. I chose the lowest possible amplification of the PreAMP, so that reaching the point of saturation of the oscilloscope input is as late as possible as the over-voltage rises. Saturation of the oscilloscope occurs due to the possibility of generating very large p.e. (>10 p.e.) events at the higher over-voltages, which are saturating the input. Joint together, the LCT5 7mm device and the MiniCircuits PreAMP at 8V reach this point at an over-voltage of ~ 6 V. In Figure(43) the results from

the lower range measurement are displayed as the lower-range green line extending between an over-voltage of 1.6V to 5.4V. The configuration for the second test removes the PreAMP from the setup, which makes the lower over-voltage range unaccesible, but extends the range to higher over-voltages. This configuration reaches the point of saturation at an over-voltage of ~ 8 V. The higher range measurement results are displayed as the second green line (25°C) extending from 3.4V to 7.2V over-voltage in Figure(43). There is a clearly visible overlap of the two measurements between ~ 3.4 V and ~ 5.4 V . It also seems, that the gain dependency on temperature is reversed. While for all other devices, the gain lowers with rising temperatures, the LCT5 7mm device seems to show inversed behaviour. This inverse behaviour is caused by the calculation of the breakdown-voltage from the gain-regression line, with this and the bias-voltage, the over-voltage is calculated, causing a horizontal shift. Plotting the gain versus bias-voltage, however, shows the expected behaviour.

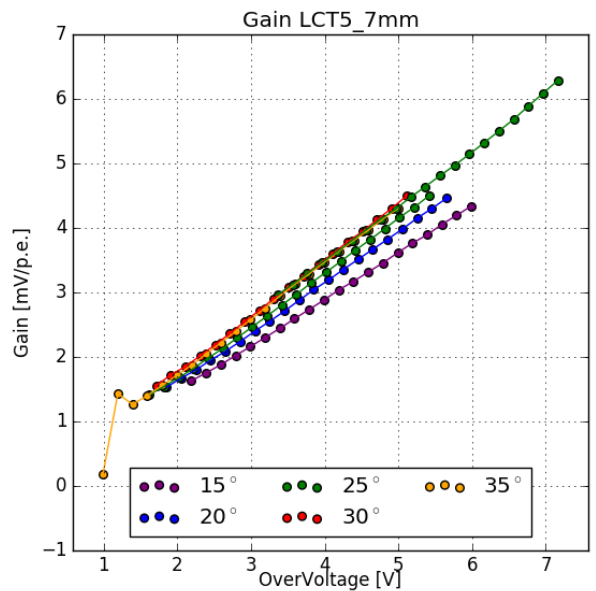


Figure 43: Gain of the HPK LCT5 7mm pixel

987 6.4.2 Dark Count Rate

989 The behaviour of the Dark Count Rate of the HPK LCT5
990 7mm device is shown in Figure(44) and is as expected,
991 in contrast to the behaviour of the gain of LCT5 7mm,
992 as discussed in section 6.4.1. It follows a linear pro-
993 gression in the relevant range and increases with rising
994 temperature. I suspect the over-voltage range above
995 $\sim 2.5V$ to be relevant. The extended range measure-
996 ment at $25^{\circ}C$ confirms this behaviour. LCT5 7mm
997 shows a linear Dark Count Rate over an over-voltage
998 range of 4V. The faded green bar in Figure(44) shows
999 results from measurements undertaken by the Depart-
1000 ment of Physics and Astronomy at the University of
1001 Catania. Those measurements were conducted on the
1002 exact same device, which is an important point, but
1003 with a different method of data acquisition and data analysis. Analysis techniques are discussed
1004 in chapter 7. The correlation between the two experiments is evident, although there is differ-
1005 ences in the acquisition and analysis process. This is further proof for the relevancy of the
1006 analysis technique employed in this paper.

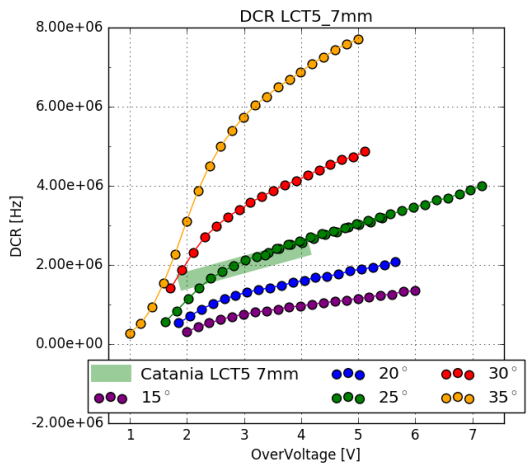


Figure 44: Dark Count Rate of the HPK LCT5 7mm pixel

1007 6.4.3 Optical Cross Talk

1009 The Optical Cross Talk is expected to be linear and in-
1010 dependent from temperature. This is the case in the, in
1011 section 6.4.2 established, relevant over-voltage range
1012 of above $\sim 2.5V$. Minor deviations are attributed to the
1013 calculation of the breakdown-voltage from the gain-
1014 regression line. The over-voltage is calculated from
1015 the former and the supplied bias-voltage, which in turn
1016 causes a slight horizontal shift. With that, comparing
1017 my results to the measurements from the University of
1018 Catania shows a strong correlation. Keeping in mind,
1019 that the process of data acquisition and analysis is dif-
1020 ferent for both measurements further proofs the analy-
1021 sis technique valid.

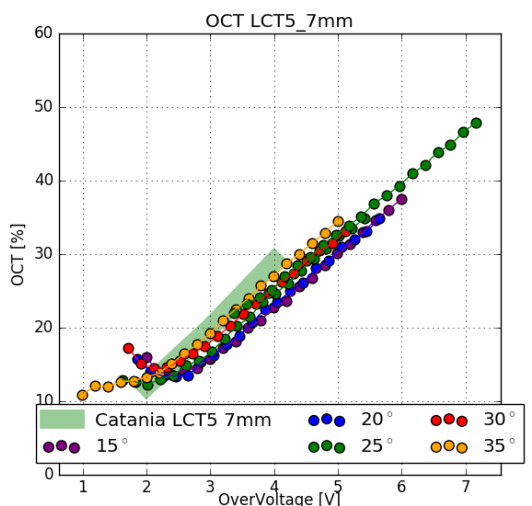


Figure 45: Dark Count Rate of the HPK LCT5 7mm pixel

1022 6.5 Hamamatsu LVR 50 μ m 6mm

1024 The Silicon Photomultiplier by Hamamatsu Photonics
1025 with the designation 6050HWB-LVR-LCT is a special
1026 prototype of the LCT5 design. LVR is an abbreviation
1027 of Low Voltage Range, meaning the device is meant
1028 to be operated at much lower operation voltages than
1029 other LCT5 devices. It has the same physical size as an
1030 LCT5 50 μ m 6mm device (S13360 chapter ??), a pix-
1031 ellsized of 6mm pixel with a cellsize of 50 μ m. The rec-
1032 ommended point of operation however is \sim 15V below
1033 that of the S13360 device, specifically at 40.2V(LVR)
1034 instead of 54.7V (S13360). The unshaped signal is
1035 similar to other LCT5 devices, therefore using the same modified CHEC-S shaper is feasible
1036 in this case, resulting in a similar pulse shape fig(47). After that the signal is amplified with the
1037 same MiniCircuits PreAMP supplied with 8.5V.

1038

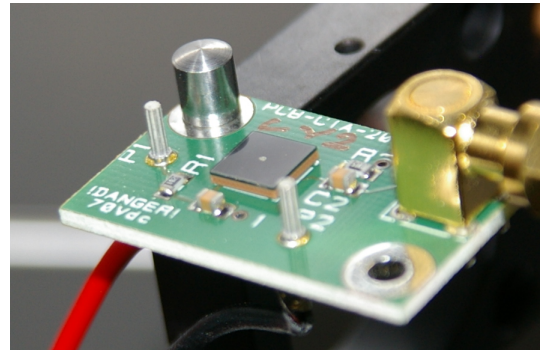


Figure 46: HPK LVR 6mm pixel

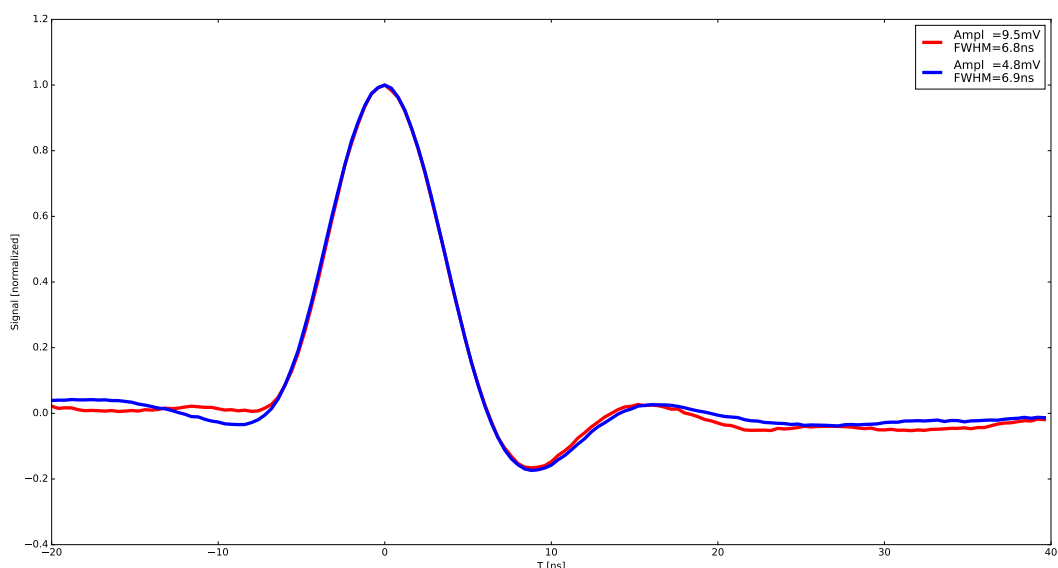


Figure 47: The average pulse shape of the 1photoelectron in blue and the 2photoelectron pulse in red of HPK LVR 6mm at 25° C and at point of operation. Both pulses have a FWHM of around 7ns and an undershoot of 20%, with no ringing.

1039 6.5.1 Gain

1041 Figure(48)(right) shows the gain of the LVR 6mm device. It is, as expected, linear over a
1042 long range and nearly independent of temperature when parametrized with over-voltage. The
1043 flattening of the slope to a plateau shape in the lower over-voltage range, is caused by the

analysis being unable to identify peaks lower than the set threshold. Only taking into account the linear region, limits the range, where the results are relevant to an over-voltage range of ~ 2.5 V. Saturation of the oscilloscope in this range is not visible, but a check with a more expanded range revealed, that the point of saturation of the oscilloscope is at an over-voltage of ~ 5 V. The apparent overlap of the gain, when plotted against over-voltage, is based on the calculation of the breakdown-voltage being very reliable due to the large linear range. Plotted versus bias-voltage fig(48)(left) the expected behaviour of the gain, lowering with increasing temperature, is visible.

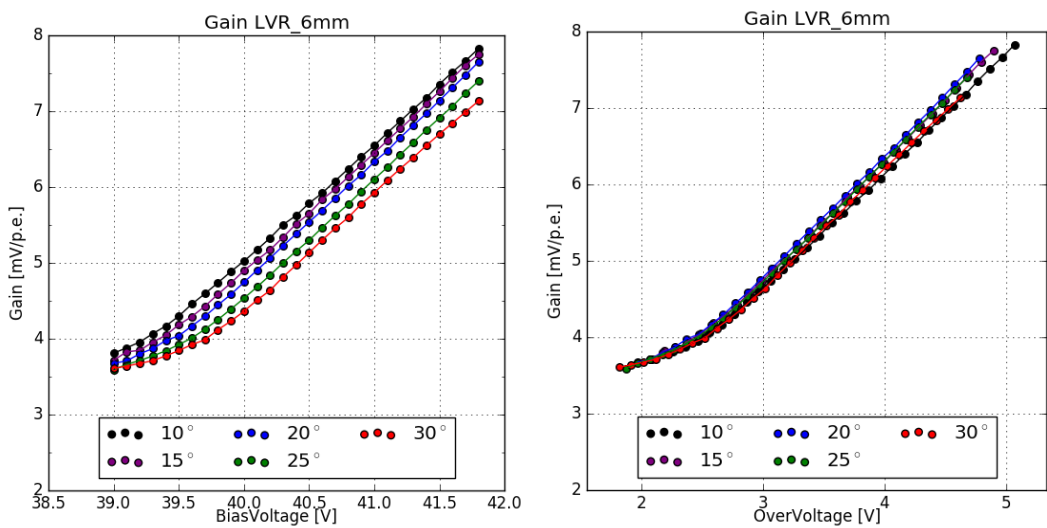


Figure 48: Gain of the HPK LVR 6mm pixel

1051

1052 6.5.2 Dark Count Rate and Optical Cross Talk 1053

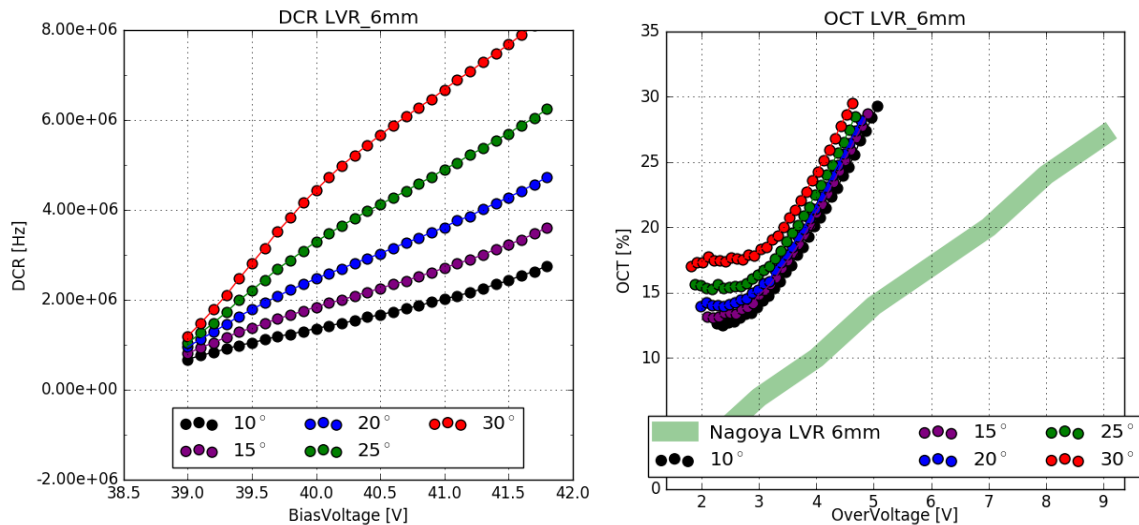


Figure 49: Dark Count Rate and Optical Cross Talk of the HPK LVR 6mm pixel

1054 The Dark Count Rate fig(49)(left), taking into account only the relevant over-voltage range
1055 of $>\sim 2.5V$ seems to correlate, while the resulting Optical Cross Talk fig(49)(right) is very high
1056 compared to results from the University of Nagoya, which also cover a much wider range.
1057 Only taking into account the previously established relevant over-voltage range of $>\sim 2.5V$, the
1058 resulting Optical Cross Talk is a factor of 2 higher. This uncertainty is a contrast to results
1059 from previous devices, where strong correlations between different groups and measurement
1060 techniques are evident. I suspect, that the device examined by me and the device present at
1061 Nagoya University are slightly different prototypes.

1062 6.6 SensL FJ60035 6mm 35 μ m

1064 The Silicon Photomultiplier by SensL with the designation FJ-60035 is also a candidate device
1065 for use in CHEC-S. It is also a 6mm device, but with a much smaller cellsize of 35 μ m, using the
1066 TSV technology, so there are no wire-bonds present. This results in 22292 cells on a single pixel
1067 with a fill-factor of 75% . It is coated with plain glass. The recommended point of operation
1068 is around 30V bias-voltage, lower even than that of the HPK IVR prototypes. The device is, by
1069 the manufacturer, pre-mounted on a printed circuit board, called a test array. This test array
1070 contains a fast output, that directly couples to the cells, and a slow output, conventionally
1071 read out via the quench resistor. For the conducted tests, I used the fast output amplified with
1072 the MiniCircuits PreAMP supplied with 12V. The SensL device was the first device measured,
1073 therefore the analysis procedure used was an older iteration compared to the procedure for the
1074 Hamamatsu devices.

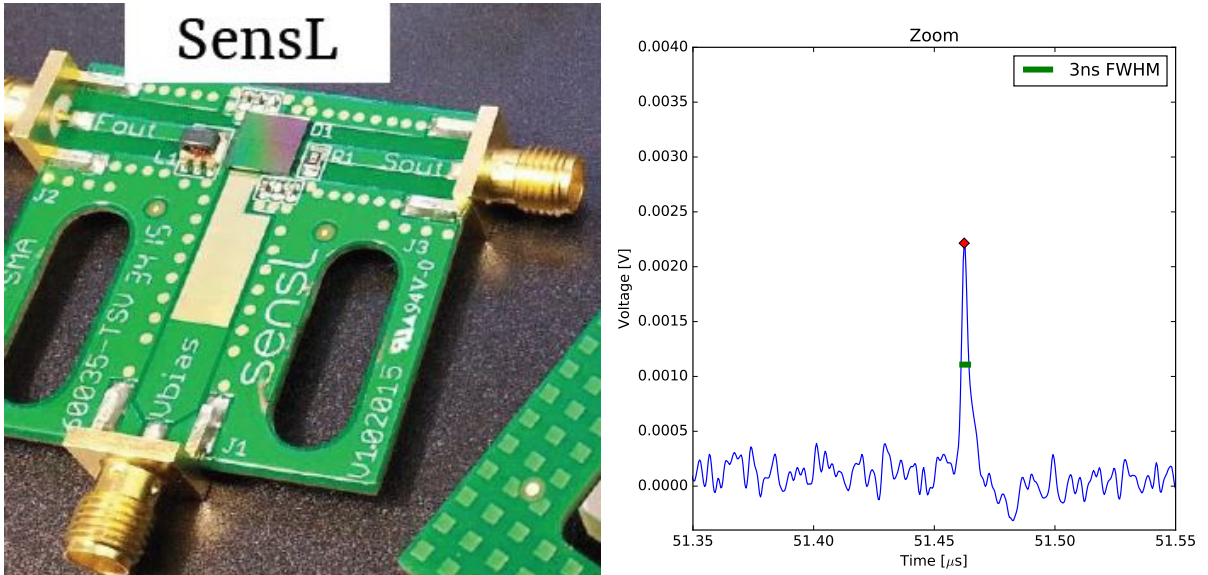


Figure 50: SensL Test Array and pulse shape at $V_{bias-voltage} = 29V$

1075 6.6.1 Gain

1077 Evaluating the SensL pulse area spectra shows the 1 p.e. position and Δ p.e. overlapping,
1078 so using the older analysis iteration introduced no error when evaluating the gain of the SensL
1079 device. It is clearly linear over a wide temperature range from -5°C to 35°C over an over-voltage
1080 ranging from 2V up to 8V. When plotted versus over-voltage the spread of the gain is even
1081 tighter signaling slight temperature independency, but still following the expected behaviour of
1082 decreasing with increasing temperature.

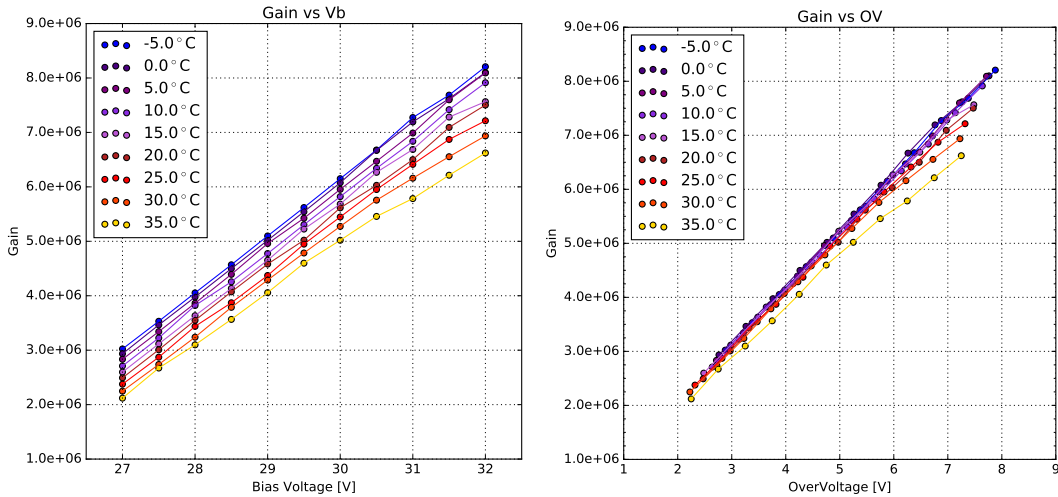


Figure 51: Gain of the SensL FJ-60035 test array

1083 6.6.2 Dark Count Rate and Optical Cross Talk

1085 The Dark Count Rate fig(52)(left) also shows the expected behaviour. At very low temperatures
 1086 the changes in rate over the over-voltage range is minimal. Increasing the temperature shows
 1087 a rapid increase in thermally induced dark counts. The Optical Cross Talk fig(52)(right) on the
 1088 other hand is independent of the device temperature, also as expected. In both cases, the values
 1089 agree with values derived from the datasheet.

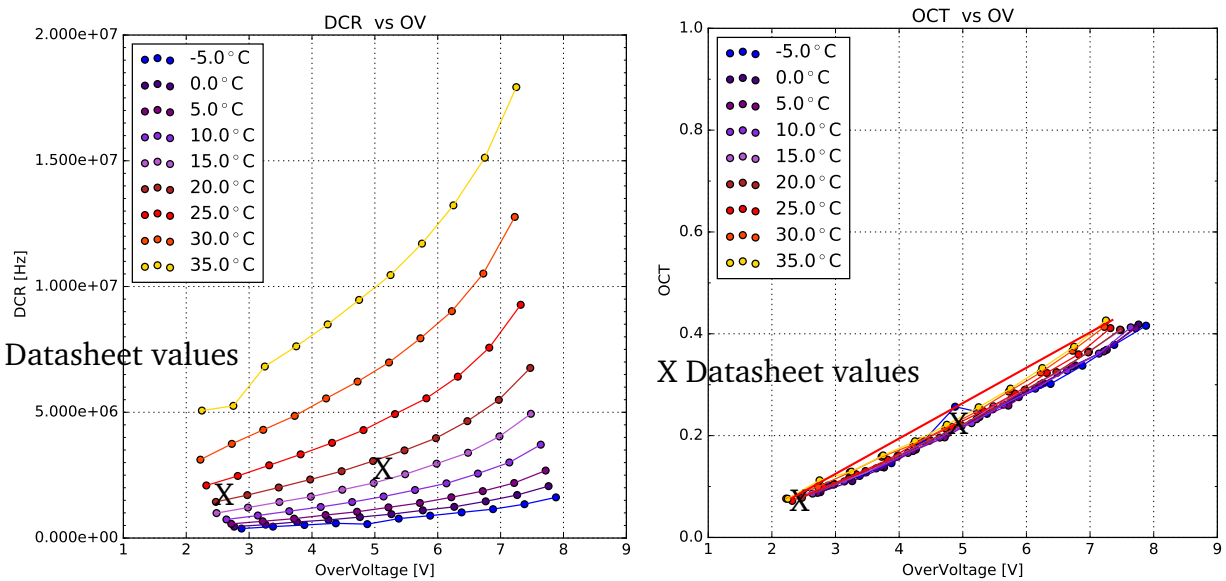


Figure 52: Dark Count Rate and Optical Cross Talk of the SensL FJ-60035 test array. Datasheet values, marked with X, measured at 21°C(~dark red). OCT results of Nagoya University marked by the red line.

1090 1091 7 Comparison

1092 A comparison of the performance of all devices is the significant step for choosing the Silicon
1093 Photomultiplier later to be used in CHEC-S. In order to do this, all measured characteristics are
1094 compared versus over-voltage. Operation of the CHEC-S camera in GCT will come down to a
1095 decision between two operational points. The first point will be marked by an Optical Cross Talk
1096 of under 15%. Every other attribute of the Silicon Photomultiplier at this over-voltage is then
1097 compared. This point will trade off precision for efficiency, a lower Optical Cross Talk makes
1098 real event detection easier, on the other hand, a lower Photon Detection Efficiency may forfeit a
1099 lot of potential data.

1100 The second point of operation is marked at the highest achievable Photon Detection Efficiency.
1101 My conducted measurements do not involve this, other groups are comissioned to determine
1102 the point of highest Photon Detection Efficiency, in other conducted measurements, that are
1103 comparable 56. This point will assure the highest detection of event photons, but will trade
1104 that for an increase in detector noise, due to the higher Dark Count Rate and more importantly
1105 Optical Cross Talk.

1106

1107 Comparing results to other groups is shown in Figure (53), using different experimental se-
1108 tups and procedures and therefore also entirely different analysis techniques. The groups, that
1109 evaluate SiPMs, the University of Leicester, the University of Nagoya and the University of Cata-
1110 nia, are all conducting fixed window readout of the SiPM after an expected light-pulse from a
1111 flasher-LED or pulsed laser.

1112

1113 The SensL device showed a very low PDE compared to the measured HPK devices fig(56).
1114 Therefore the following figures are only showing the HPK results for reasons of performance.

1115 1116 7.1 Dark Count Rate

1117 Comparing the Dark Count Rate of the measured devices and results from the other groups is
1118 shown in Figure 53. The differences in analysis procedure will only have a slight impact on the
1119 presumed Dark Count Rate, since all experiments record dark-count events over their respective
1120 acquisition time windows. On the other hand, if the readout window is sufficiently small, events
1121 originating from afterpulsing or delayed crosstalk could be missed. All groups experience the
1122 same multi-hit coincidence, meaning a light-event or dark-event coinciding with another, form-
1123 ing a (partial)multi p.e. event.

1124 Only two of the five measured devices have measurements result from other groups to compare,
1125 as it is not their focus. In the case of both, the IVR 6mm and the LCT5 7mm results can be
1126 discussed to some degree as matching. While the correlation is obvious for the LCT5 7mm de-
1127 vice Figure(53)(red), where the covered measurement range in this paper exceeds the external

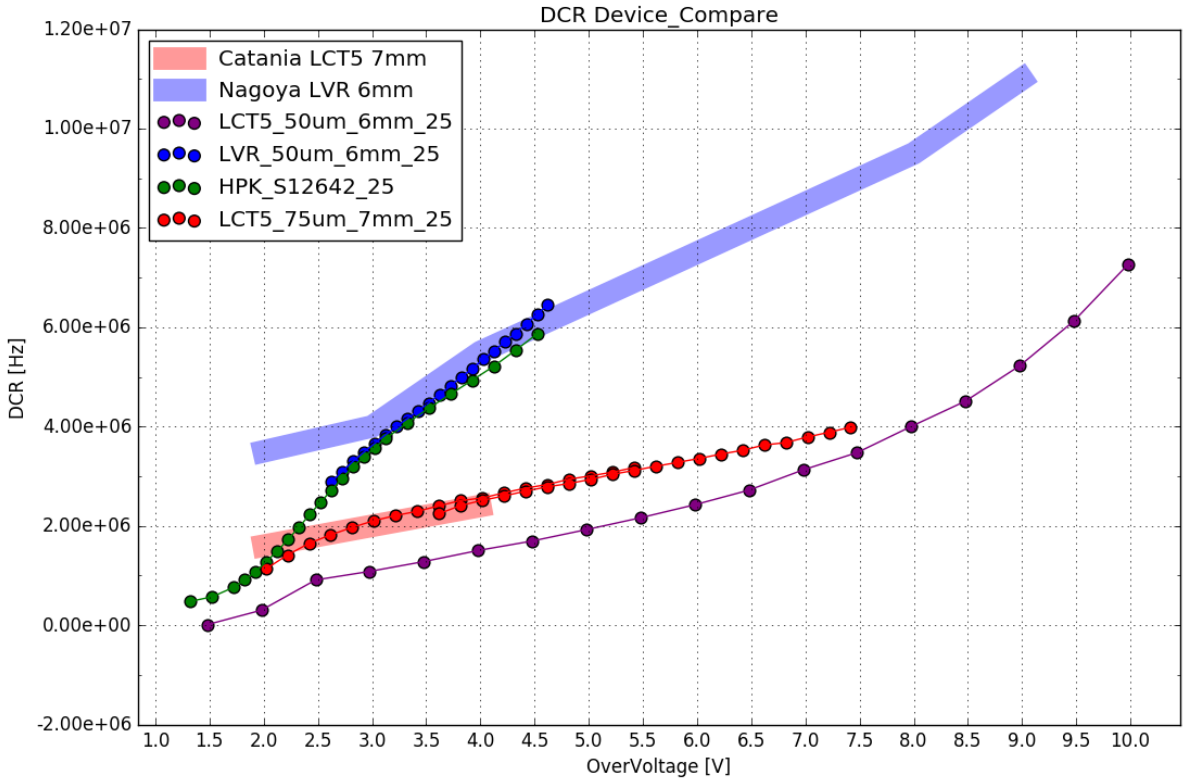


Figure 53: Dark Count Rate comparison of measured devices at 25°C. Description

1128 results, while matching and showing the same trend, the LVR 6mm results deviate. Between an
 1129 over-voltage of 3V and 4V the results overlap, the trend on the other hand is obviously different.
 1130 Additionally the limit on the higher range due to noise makes it impossible to compare against
 1131 the full range measured by the external group, so the DCR for LVR 6mm must be labeled as not
 1132 matching.

1133 7.2 Optical Cross Talk

1134 The comparison of the Optical Cross Talk between the different groups and the results presented
 1135 in this paper are dependent of the analysis and acquisition procedure. Extended trace analysis,
 1136 utilized in this paper captures all aspects of the Optical Cross Talk, prompt and delayed as well
 1137 as afterpulsing. The procedure of time window analysis, utilized by the groups being compared
 1138 to, are, due to their limited window, either biased towards the prompt cross talk or in extreme
 1139 cases, will not be able to capture delayed cross talk or time-delayed afterpulsing at all. Com-
 1140 paring data analysis techniques, for example, at the University of Leicester is therefore a vital
 1141 step. Their approach utilizes a pulsed laser as light source and involves no cooling of the SiPM
 1142 tile. The waveforms are extracted from the scope and a small time window is defined from
 1143 the known time position window of the incident pulse to search for peaks, find their value and
 1144 generate a histogram. To the pulse area histogram, a theoretical model of contributing factors
 1145 is fitted. This theoretical model simulates characteristics, updating continuously to find their cor-

1147 rect values. Those values are the full set of characteristics of the device in testing, among them:
 1148 gain curve, breakdown-voltage, OCT, PDE, noise, dynamic range, crosstalk probability.
 1149 There are a number of differences in their approach compared to the one utilized in this paper,
 1150 most important is the time window size. If the window after an incident pulse is too short,
 1151 data loss is a possibility, depending on the delay time of delayed cross-talk and afterpulsing
 1152 assisted by traps with long lifetimes. This is a problem, especially with devices of the LCT5 gen-
 1153 eration implementing physical trenches isolating the cells and effectively reducing the prompt
 1154 cross-talk, here the contribution from the prompt cross-talk to the overall Optical Cross Talk is
 1155 lowered. Missing data from delayed cross-talk and afterpulsing, because it will not be recorded
 1156 yet, would lead to errors in the overall Optical Cross Talk results being lower than expected.
 1157

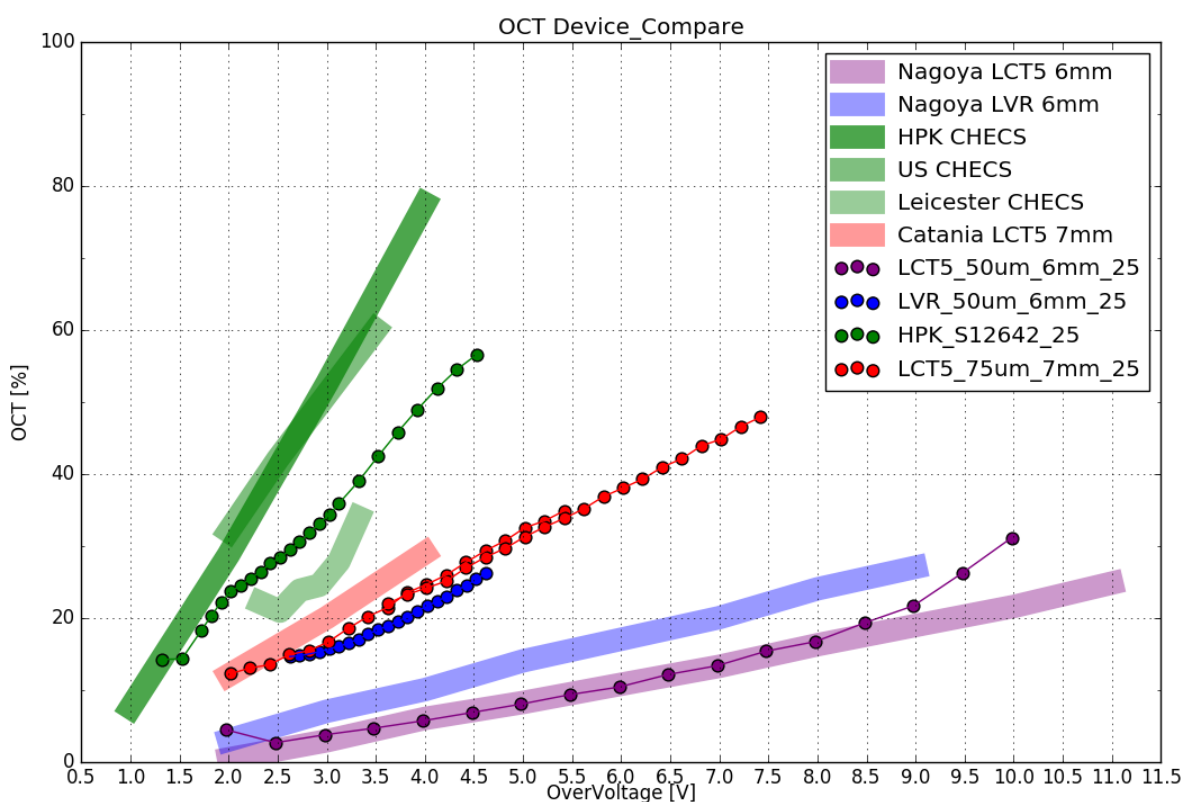


Figure 54: Cross Talk comparison of measured devices at 25°C. Description

1158 This is indeed the case for the S12642 tile in Figure 54 (green). The light green bar below
 1159 (negative y-axis) the dotted data presented in this paper shows the results form the University
 1160 of Leicester indeed being lower. In purple results of the LCT5 S13360 device with physical
 1161 trenches are shown. Compared to results from the University of Nagoya, there is a prominent
 1162 upturn at around an over-voltage of ~8V. This could be due to the differences in analysis tech-
 1163 nique. The University of Nagoya also employs time window analysis. LCT5 posseses lowered
 1164 prompt cross-talk probability, so the contribution of delayed cross-talk to the overall cross-talk
 1165 is higher than for S12642. With rising over-voltage the ratio between prompt and delayed

1166 cross talk shifts towards a higher contribution from delayed cross-talk[14][19]. While at lower
1167 over-voltages ($\sim 0.5V$) the cross-talk is nearly entirely dominated by the prompt cross-talk with
1168 nearly no contribution of delayed cross-talk, at ($\sim 2V$) contributions are mostly equal and at
1169 high over-voltages ($\sim 7V$) the contribution of delayed cross-talk is expected to be above 80%,
1170 probably due to higher penetration depth and avalanche probability.

1171 Results of the LCT5 7mm device from both groups mostly overlap, the slight shift between them
1172 is most likely caused by a small error in the breakdown-voltage calculation, due to no cooling
1173 of the tile in experiments involving light. In addition, the slope of both results seems to be mostly
1174 equal, and the extended range measurement, overlapping with the low-range results confirms
1175 that.

1176 Even though results from 3 different groups mostly correlate, or have at least partially un-
1177 derstood differences, the Optical Cross Talk of LVR 6mm Figure 54 (blue) compared to the
1178 results from the University of Nagoya do not show any correlation at all. This is concerning,
1179 because comparing S13360 (purple) to the same group showed strong correlation over a wide
1180 over-voltage range. Since there is also no datasheet present yet, this device is a prototype, the
1181 assumption is that the device examined is physically different than the device present at Nagoya.
1182 It may just be a difference in coating, which combined with the TSV technology could lead to
1183 the present uncorrelation[19].

1184 7.3 Photon Detection Efficiency 1185

1186 The measurement technique in this paper utilizes only dark counts and aims at giving an un-
1187 derstanding of the Optical Cross Talk and temperature dependencies of the different SiPMs
1188 proposed, therefore no PDE measurements are possible. The point of operation with the highest
1189 PDE as well as the PDE versus OCT behaviour is determined by a different group in Japan, at
1190 the University of Nagoya. See Figure (56) for the current results of their endeavors. A figure
1191 showing the behavior of PDE versus OCT is the usual procedure of comparing SiPMs, it gives a
1192 correlated overview of the two most significant characteristics. This gives the most insight of the
1193 capabilities of the different devices compared to the two proposed operating points chapter(7).
1194 For consistency and to make comparison between group results easier, the PDE ascertained by
1195 the groups, of devices in common, compared to the resulting Optical Cross Talk from this paper
1196 produces Figure (55).

1197

1198 Comparing all devices at the two proposed points of operation produces the table in
1199 Figure(57). This table together with Figure (55) of the 5 measured devices in this thesis,
1200 where PDE data is accessible, is used to confirm results between groups and assist in the de-
1201 cision on the most viable SiPM for CHEC-S. The final decision will be taken by the group at the
1202 University of Nagoya, by Hiro Tajima, the Photosensor work group lead scientist? of GCT based
1203 on measurements on substantially more devices (see appendix H, for the complete list).

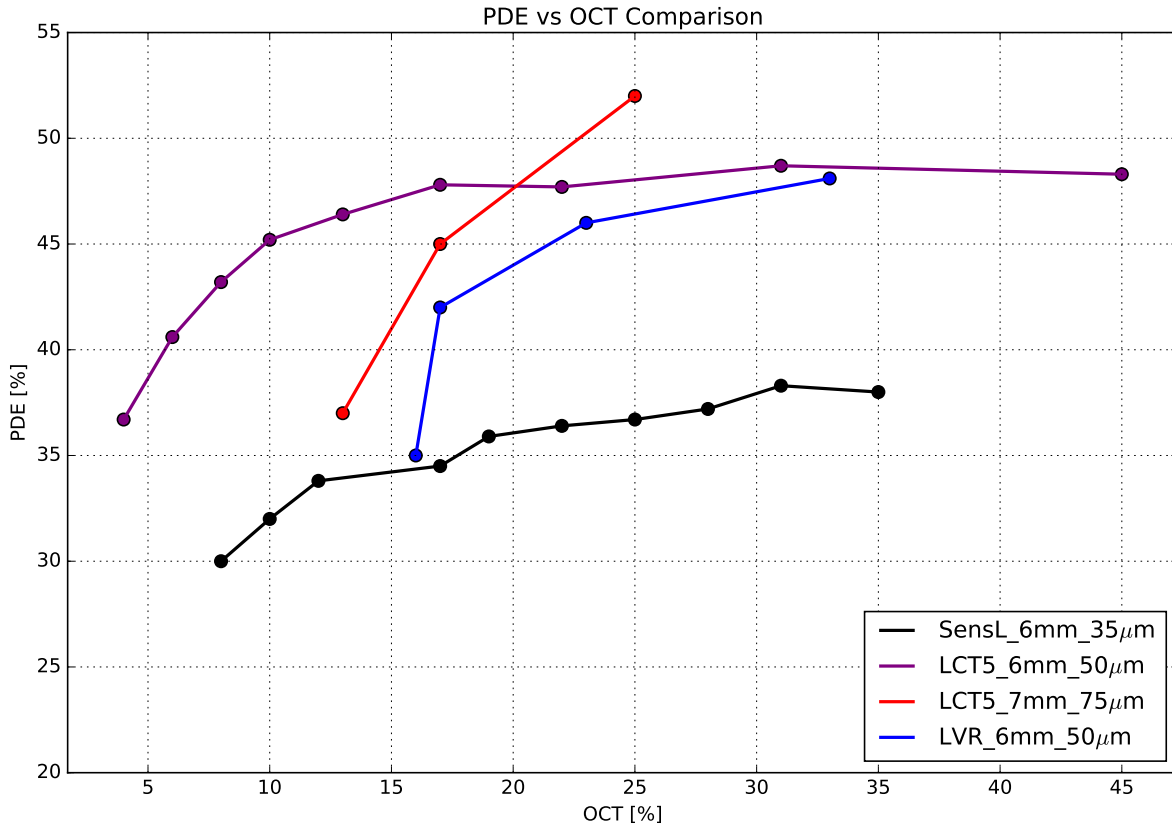


Figure 55: PDE results from the University of Nagoya parametrized with OCT results from this paper, where available. PDE measurements at $\lambda = 400\text{nm}$. An optimum device for IACT application would be in the upper left region.

1204 The PDE of SiPMs, when plotted versus the corresponding OCT at a common over-voltage point
 1205 show the behaviour in Figure (55). A clearly visible saturation after a certain OCT marks the
 1206 point, from where an increase in power no longer increases photon-detection capabilities. An
 1207 increase in OCT without rising PDE would have a adverse effect on the detectors resolution.
 1208

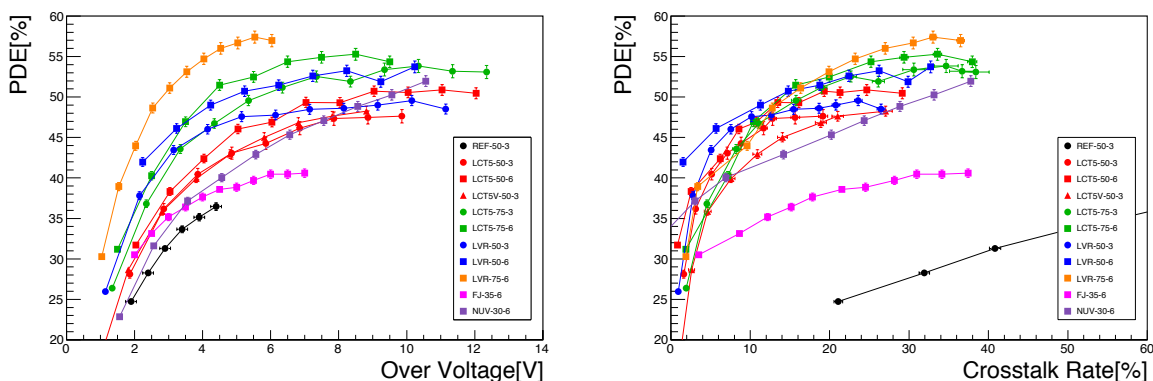


Figure 56: PDE Comparison Plots from the University of Nagoya at $\lambda = 400\text{nm}$

1209 The prototype LCT5 7mm fig(55)(red) device reaches the highest PDE. While the prelimi-
1210 nary external measurements show only 3 datapoints, a trend above 50 % is visible. This is
1211 expected for devices with larger cell- and pixel-size possesing a higher fill-factor. The increase
1212 in size and therefore PDE comes with a trade-off, increasing size comes with a rise of DCR and
1213 OCT, which are very high at this point (at $\sim 25\%$).

7.4 Point of Operation Comparison

Device	Min. OCT			Max. PDE		
	OCT	DCR	PDE	OCT	DCR	PDE
CHECS	15%	0.5 MHz	25% (DS)	50%	5 MHz	48% (DS)
LCT5 6mm	15%	3.4 MHz	49% (Nagoya)	22%	5 MHz	51% (Nagoya)
LCT5 7mm	15%	2.0 MHz	42% (Catania)	25%	2.5 MHz	53% (Catania)
LVR 6mm	15%	2.5 MHz	43% (Nagoya)	>27%	>6MHz	>50% (Nagoya)
SensL	15%	3.0 MHz	37% (Nagoya)	30%	6 MHz	40% (Nagoya)

Figure 57: Comparison table of the measured devices in the style of the 2 proposed operation points for CHEC-S. First point represents minimal achievable OCT, second point represents maximum achievable PDE. PDE values taken from results of other groups. Note that the LCT5 6mm device can achieve even lower OCT value ($\sim 3\%$ at $V_{ov} = 2.5$)

1216 8 further analysis

1218 8.1 multi incident probability and optical Cross Talk

1220 With increasing Dark Count Rate the probability of two dark events happening at the same
1221 time rises with increasing bias-voltage. Taking for example the Dark Count Rate of S13360 and
1222 taking the FWHM of the characteristic pulse we can calculate the probability for every dark rate
1223 at every bias-voltage and can extract a probability curve. Wouldnt that just make the DCR rise
1224 even higher since 1 2p.e. are now 2 1p.e.s' ?? nonononono

1225 multi incident has influence on optical cross talk, 2 ones are interpreted as 1 2 and are there-
1226 fore put into the 2p.e. peak of the histogram, leading to calculation errors.

1227 8.2 Prompt and delayed cross talk ratio

1229 What happens if we take the OCT of S13360 and scale it with an expected prompt to delayed
1230 crosstalk ratio. evidence only from confidential HPK talk, need citations. Could just make new
1231 plots in HD, evaluate.

1232 9 Conclusion and Outlook

1234 _____> Hmhmhm

1235 For that purpose 5 different SiPM from two manufacturers have been examined.

10 Glossary

- 1238 1. SiPM - Silicon Photomultiplier
- 1239 2. IACT
- 1240 3. CTA - Cherenkov Telescope Array
- 1241 4. LST
- 1242 5. MST
- 1243 6. SST
- 1244 7. GCT
- 1245 8. CHEC
- 1246 9. HPK - Hamamatsu Photonics K.K.
- 1247 10. SensL - Sense Light

1248 1249 11 Bibliography

1250 1251 References

- 1252 [1] Jim Hinton et al. *Teraelectronvolt Astronomy* Ann. Rev. Astron. Astrophys., 47:523
- 1253 [2] The CTA Consortium *Design Concepts for the Cherenkov Telescope Array CTA, An Advanced*
1254 *Facility for Ground-Based High-Energy Gamma-Ray Astronomy* ; arXiv:1008.3703v3 [astro-
1255 ph.IM] 11 Apr 2012
- 1256 [3] Teresa Montaruli et al. *The small size telescope projects for the Cherenkov Telescope Array*
1257 arXiv:1508.06472v1 [astro-ph.IM]
- 1258 [4] *The ASTRONET Infrastructure Roadmap* ISBN: 978-3-923524-63-1
- 1259 [5] Jim Hinton et. al *Seeing the High-Energy Universe with the Cherenkov Telescope Array* As-
1260 troparticle Physics 43 (2013) 1-356
- 1261 [6] R. López-Coto for the HAWC collaboration *Very high energy gamma-ray astronomy with*
1262 *HAWC* arXiv:1612.09078v1 [astro-ph.IM] 29 Dec 2016
- 1263 [7] John Murphy *SensL J-Series Silicon Photomultipliers for High-Performance Timing in Nuclear*
1264 *Medicine*
- 1265 [8] A. N. Otte et al. *Characterization of three high efficient and blue sensitive Silicon photomul-*
1266 *tipliers* arXiv:1606.05186v2 [physics.ins-det] 26 Jan 2017
- 1267 [9] A. Bouvier et al. *Photosensor Characterization for the Cherenkov Telescope Array: Silicon*
1268 *Photomultiplier versus Multi-Anode Photomultiplier Tube* ; arXiv:1308.1390v1 [astro-ph.IM]
1269 6 Aug 2013
- 1270 [10] V. Vassilieva , S. Fegan *Wide field aplanatic two-mirror telescopes for ground-based*
1271 *gamma-ray astronomy* Astropart. Phys. 28 (2007) 10, [astro-ph/0612718] arXiv:astro-
1272 ph/0612718v2 12 Apr 2007
- 1273 [11] A. Zech, J.-P. Amans, S. Blake et al. *SST-GATE: A dual mirror telescope for the Cherenkov*
1274 *Telescope Array* arXiv:1307.3035v1 [astro-ph.IM] 11 Jul 2013
- 1275 [12] Julien Rousselle et al. *Construction of a Schwarzschild-Couder telescope as a candidate for*
1276 *the Cherenkov Telescope Array: status of the optical system* arXiv:1509.01143v1 astro-ph.IM
- 1277 [13] J. Rosado S. Hidalgo *Characterization and modeling of crosstalk and afterpulsing in Hamamatsu*
1278 *silicon photomultipliers.* arXiv:1509.02286v2 [physics.ins-det] 21 Oct 2015
- 1279 [14] K. Boone, Y. Iwai, F. Retiere, C. Rethmeier *Delayed avalanches in Multi-Pixel Photon Counters*
1280 arXiv:1703.04651v1 [physics.ins-det] 14 Mar 2017

- 1281 [15] Robert G. Wagner et al. *The Next Generation of Photo-Detectors for Particle Astrophysics*
1282 arXiv:0904.3565v1 [astro-ph.IM] 22 Apr 2009
- 1283 [16] *Opto-semiconductor handbook Chapter 03 Si APD, MPPC*. Hamamatsu Photonics K.K.
- 1284 [17] Jonathan Biteau et al *Performance of Silicon Photomultipliers for the Dual-Mirror Medium-*
1285 *Sized Telescopes of the Cherenkov Telescope Array* arXiv:1508.06245v1 [astro-ph.IM] 25 Aug
1286 2015
- 1287 [18] Richard White *private communication*. 2017
- 1288 [19] Koei Yamamoto *private correspondence*. 2016
- 1289 [20] Luigi Tibaldo *Initial testing at MPIK (wb July 18 2016)* July 2016
- 1290 [21] T. C. Awes et al. *Configurable electronics with low noise and 14-bit dynamic range for*
1291 *photodiode-based photon detectors* Nuclear Inst. and Methods in Physics Research, Mai 2006
- 1292 [22] Maurice Stephan. *Design and Test of a Low Noise Amplifier for the Auger Radio Detector*
1293 Diploma Thesis, RWTH Aachen University, July 2009
- 1294 [23] Benjamin Glauß. *Optical Test Stand and SiPM characteriation studies*. Master's Thesis,
1295 RWTH Aachen University, June 2012.
- 1296 [24] Hiro Tajima *Roadmap for Procurement of SiPMs*, GCT Meeting, Amsterdam, February
1297 15–17, 2017
- 1298 [25] http://astro.desy.de/gamma_astronomy/cta/index_eng.html
- 1299 [26] [http://www.ung.si/en/research/laboratory-for-astroparticle-physics/
1300 projects/cta/](http://www.ung.si/en/research/laboratory-for-astroparticle-physics/projects/cta/)
- 1301 [27] [http://www.ung.si/en/research/laboratory-for-astroparticle-physics/
1302 projects/fermi-lat/](http://www.ung.si/en/research/laboratory-for-astroparticle-physics/projects/fermi-lat/)
- 1303 [28] [http://212.71.251.65/aspera//index.php?option=com_content&task=
1304 blogcategory&id=111&Itemid=234](http://212.71.251.65/aspera//index.php?option=com_content&task=blogcategory&id=111&Itemid=234)

12 Appendix

A CTA

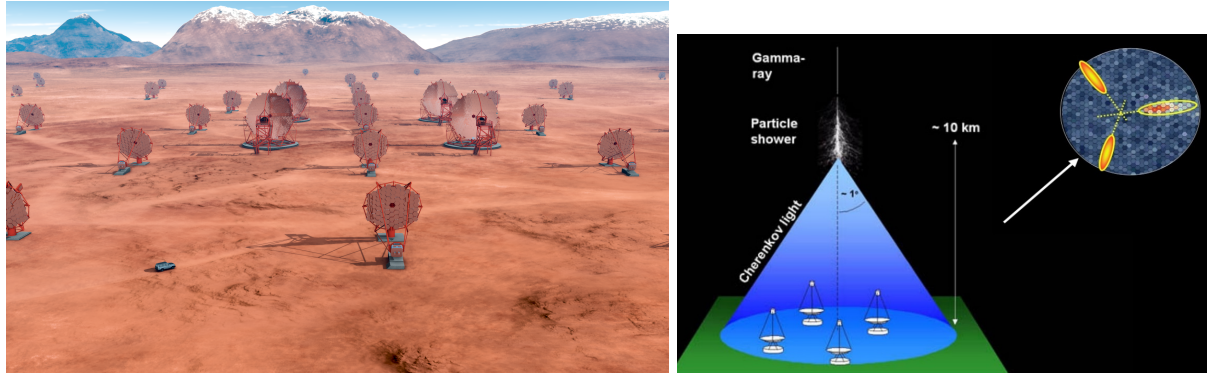


Figure 58: A render of the finished CTA Array at the site in Chile (left) with visible LSTs and MSTs, and the Shower Path Reconstruction technique of the stereoscopic view employed by current IACT experiments like HESS, MAGIC, VERITAS (right).

B progenitor experiments of CTA



Figure 59: IACT Projects: HESS in the Khomas Highland, Namibia. MAGIC at the Roque de los Muchachos Observatory on La Palma , one of the Canary Islands. VERITAS at Mount Hopkins, Arizona, USA

1311
1312

C OCT dependency on cellsize

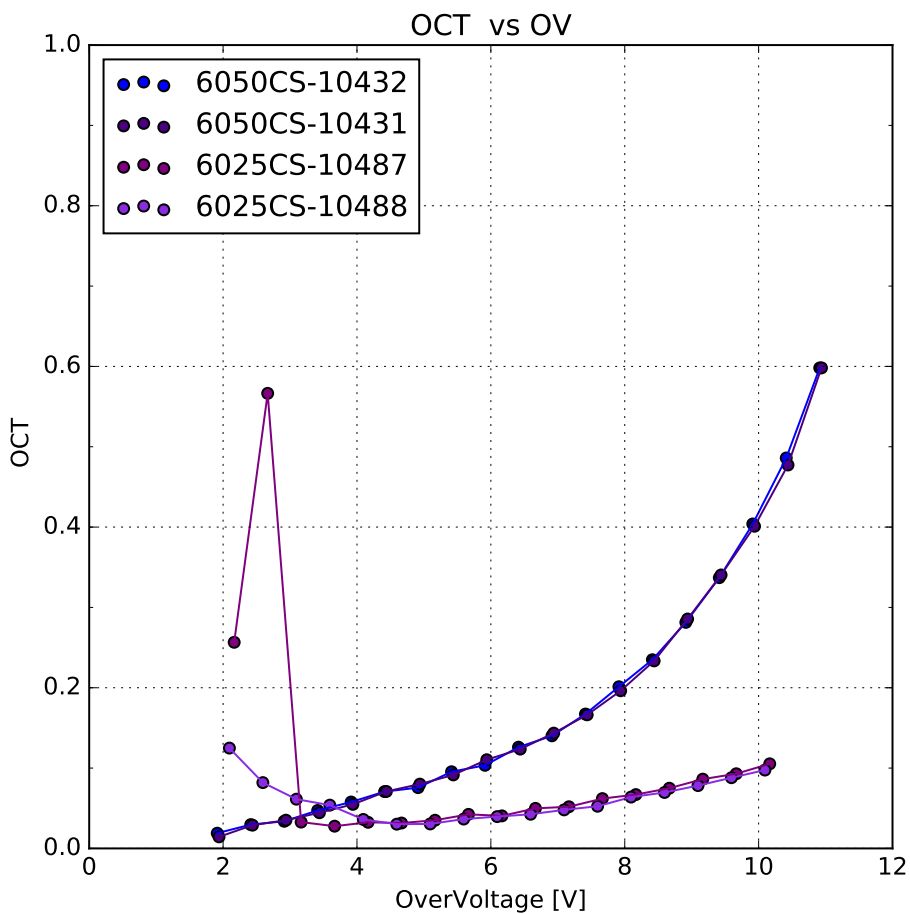
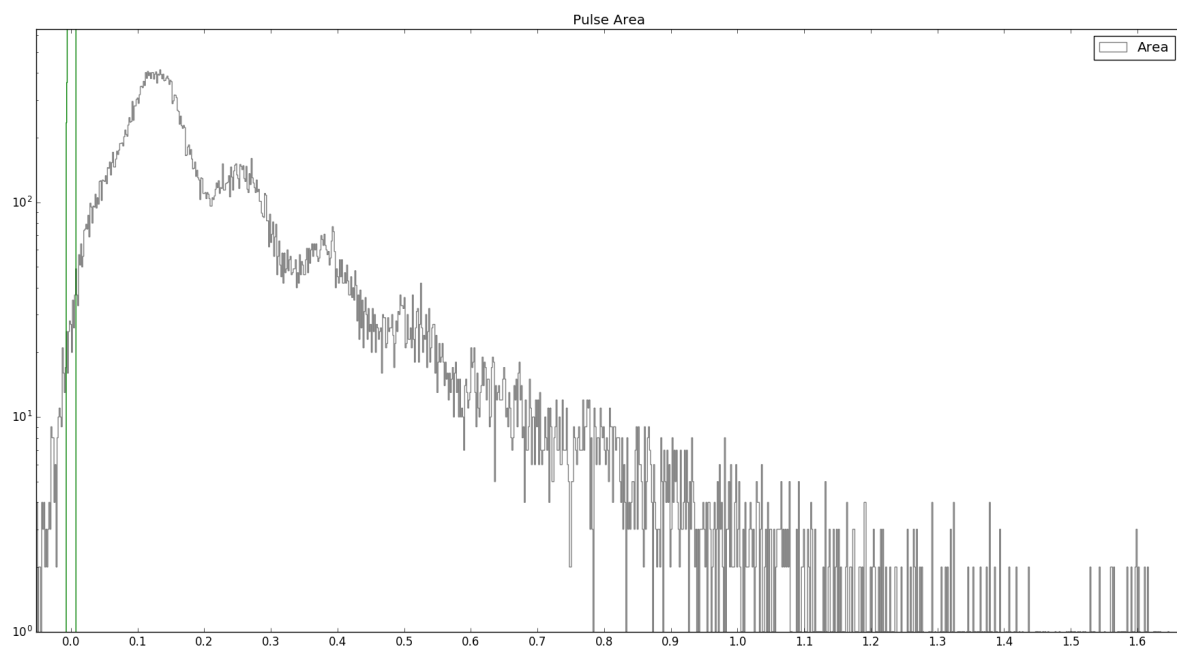
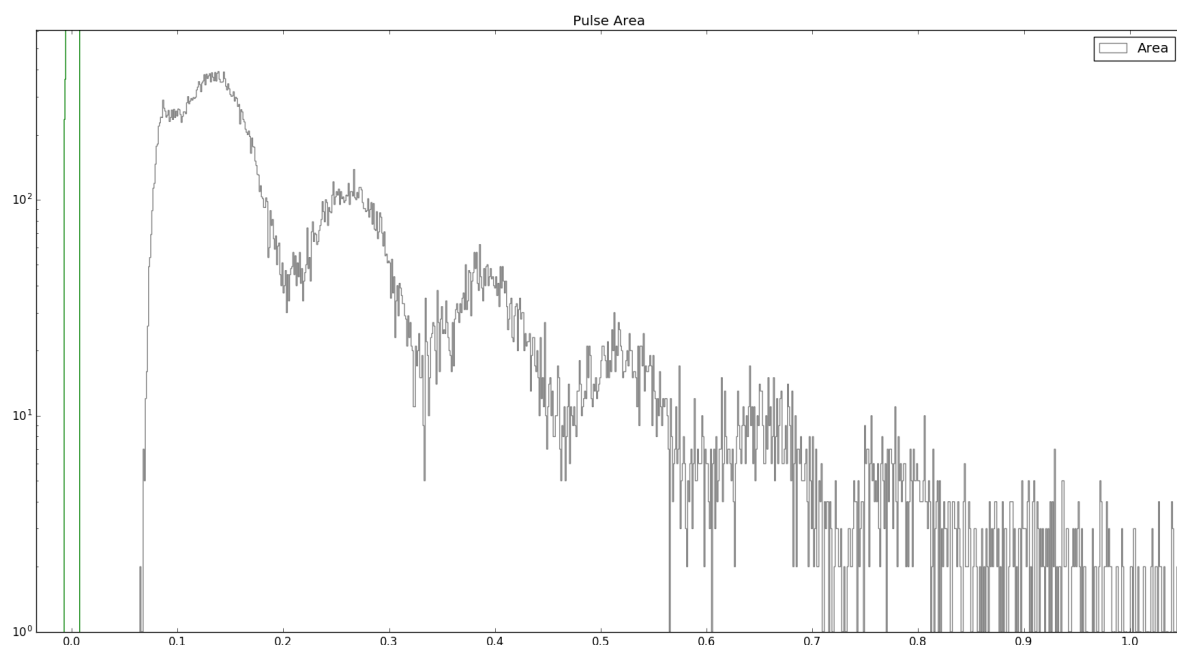


Figure 60: Results of the Optical Cross Talk of 2 sets of 2 similar HPK S13360 devices, that only differ in their respective cell-size. HPK S13360 is the first device incorporating physical trenches in the upper layer, optically isolating each cell. Consequence to this is a drastic reduction in prompt cross-talk. Delayed cross-talk and afterpulsing are basically unaffected. Upscaling the $25\mu\text{m}$ results shows an overlap between the 2, see text.

1313 In Figure (60) the results of the complete Optical Cross Talk of 2 sets of $50\mu\text{m}$ and $25\mu\text{m}$ HPK
 1314 S13360 devices are shown. Plotting the results of 2 similar devices, only different in their cell-
 1315 size, and then multiplying the $25\mu\text{m}$ results by the factor derived from their difference in area,
 1316 here 4, a correlation is visible. Scaling up the Optical Cross Talk of the $25\mu\text{m}$ cell, shows an over-
 1317 lap between the 2 cell-sized pixels. This means, that the Optical Cross Talk is directly area and
 1318 therefore cell-size dependent. Research by J. Rosado and S. Hidalgo [13] on the cross-talk prob-
 1319 ability of Hamamatsu SiPMs showed through Monte Carlo simulation, that the prompt crosstalk
 1320 mostly takes place in a small area of pixels (~ 8) around the primary one. Which means, that
 1321 the cross-talk is directly increasing with increasing cell-size, or in other words: with chance to
 1322 diffuse to a neighboring cell. Small cells reduce the chance, as there is less area to a neighboring
 1323 cell to pass through.

1324 Since the measurements conducted by me do not differ between the range of secondary
1325 avalanche effects, the Optical Cross Talk shown contains every aspect, prompt and delayed
1326 as well as afterpulsing.

D Pulse Area Spectra of different integration window widths



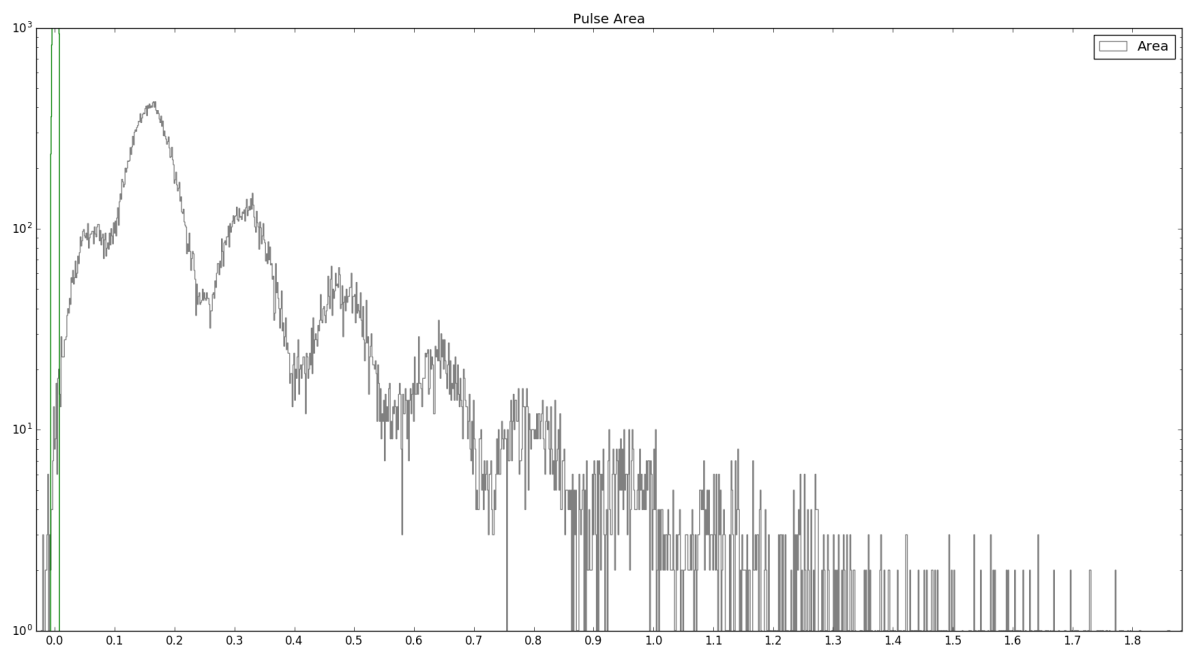


Figure 61: Pulse Area Spectra with window widths of 5 left 5 right (top), 5 left 20 right (middle), 10 left 10 right (bottom) bins respectively. Left of the 1p.e. peak of the top picture a part of the 0p.e. peak is visible. The middle figure shows the distortion an asymmetrical integration window causes. The bottom figure is the employed integration window to derive the pulse area histogram.

E BreakdownVoltage

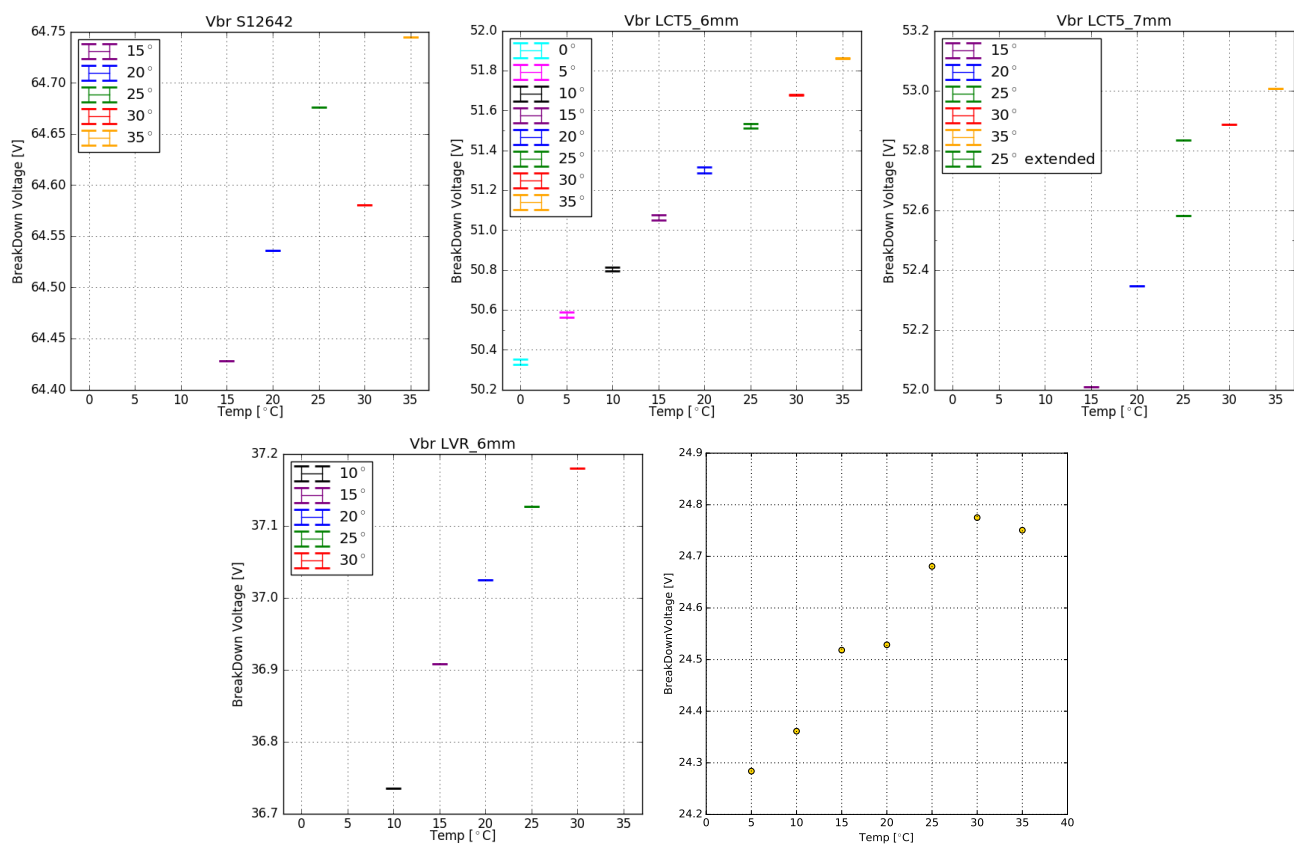


Figure 62: Dependency of the breakdown-voltage of temperature for the 5 measured devices.

For LCT5 7mm , the extended range measurement adds an extra datapoint at 25°C
 HPK S12642 (CHEC-S) (top left) ; HPK LCT5 6mm (top middle) ; HPK LCT5 7mm (top right) ; HPK LCT5 LVR 6mm (bottom left) ; SensL FJ60035 (bottom right).

Device	$\Delta V / T$ [mV/°C]
CHECS	13.1 ± 4.1
LCT5 6mm	43.5 ± 0.4
LCT5 7mm	53.0 ± 4.0
LVR 6mm	25.6 ± 2.6
SensL	15.0 ± 1.1

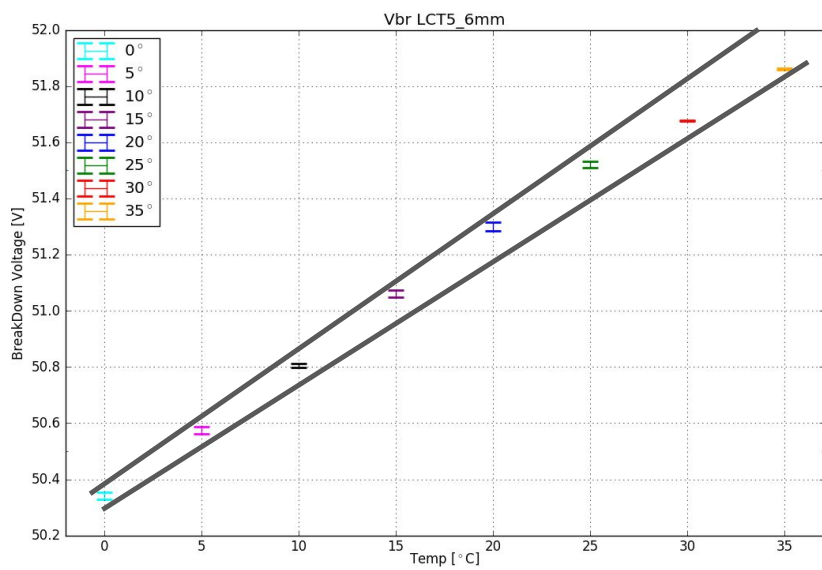
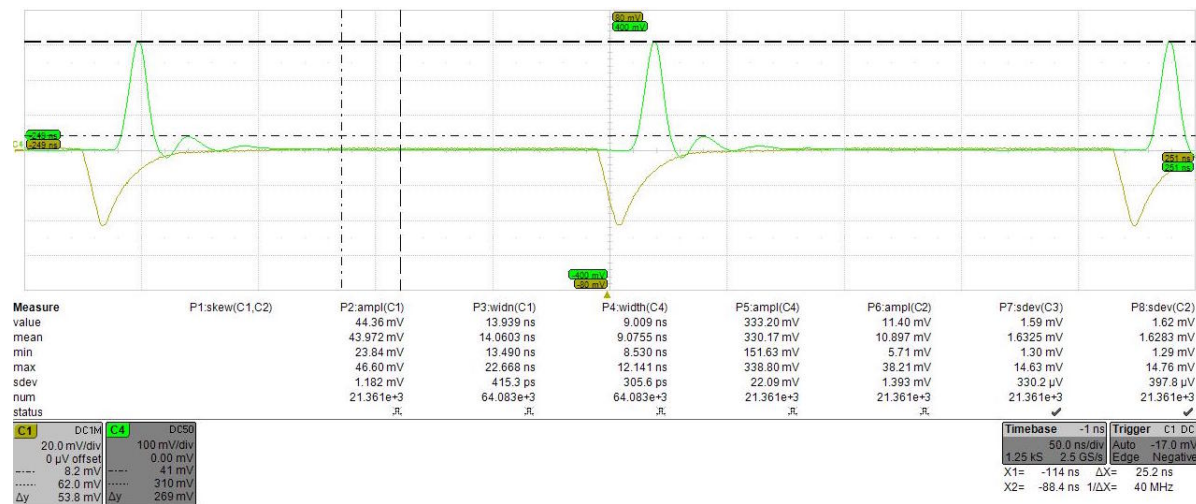
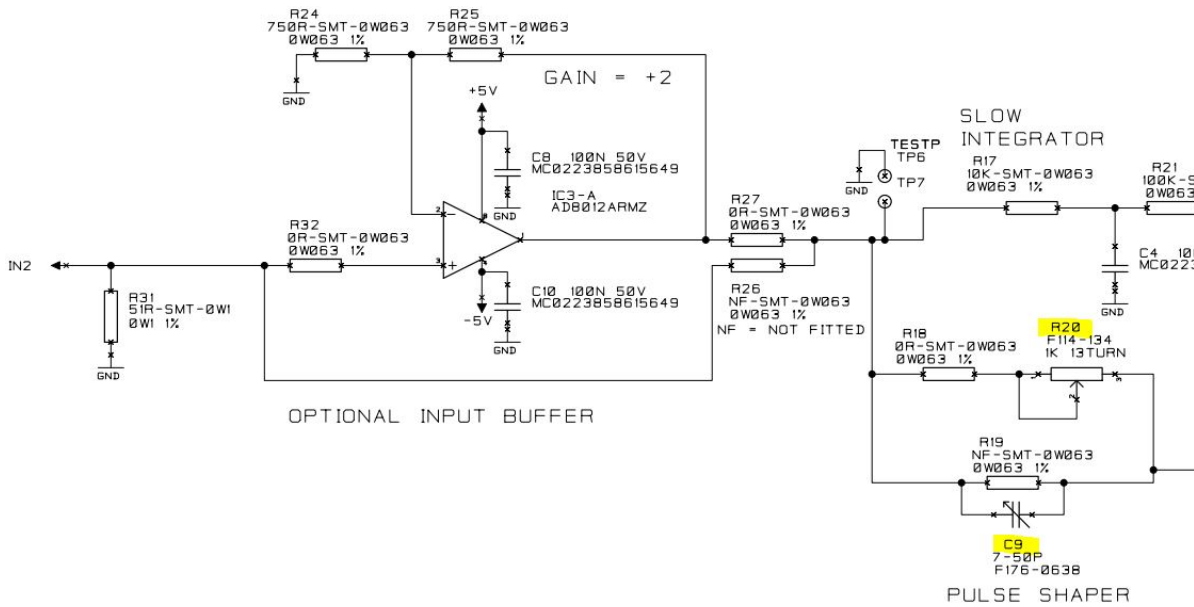


Figure 63: The extracted breakdown-voltage dependence of all measured devices, derived from two regression lines and their mean. For some devices the breakdown-voltage dependency is known through datasheet values. S12642 = 60mV/°C, S13360 = 54mV/°C, SensL FJ60035 =<21.5mV/°C

F Shaper**Figure 64:** Experimental setup scheme, Annotations see text**Figure 65:** Experimental setup scheme, Annotations see text

1333
1334

G Pulse Area and Height Spectra

1335 Example pulse area spectra

H SiPM list tested at University of Nagoya**Test Samples**

Product ID	Pixel size	Cell size	Technology	Short name	Fill factor
S12572-050C	3 mm	50 µm	Standard	REF-50-3	62%
S13360-3050CS	3 mm	50 µm	LCT5	LCT5-50-3	74%
S13360-3050VE	3 mm	50 µm	LCT5, epoxy	LCT5E-50-3	74%
S13360-6050CS	6 mm	50 µm	LCT5	LCT5-50-6	74%
S13360-3075CS	3 mm	75 µm	LCT5	LCT5-75-6	74%
S13360-6075CS	6 mm	75 µm	LCT5	LCT5-75-6	82%
LVR-3050CS	3 mm	50 µm	LVR	LVR-50-3	74%
LVR-6050CS	6 mm	50 µm	LVR	LVR-50-6	74%
LVR-6075CS	6 mm	75 µm	LVR	LVR-75-6	82%
LVR-7050CS	7 mm	50 µm	LVR	LVR-50-7	74%
MicroFJ-SMA-60035	6 mm	35 µm	TSV	FJ-35-6	?
FBK NUV	6 mm	30 µm	NUV	NUV-30-6	49%

Roadmap for Procurement of SiPMs
GCT Meeting, Amsterdam, FEB 15–17 2017

3/11

Figure 66: List of devices in testing at the University of Nagoya, Japan. Taken from [24]

I CHEC-S pixel comparison

- 1340 Comparison of results from 10 different pixels on the CHEC-S (HPK S12642-1616PA-50) array.
 1341 Every pixel is analyzed with the same technique and analysis parameters.

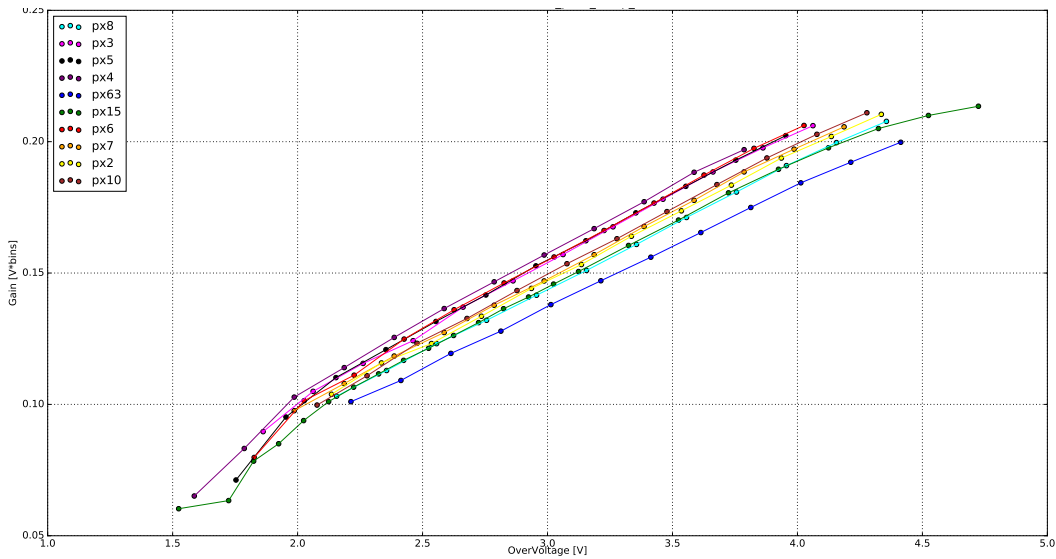


Figure 67: Gain comparison of 10 different pixels of the CHEC-S (HPK S12642-1616PA-50) array

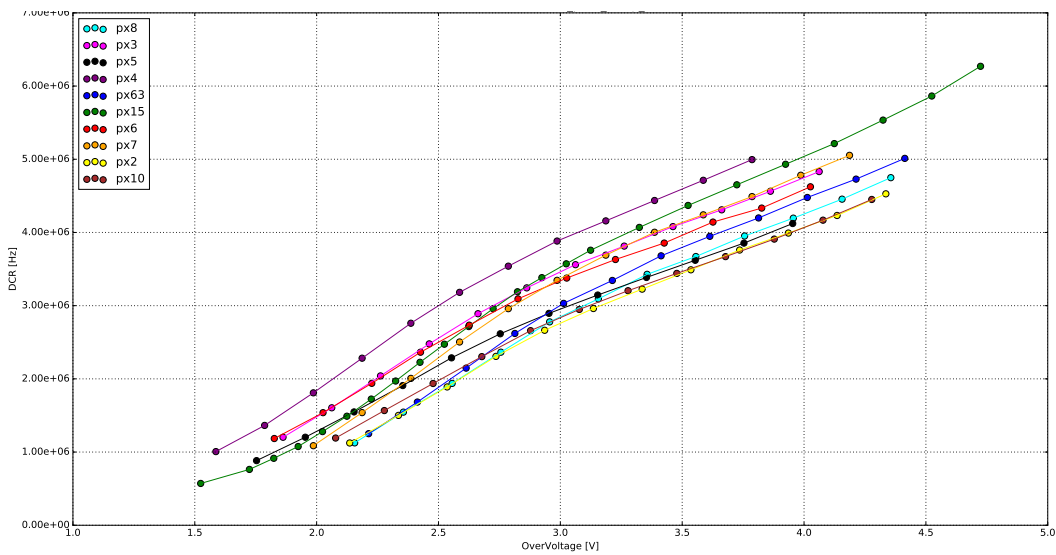


Figure 68: DCR comparison of 10 different pixels of the CHEC-S (HPK S12642-1616PA-50) array

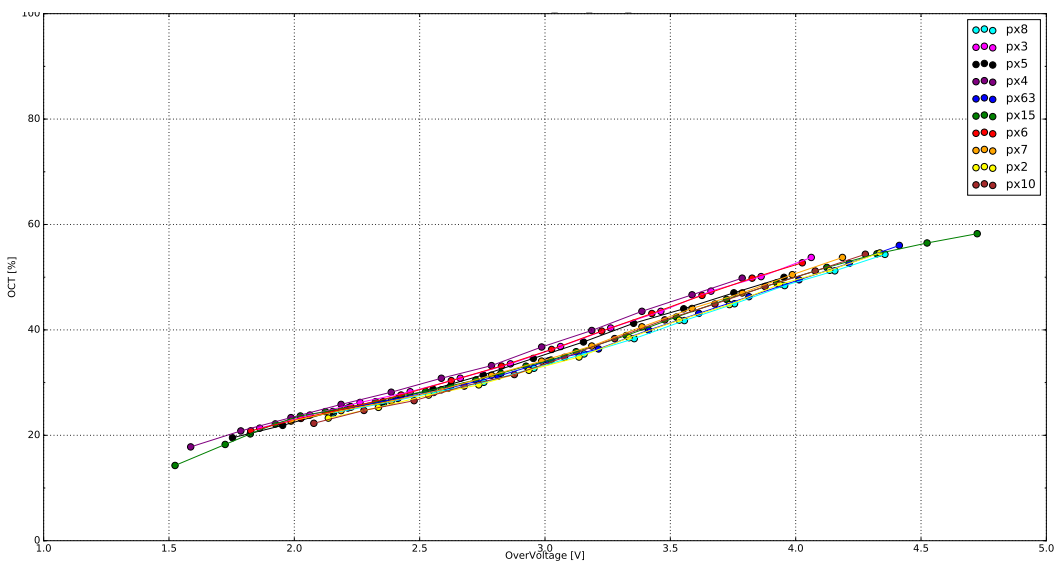
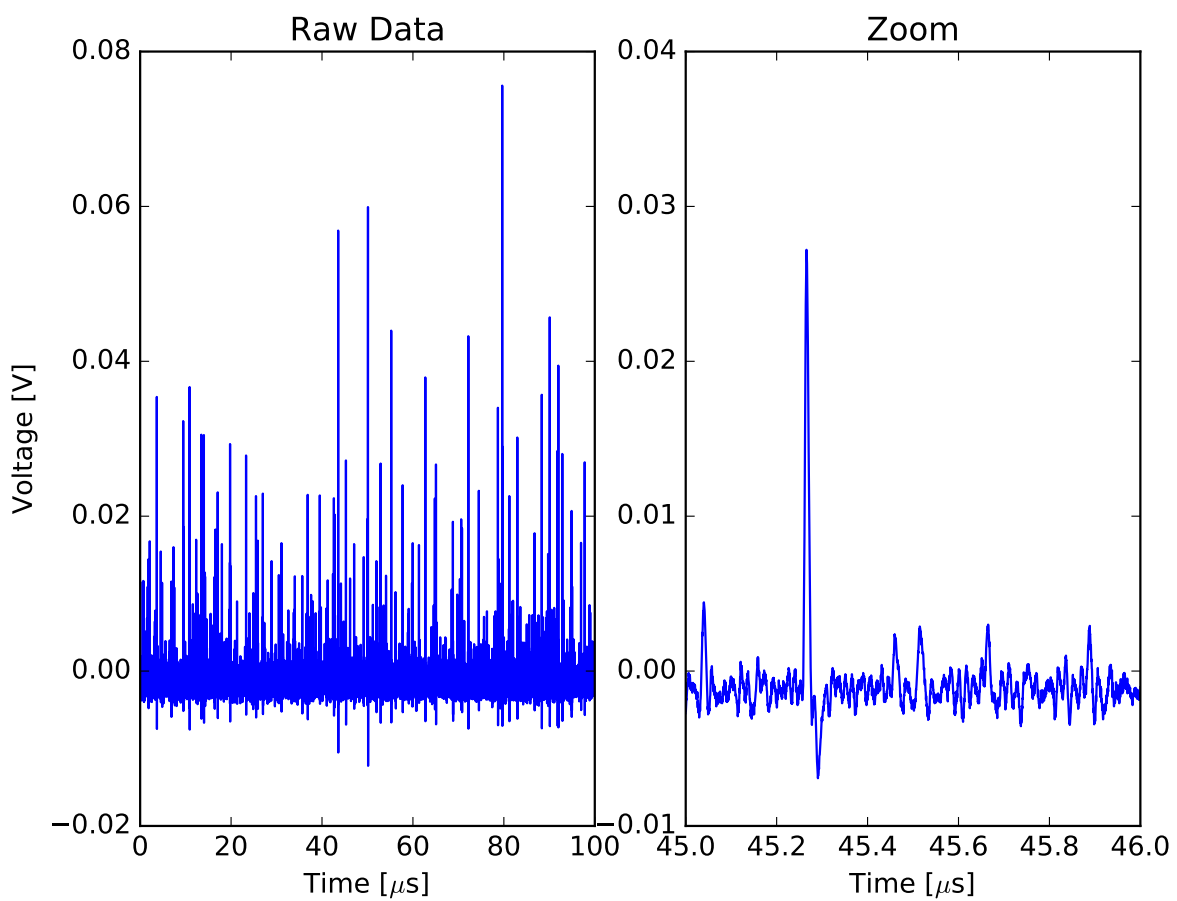


Figure 69: OCT comparison of 10 different pixels of the CHEC-S (HPK S12642-1616PA-50) array

J Additional Data Analysis Plots**Figure 70:** Description

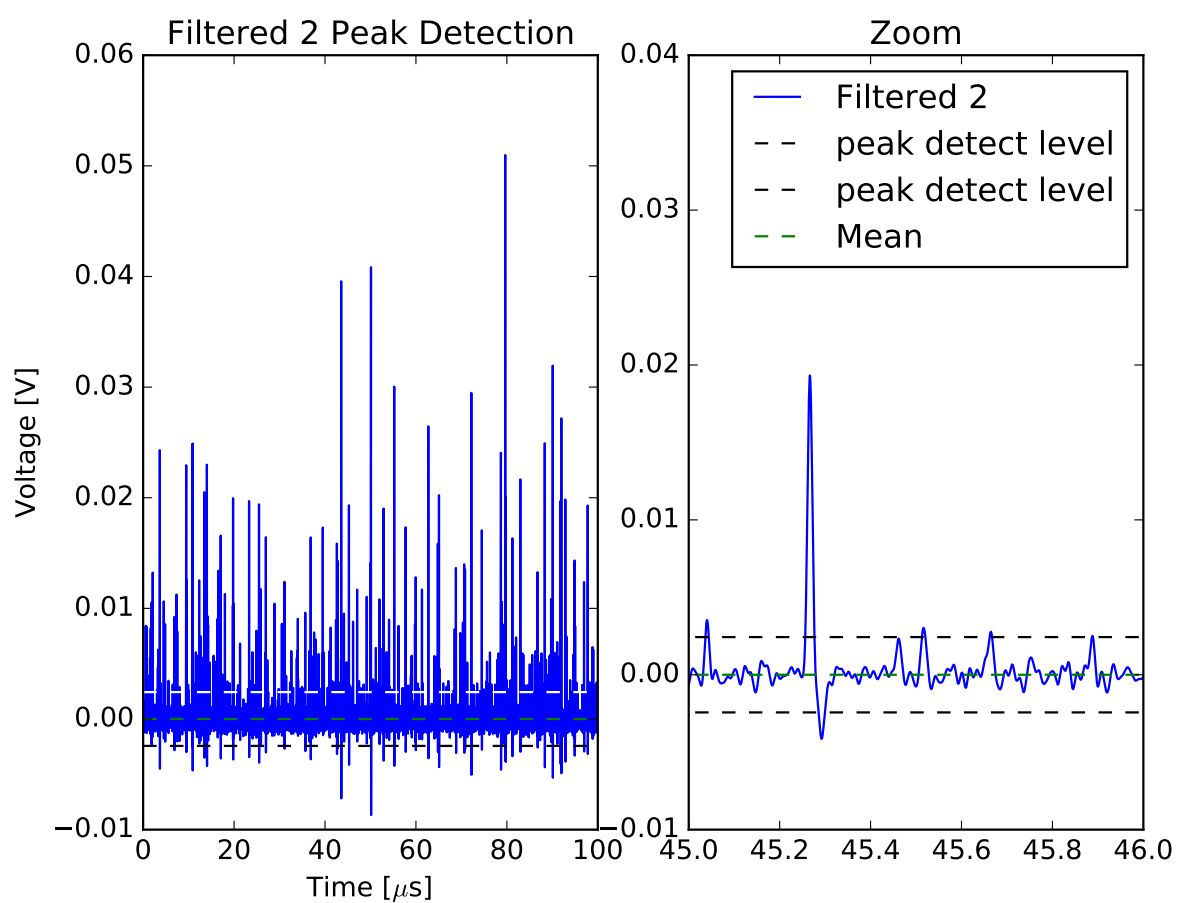


Figure 71: Description

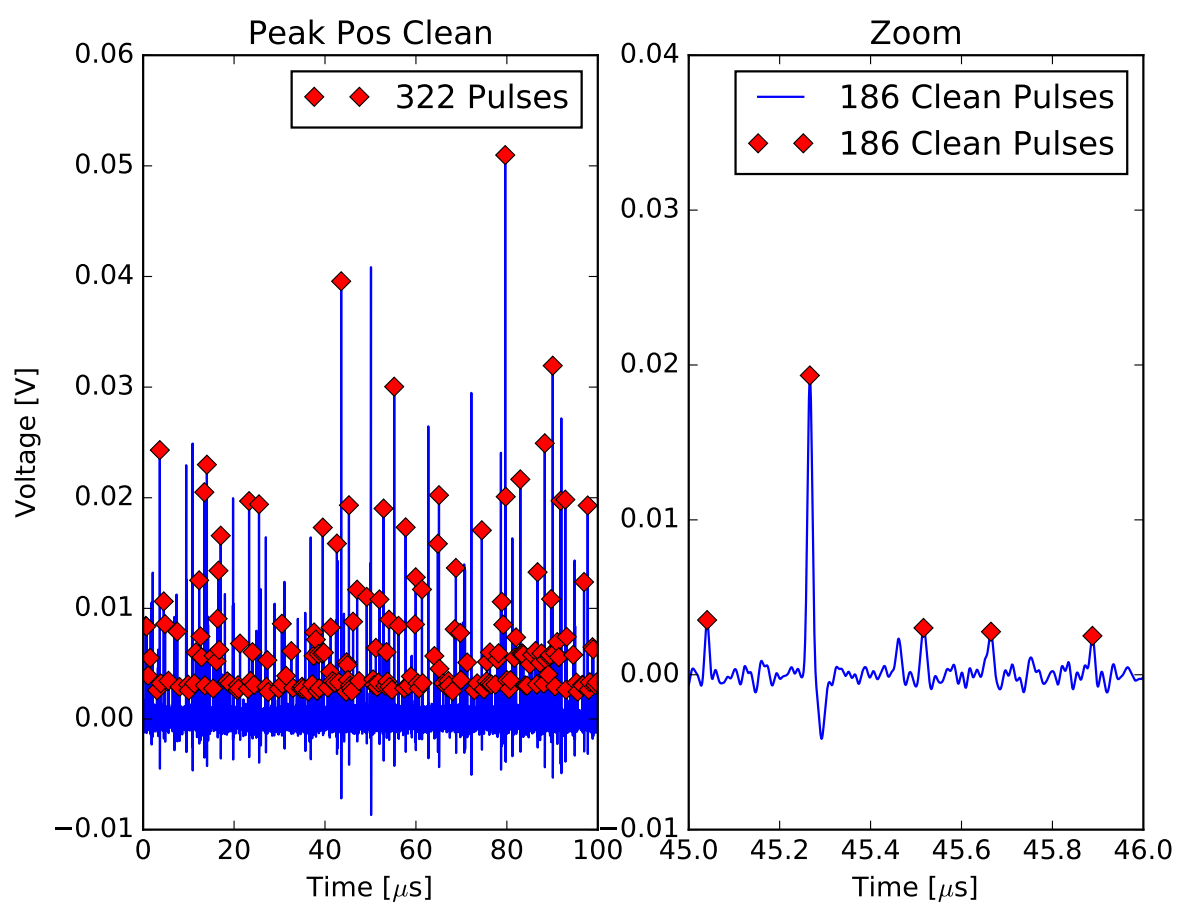


Figure 72: Description

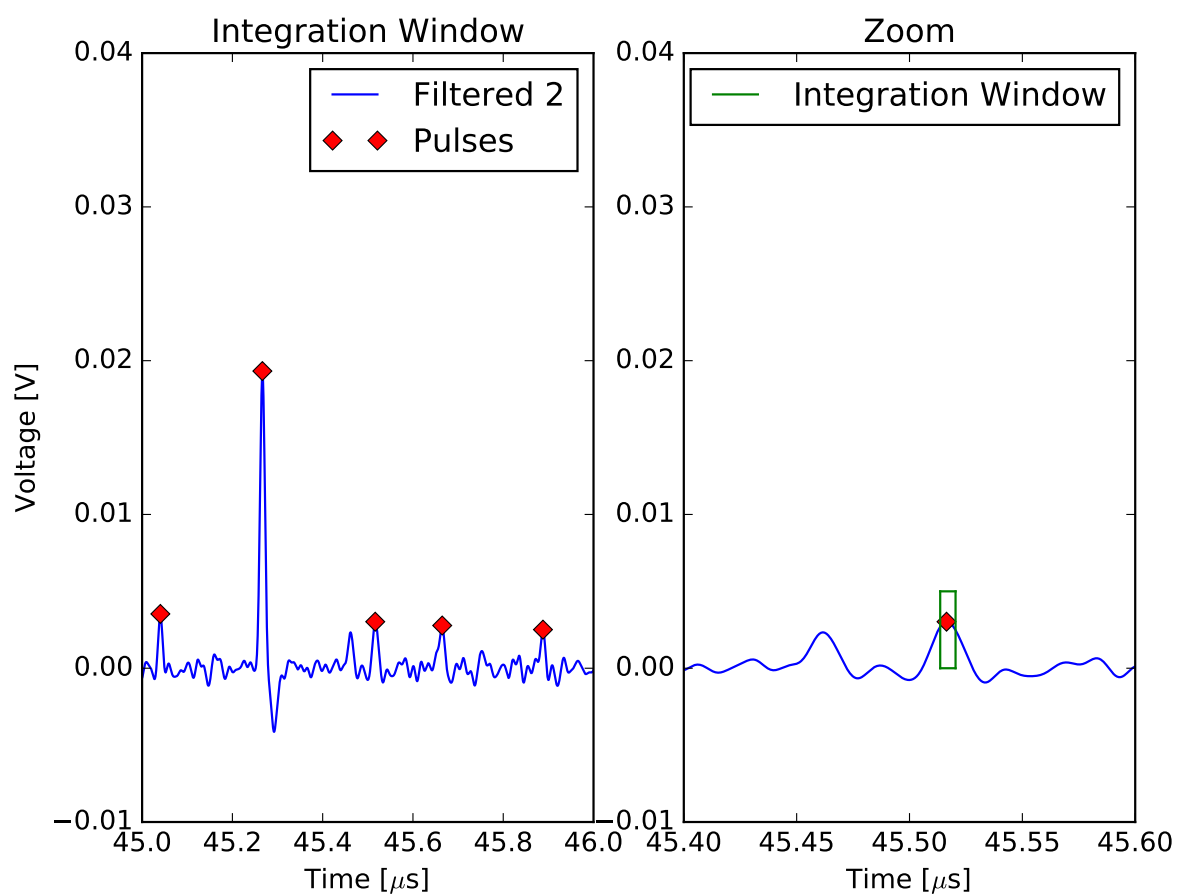


Figure 73: Description

1344 Erklärung zur Master-Thesis

1345 Hiermit versichere ich, die vorliegende Master-Thesis ohne Hilfe Dritter nur mit
1346 den angegebenen Quellen und Hilfsmitteln angefertigt zu haben. Alle Stellen, die
1347 aus Quellen entnommen wurden, sind als solche kenntlich gemacht. Diese Arbeit
1348 hat in gleicher oder ähnlicher Form noch keiner Prüfungsbehörde vorgelegen.

1349 Darmstadt, den April 21, 2017

1350 _____

1351 (B. Gebhardt)